University of California
Santa Barbara

Quantum Dot Lasers Epitaxially Grown on Silicon

A dissertation submitted in partial satisfaction
of the requirements for the degree

Doctor of Philosophy
in
Materials

by

Alan Young Liu

Committee in charge:

Professor John Bowers, Chair
Professor Arthur Gossard
Professor Rod Alferness
Professor Larry Coldren
Professor Chris Palmstrøm

March 2017

The Dissertation of Alan Young Liu is approved.

Professor Arthur Gossard

Professor Rod Alferness

Professor Larry Coldren

Professor Chris Palmstrøm

Professor John Bowers, Committee Chair

December 2016

Quantum Dot Lasers Epitaxially Grown on Silicon

Dedicated to my mother

Acknowledgements

The acknowledgements are my favorite part to read of any thesis, as it gives a glimpse of life outside of research and reveals the intangibles that helped to make the PhD. Despite being typically the shortest part of a dissertation (other than perhaps the abstract), the acknowledgements paints a much more vivid picture of the life of the graduate student. This was actually the first section that I wrote (and probably one that I spent a disproportionate amount of time on), starting in January of 2016 and slowly adding to it over the course of a year. To be honest, I have been thinking about how to craft this section ever since my first year at UCSB, which is a direct reflection of the incredible amount of help that I received from an incredible community of world class researchers, without whom it would be safe to say that the work in this thesis would either not have been possible or not conducted in the same timely manner.

At UCSB, I was extremely fortunate to be placed in a position to succeed right from the start. First and foremost, I was lucky to have not one but two of the greatest advisors ever - John Bowers and Art Gossard. Their professional pedigrees speak for themselves, but what makes them more incredible is the combination of scientific genius along with their unique personalities. They've always been supportive of anything and everything I've done, and essentially gave me the green light to do conduct my research as I saw fit. Never quite pushing (except when reports were due), but always giving me a nudge in the right direction when I needed it. From a research standpoint, it was great to be able to learn from Art's materials knowledge and from John's device expertise. Even more importantly was my exposure to each of their managerial styles that were very different from one another yet had their individual ways of bringing out the best in me.

Professor Gossard is a model citizen to the world. His combination of class, kindness, and positivity creates an uplifting presence. His words of wisdom and questions always

make me think about research in a new way. I also enjoyed our many lunches together where the topic of conversation can range anywhere from movies, the stock market, mountain biking, or stories of the golden days at Bell Labs. One of the enduring memories I have is of a conversation with Professor Gossard towards the end of my first year, during which I was struggling mightily and when the road ahead was not quite clear. He recounted one of his growth campaigns with John English back at Bell Labs, during which they set out to break the world record for mobility in GaAs. The timing was key because I had been floundering about for a while and not really making any progress research-wise. He had told me "when John (English) and I were trying to break world records, we would grow three samples a day, measure them, take the best sample and then grow another three the next day changing something else." After who knows how many days and samples, they blew the previous mobility record out of the water. I think this was a pivotal moment during my Ph.D. that eventually led to my abandoning of the bad habit of trying to cut corners. One year after this conversation after which I had made some progress but was once again stuck, I decided to start over from scratch, throwing everything I had done thus far out the window and embarking upon a furious growth campaign of my own. As will be shown later this thesis, his words have been paying dividends ever since.

Professor Bowers just seems to have a certain knack for winning and success. His competitive spirit and passion for science are contagious, and his management skills are unparalleled. He has constantly challenged me to achieve more and push the limits of what's possible. When I made my first quantum dot lasers on silicon that actually worked reasonably well (following a string of failures), I was more than pleased with myself and ready to write the paper. After reviewing my results he told me that I was close to some world records and that if I can break them then we would get a lot of attention for the work. So I went back to the lab, and emerged a month later with results that did

break the record, which I was ecstatic about. Then he pretty much said "those numbers are great, but can we get more?" So I went back to the lab once again, and emerged two months later with even better results. These results then formed the basis for my proudest paper to date, and I probably would not have gotten them if it weren't for John's urging. This experience ingrained in me the notion that I should always put out my best work. On top of it all he's opened so many doors for me already as a graduate student, I don't quite know where to start. I've also gotten the chance to travel to many different cities and countries for conferences while in his group, each of them a wonderful experience. I would also like to thank him and Ariel for excellent ski lessons. For a brief moment in March 2014 I was not sure whether I'd make it through my entire Ph.D. when he started down a black diamond slope and beckoned me to follow. This was only my second day of skiing and my first off the bunny slopes. Miraculously I somehow survived unscathed. He gave us all a scare when our group administrative assistant emailed us in the summer of 2016 to relay the news that he had fractured a few vertebrae in his neck during a mountain biking trip. However, when I got an email from him an hour later asking me to write a report, I knew that he'd be alright.

I would like to thank Dean Alferness for his constant enthusiastic support of this work. I find it amazing that he even has time to follow our research despite the many duties required of him as the Dean, and have appreciated the fact that he takes some time out to chat whenever we run into each-other despite his busy schedule. One thing that I've really admired about Dean Alferness is his uncanny ability to eloquently articulate the big picture in a few succinct sentences, and there have been a few instances where he was better at explaining the big picture of my research to others than myself! Professor Larry Coldren's excellent Semiconductor Lasers and Photonic Integrated Circuits course (and corresponding textbook) is the source of most of my knowledge on optoelectronics. In addition, I would like to thank him for training many excellent students who were

both materials growers as well as great device scientists, whose dissertations decorate the shelves in the MBE lab and have been an invaluable resource throughout my Ph.D. I will confess that in many ways I've tried to mold myself after his students for their wide "bandwidth" in the sense that many of them grew their own material in either MBE or MOCVD, then fabricated complicated devices out of their material (with many more mask layers than I have), and on top of it all could throw down some solid theory. There have been many nights where I've spent hours on end scouring through their dissertations, and end up thinking to myself "wow...and so far all I've done is __ ." Professor Palmstrom has always been very helpful with his encyclopedic knowledge on a very diverse range of topics. I would also like to thank him for allowing me to crash his group meetings, group BBQs, and group lunches. Being the only grower in the Bowers group for my first few years, it was very helpful for me to have found a supportive group of people in the Palmstrom group whose research was similar to mine from a materials growth standpoint. I've also enjoyed all the great banter and conference travel with them over the years. NAMBE2013 in Banff with Sahil, Bo, and Jason led to many memorable experiences, least of which was running away from moose.

Chong Zhang probably deserves to be co-author on this thesis. He has been like a big brother to me throughout grad school and was always willing to help out no matter how busy his own schedule was. When I first started here I knew nothing about device fabrication and he was the one who made the mask and also came up with the process for our first batch of ridge lasers. Our midnight fab runs for two weeks straight at the beginning of 2013 was where I learned 80% of my processing skills and is what yielded the first working quantum dot lasers on silicon at UCSB. Granted, he also capped off those two weeks by dropping the chip after the final process step and giving me a heart attack. Fortunately we are in the business of making lasers on silicon, and one of the advantages of silicon is its mechanical toughness. I'm grateful for all the dinners and

food he has given me over the years, as well as teaching me some useful Chinese. His workhorse mentality is a constant source of inspiration. HPE Labs is lucky to have him and I have no doubt he will accomplish more great things in the future.

John English...what more can I say about him that hasn't already been said in the acknowledgements section of the 100+ graduates of the UCSB MBE lab's dissertations? This guy not only made the MBE lab work, his presence also made it one of the funnest places to work. JEnglish is truly one of a kind, and it has been an absolute pleasure to have worked in the MBE lab with him. Even though he'll probably deny it to no end if you ask him directly, I'm sure deep down he enjoyed having me around as well, if for no other reason than having someone to heckle at. When John announced his retirement in 2014, I was convinced that I would end up on the 10 year PhD track. I'm glad he decided to stick around part time, and I'm also glad we found a capable replacement in Kurt Olsson. I hope we get a chance to play golf one day.

Hong Lu and Peter Burke taught me the ins and outs of System C, my trusted epi-factory workhorse throughout graduate school. Hong was responsible for most of my MBE training, and I'm so thankful that she had the patience to put up with my (many) initial screw-ups. Her positive presence has been sorely missed these last two years. I also miss Hong's delicious home cooked meals. As I wrote this I thought back to my first few months at UCSB when I was growing late one night and Hong brought me some home-made dumplings. Now I am hungry. My first growth run on silicon was with Peter Burke, and it was a memorable one. Basically everything that went wrong did go wrong that day, and we ended up finally finishing our growth at 5 AM. But I ran into Professor Gossard at 11 PM that night, so even though the sample turned out crappy we may still have gotten some brownie points. I also enjoyed working with the other System C growers past and present: Cheng-Ying Huang, Jeremy Law, Tuan Truong, Justin Norman, and Daehwan Jung. Thanks also to Yan Zheng and Chinhan Lin for teaching me how to grow

and measure broad area lasers back when I didn't know what a laser was, much less how to grow one. The many, many other members of the UCSB MBE lab all helped to make it a wonderful place to work. I hope our semi-annual pinata bashing tradition continues. I will also miss the kareoke sessions with the Oxide 930 crew during growth days.

The entire Bowers group members past and present, I could not have asked for a better group to work with. The members of this group are some of the most talented and motivated people that I know. Starting out as a grower I didn't get to see them much since I was holed up in the MBE lab for most of my first two years, but I'm glad I got to do some more device work later on which allowed us to interface more often. I'm also grateful that they put up with my randomly walking through their office doors when I was not measuring/had no business being in ESB, and just wanted to poke my head in to see what they were up to after getting tired of thinking about some problem. Measurements in FEMTO lab were always fun when there were other photonics people around, mostly because I got to learn about other awesome photonics research. From my early days to picking Daryl and Sudha's brains about what exactly is an optoelectronic oscillator to a perpetual game of 20 questions with Geza on his latest corporate research, I've always enjoyed the company no matter how bad the measurement results. Thanks to Sudha, Daryl, Mike Davenport, and Tin Komljenovic for getting me acquainted with lab and teaching me various different testing techniques and tricks. Thanks to Alex Spott for teaching me about coffee and rock climbing, and being a fantastic travel partner for ISLC. I am looking forward to our 6 year reunion tour when we will co-present 5 year ambient aging study of quantum dot and quantum cascade lasers on silicon. Mike Davenport and Michael Belt gave me an excuse to gossip about photonics at the gym and not actually work out. Thanks to Jon Peters and MJ Kennedy for helping to process my last batch of chips. Jon Peters can always be counted on to understand my obscure Star Wars references. The general photonics crew between the Blumenthal, Coldren, and now

Klamkin groups have also been a blast to work with. In addition to Yan and Chinhan, John Parker, Abi Sivananthan, and Ajit Barve were also particularly helpful to me when I was starting out.

I will miss scrimmaging with the Bowers basketball crew of Daryl, Sudha, Chong, Chao, Tony, Robert, Paolo, Justin, Minh, Lin, Akhilesh, John (for one game), and the other occasional guest appearances. Special thanks to On The Alley for providing discounted fish taco dinners for most of my tuesdays this past year, and the Taco Tuesday crew for always making them enjoyable. The UCSB Photonics Sports Bar provided a welcome distraction from mask and thesis writing.

After starting out alone on this project, I am very excited for Justin Norman, Daehwan Jung, Ludovico Megallini, Brian Cabinian, Jenny Selvidge, Chen Shang, and Yating Wan to join us and work on epitaxial lasers on silicon. It was a pleasure to work with you all and I very much look forward to seeing great results from you guys in the future. Justin Norman deserves special mention because he interned with me in the summer of 2012 and was brave enough to come back for a full PhD (then followed through by sticking around the past few years), I guess I was too easy on him. I'm grateful to have had his help in shouldering many different responsibilities over the years (which only seemed to grow in number).

I am indebted to all of our excellent collaborators who have helped to make this thesis possible in one way or another: Professor Pierre Petroff, Professor Kei May Lau, Professor Larry Lee, Weng Chow, Amy Liu, Bob Herrick, and Professor Osamu Ueda. Whether its providing high quality growth templates, helping with theory and modeling, giving advice on material growth, or assisting with reliability, I consider myself extremely lucky to have had the chance to work with and learn from this extraordinary group of people. I hope we will continue to engage in the future and keep pushing our work forward.

Thanks to all the cleanroom staff for keeping things up and running, fixing all the broken machines and retrieving all the stuck wafers. All the people that worked in the cleanroom made device processing actually fun. Thanks to Mark Cornish and Youli Li for helping with CNSI equipment. I'm also eternally grateful to Ceanna Bowman, Jane Allen, and now Tina Hang for taking care of the paperwork.

I want to acknowledge three people in particular who are not only great friends of mine, but also sources of profound positive influence throughout graduate school: Jason Douglas, David Jorgensen, and Andrew Pebley. Let me begin by stating that all three are models of hyper-efficiency whom I've constantly aspired to. Jason was my first roommate in Santa Barbara. Suffice it to say he has gone above and beyond the call of duty in upholding the high standards expected of a MIT grad in both curricular and (in particular) extracurricular activities in Santa Barbara. I was lucky enough to share an office with David Jorgensen and Andrew Pebley at the beginning of graduate school, both of whom are world class athletes. I'm convinced that David Jorgensen's delicious oatmeal cookies helped to accelerate my recovery from knee surgery in 2013. We also endeavored into the new world of surfing together, and he has hosted many great fondue parties throughout the years. I was lucky to have Andrew Pebley as my roommate throughout most of graduate school as well. His self discipline has inspired me to become more disciplined. I also have him to thank for being my personal trainer through most of 2014 when he would wake me up at 7 AM to go to the gym - a habit that I've since incorporated into my MWF routine.

Much of the groundwork for this thesis was written in a coffee induced haze during early morning "thesis club" writing sessions at Handlebar/Coffee Cat/French Press with Matt Idso and Chelsea Catania. In addition to David's cookies mentioned above, Chelsea's delicious pasta was probably another important factor in helping to expedite my recovery from knee surgery in 2013. She has been a great friend throughout graduate

school, and I'm thankful to have had her support during these past few months when we were both going through thesis writing/defense prep together. Matt Idso is a fantastic adventure partner and an even better friend. We made the irrational decision to jump out of a plane together, which was definitely a highlight of graduate school. Our adventure bucket-list seems to grow at an exponential pace, and I look forward to checking off all the items in the future.

Thanks to my surfing friends through the years who have all provided great company on the waves and/or gave me pointers on surfing. It's definitely going to be rough adjusting to a new life where I can't just grab a board and drive down to the beach at a moment's notice.

Last but certainly not least, I would like to thank my mother for bringing me into this world and for her constant love. This thesis is dedicated to her.

Curriculum Vitæ
Alan Young Liu

Alan Young Liu

Born February 10th, 1990, New York, New York.

Education

2016	Ph.D. in Electronic and Photonic Materials, University of California, Santa Barbara.
2011	B.S. in Physics & Mathematics, Tulane University.
2011	Minor in Business & Engineering Science, Tulane University

Awards and Honors

- Best Student Presentation at the 55th Electronic Materials Conference - 2014
- Best Student Presentation at the 30th North American Molecular Beam Epitaxy Conference - 2013
- NSF Graduate Research Fellowship - 2011
- Tulane University R. C. Read Scholars Award for Outstanding Achievement and Promise for the Future 2011
- Tulane University Physics Department Joseph J. Kyame Outstanding Graduate Award 2011

Publications

1. **A. Y. Liu**, C. Zhang, J. Norman, A. Snyder, D. Lubyshev, J. M. Fastenau, A. W. K. Liu, A. C. Gossard, J. E. Bowers, "High performance continuous wave 1.3 μm quantum dot lasers on silicon." *Applied Physics Letters*, vol. 104, 2014.
2. **A. Y. Liu**, C. Zhang, A. Snyder, D. Lubyshev, J. M. Fastenau, A. W. K. Liu, A. C. Gossard, J. E. Bowers, "MBE growth of p-doped 1.3 m quantum dot lasers on silicon." Journal of Vacuum Science & Technology B, vol. 32, 2014.
3. **A. Y. Liu**, R. W. Herrick. O. Ueda, P. M. Petroff, A. C. Gossard, J. E. Bowers, "Reliability of InAs/GaAs quantum dot lasers epitaxially grown on silicon." IEEE Journal of Selected Topics in Quantum Electronics, vol. 21, 2015.
4. **A. Y. Liu**, S. Srinivasanan, J. Norman, A. C. Gossard, J. E. Bowers, "Quantum dot lasers for silicon photonics [Invited]," Photonics Research, vol. 3, 2015
5. T. Komljenovic, M. Davenport, J. Hulme, **A. Y. Liu**, C. Santis, A. Spott, S. Srinivasan, E. Stanton, C. Zhang, J. E. Bowers, "Heterogeneous Silicon Photonic Integrated Circuits (Invited)," Journal of Lightwave Technology, vol. 34, 2015

6. W. W. Chow, **A. Y. Liu**, A. C. Gossard, J. E. Bowers, "Extraction of inhomogeneous broadening and nonradiative losses in InAs quantum-dot lasers," Applied Physics Letters, vol. 107, 2015
7. Y. Wan, Q. Li, **A. Y. Liu**, A. C. Gossard, J. E. Bowers, E. L. Hu, K. M. Lau, "Optically pumped 1.3 μm room-temperature InAs quantum-dot micro-disk lasers directly grown on (001) silicon," Optics Letters, vol. 41, 2016.
8. Y. Wan, Q. Li, **A. Y. Liu**, W. W. Chow, A. C. Gossard, J. E. Bowers, E. L. Hu, K. M. Lau, "Sub-wavelength InAs quantum-dot micro-disk lasers epitaxially grown on exact Si (001) substrates," Applied Physics Letters, vol. 108, 2016.
9. Y. Wan, Q. Li, **A. Y. Liu**, A. C. Gossard, J. E. Bowers, E. L. Hu, K. M. Lau, "Temperature characteristics of epitaxially grown InAs quantum dot micro-disk lasers on silicon for on-chip light sources," Applied Physics Letters, vol. 109, 2016
10. Q. Li, Y. Wan, **A. Y. Liu**, A. C. Gossard, J. E. Bowers, E. L. Hu, K. M. Lau, "1.3 μm InAs quantum-dot micro-disk lasers on V-groove patterned and unpatterned (001) silicon," Optics Express, vol. 18, 2016.
11. **A. Y. Liu**, J. Peters, X. Huang, D. Jung, J. Norman, M. L. Lee, A. C. Gossard, J. E. Bowers, "Electrically pumped continuous wave 1.3 μm quantum dot lasers epitaxially grown on on-axis silicon, Optics Letters, vol. 42, 2016.
12. **A. Y. Liu**, T. Komljenovic, M. L. Davenport, A. C. Gossard, J. E. Bowers, "Reflection sensitivity of 1.3 μm quantum dot lasers epitaxially grown on silicon," Submitted to Optics Express, 2016.

Conference presentations (as presenter)

1. **A. Y. Liu**, C. Zhang, A. C. Gossard, J. E. Bowers, "Growth of InAs Quantum Dot Laser Structures on Silicon", *IEEE Photonics Conference*, Burlingame, CA, September (2012).
2. **A. Y. Liu**, C. Zhang, A. Snyder, D. Lubyshev, J. M. Fastenau, A. W. K. Liu, A. C. Gossard, J. E. Bowers, "InAs quantum dot ridge lasers on Silicon," *30th North American Molecular Beam Epitaxy conference*, Banff, Canada, October (2013)
3. **A. Y. Liu**, C. Zhang, A. Snyder, D. Lubychev, J. M. Fastenau, A. Liu, A. C. Gossard, J. E. Bowers , "High Performance 1.3 μm InAs Quantum Dot Lasers Epitaxially Grown on Silicon," *Optical Fiber Communication Conference and Exposition (OFC)/National Fiber Optic Engineers Conference*, San Francisco, CA, March 11th, (2014)
4. **A. Y. Liu**, C. Zhang, J. Norman, A. C. Gossard, and J. E. Bowers, "Record lifetimes of GaAs based lasers epitaxially grown on silicon," *Electronic Materials Conference*, Santa Barbara, CA, June 26th , (2014). **(Postdeadline)**
5. **A. Y. Liu**, C. Zhang, A. C. Gossard, J. E. Bowers, "Quantum Dot Lasers on Silicon," *IEEE International Conference on Group IV Photonics (GFP)*, Paris, France, August 27th , (2014) **(Invited)**

6. **A. Y. Liu**, C. Zhang, J. Norman, A. Snyder, D. Lubyshev, J. M. Fastenau, A. W. K. Liu, A. C. Gossard, J. E. Bowers, "Quantum Dot versus Quantum Wells on Silicon," *International Conference on Molecular Beam Epitaxy*, Flagstaff, AZ, September 7th , (2014)
7. **A. Y. Liu**, A. C. Gossard, J. E. Bowers, "Quantum Dot Lasers for Silicon Photonics by Heteroepitaxy," *The 4th International Symposium on Photonics and Electronics Convergence*, Tokyo, Japan, November 19th, (2014) **(Invited)**
8. **A. Y. Liu**, J. Peters, X. Huang, T. Komljenovic, J. Norman, D. Jung, M. Davenport, M. L. Lee, A. C. Gossard, J. E. Bowers, "Electrically pumped continuous wave 1.3 μm quantum dot lasers epitaxially grown on on-axis (001) Si," *International Semiconductor Laser Conference*, Kobe, Japan, September, (2016) **(Postdeadline)**

Conference presentations (as co-author)

1. J. E. Bowers, J. Bovington, **A. Y. Liu**, A. C. Gossard, "A path to 300mm hybrid silicon photonic integrated circuits," *Optical Fiber Communication Conference and Exposition (OFC)/National Fiber Optic Engineers Conference*, San Francisco, CA, March 12th, (2014)
2. J. E. Bowers, E. J. Stanton, M. J. Heck, A. Spott, M. L. Davenport, **A. Y. Liu**, J. T. Bovington, J. R. Meyer, C. L. Canedy, J. Abell, C. D. Merritt, W. W. Bewley, C. S. Kim, and I. Vurgaftman, "Technology for multispectral infrared laser integration on silicon," *IEEE Summer Topicals Meeting*, Montreal, Quebec, Canada, July (2014).
3. W. W. Chow, **A. Y. Liu**, A. C. Gossard, J. E. Bowers, F. Jahnke, "Gain-current relationships in quantum-dot and quantum-well lasers: theory and experiment," *IEEE Photonics Conference*, Reston, Virginia, October, (2015).
4. J. E. Bowers, T. Komljenovic, M. Dvenport, J. Hulme, **A. Y. Liu**, C. T. Santis, A. Spott, S. Srinivasan, E. J. Stanton, C. Zhang, "Recent advances in silicon photonic integrated circuits," *SPIE Photonics West*, San Francisco, CA, February (2016).
5. Y. Wan, Q. Li, **A. Y. Liu**, A. Gossard, J. E. Bowers, E. L. Hu, K. M. Lau, "Room temperature CW 1.3 μm single mode lasing of InAs quantum dot micro-disk lasers grown on (001) Si," *Conference on Lasers and Electro-Optics*, San Francisco, California, June (2016).
6. **A. Y. Liu**, Y. Wan, Q. Li, E. L. Hu, K. M. Lau, A. C. Gossard, J. E. Bowers, "1.3 μm quantum-dot micro-disk lasers directly grown on (001) silicon," *International Conference on Molecular Beam Epitaxy*, Montpellier, France, September, (2016).
7. **A. Y. Liu**, J. Peters, J. Norman, X. Huang, D. Jung, M. L. Lee, A. C. Gossard, J. E. Bowers, "Electrically pumped continuous wave III-V quantum dot lasers epitaxially grown on exact GaP/Si (001)," *International Conference on Molecular Beam Epitaxy*, Montpellier, France, September, (2016). **(Postdeadline)**

8. **A. Y. Liu**, J. Peters, D. Jung, X. Huang, J. Norman, M. L. Lee, A. C. Gossard, J. E. Bowers, "InAs/GaAs quantum dot lasers on exact GaP/Si (001)," *North American Conference on Molecular Beam Epitaxy*, Saratoga Springs, New York, September, (2016). **(Postdeadline)**.
9. D. Jung, **A. Y. Liu**, J. Norman, Y. Wan, K. M. Lau, M. L. Lee, A. C. Gossard, J. E. Bowers, "InAs Quantum Dot Laser Diodes Grown on on-axis Silicon" *The 6th International Symposium on Photonics and Electronics Convergence*, Tokyo, Japan, November, (2016) **(Invited)**

Book Chapters

- Sudharsanan Srinivasan, **Alan Y. Liu**, Di Liang, and John E. Bowers, "Silicon Lasers and Photonic Integrated Circuits, Chapter 15 in Fiber Optic Communication Key Devices (2nd edition)", Springer, 2017 (In Press).

Patents

- **A. Y. Liu**, J. C. Norman, A. C. Gossard, J .E. Bowers, "Epitaxial Laser Integration on Silicon Based Substrates," patent pending, filed 2016.
- **A. Y. Liu**, A. Spott, A. C. Gossard, J .E. Bowers, "Unipolar light emitting devices epitaxially grown on silicon based substrates," patent pending, filed 2016.

Abstract

Quantum Dot Lasers Epitaxially Grown on Silicon

by

Alan Young Liu

This thesis investigates the growth, fabrication, and performance of III-V semiconductor quantum dot lasers epitaxially grown on silicon based substrates as an enabling technology for the realization of low cost, size, weight, and power (cSWaP) photonic integrated circuits. The use of large area, low cost silicon or silicon on insulator (SOI) based substrates as a photonic integration platform is attractive due to existing economies of scale and potential to recycle advanced CMOS fabrication tools already developed for silicon microelectronics. The indirect bandgap of silicon presents a major hurdle towards the complete integration of photonic devices on silicon - in particular a laser. To circumvent inefficient light emission from silicon's indirect bandgap, current methods to fabricate silicon-based lasers typically rely on a separate material for the generation and amplification of light. These methods include integration of III-V materials onto silicon via wafer bonding or direct epitaxial growth, as well as band-gap engineering of group IV elements such as Ge or Ge_xSn_{1-x} grown on silicon for direct gap light emission.

Direct growth of high gain III-V compound semiconductors onto silicon substrates is well suited for high volume applications. Unfortunately, large dislocation densities typically result from the growth process due to fundamental material differences between III-Vs and Si, which is detrimental to both the device efficiency as well as reliability. In this thesis, we demonstrate III-V laser diodes epitaxially grown on silicon with world record performance. Key to our approach is the use of III-V self-assembled quantum dot light emitters in place of traditional quantum wells, offering advantages of reduced

sensitivity to dislocations, reduced sensitivity to reflections/optical feedback, and low values of threshold current (densities). In particular, the reduced sensitivity of quantum dot active regions to dislocations allows us to employ direct epitaxial growth for the integration of III-V quantum dot lasers on silicon substrates with minimal compromise in light emission efficiency.

Contents

List of abbreviations used in this thesis

- ACC: Auto current control (in aging)
- APC: Auto power control (in aging)
- CW: Continuous Wave
- DBR: Distributed Bragg Reflector
- DFB: Distributed feedback
- DWELL: Dots-in-a-well
- ECCI: Electron Channeling Contrast Imaging
- HR: High reflectivity (coatings)
- IV: Current-Voltage
- LI: Light-Current
- LIV: Light-Current-Voltage
- MTTF: Mean time to failure
- PD: Photo-detector
- PIC: Photonic Integrated Circuit
- PL: Photoluminescence
- QD: Quantum Dot
- QW: Quantum well
- RIN: Relative Intensity Noise
- SAG/SAE: Selective-area growth (or epitaxy)
- SEM: Scanning Electron Microscope
- TEM: Transmission Electron Microscope
- VOA: Variable optical attenuator
- XRD: X-Ray Diffraction

Chapter 1

Introduction

1.1 Silicon Photonics

Silicon photonics is an emergent technology that leverages large area, low-cost silicon substrates for the manufacturing of high functionality photonic integrated circuits in a commercial silicon foundry. The development of this technology has historically been driven by the anticipation of low cost optical interconnects to meet ever increasing bandwidth demands (predominantly in datacenters, with applications in metro and computercom as well). There are now emergent applications for silicon photonics in sensing as well, including medical diagnostics, and LIDAR to name a few [1, 2]. Compared to traditional III-V substrates such as GaAs or InP, silicon affords more than an order of magnitude reduction in price per area (see Table 1.1), with high-throughput processing in a silicon foundry presenting additional advantages of cost and yield.

	Si	SOI	GaAs	InP
Substrate cost ($/cm^2)	0.20	1.30	1.65	4.55
Maximum size (mm)	450	450	150	150

Table 1.1: Maximum size and normalized cost of common semiconductor substrates.

1.2 Silicon based lasers

The functionality of a photonic integrated circuit derives from the generation of photons from a light source, manipulation of the light via its phase, amplitude, polarization, or a combination thereof, and detection of the light with a photodetector. Unfortunately. silicon is an indirect bandgap material and inefficient at generating light. To circumvent the inefficient light emission from silicon, current methods to fabricate silicon-based lasers typically utilize gain from a separate material. These methods include integration of III-V lasers onto silicon via wafer bonding or direct epitaxial growth, band engineering of group IV elements such as Ge or Ge_xSn_{1-x} for direct gap light emission, and rare earth doping of silicon/silica based waveguides. An excellent review of silicon based lasers can be found in [3, 4]. Integration of III-V lasers - a proven technology - onto silicon is the most attractive approach from a performance point of view. Most integrated silicon photonics demonstrations to date have used wafer bonded III-V layers which were originally grown on native substrates [5, 6]. Though impressive device results have been demonstrated, use of III-V substrates for the laser growth can be costly and imposes a limit on the maximum bonding size set by the largest available III-V substrate, typically no larger than 150 mm. Direct growth on silicon substrates offer better economies of scale, not limited by the III-V substrate size and cost. These structures may be used as-grown or bonded to patterned silicon-on-insulator wafers for efficient waveguide coupling, making available the full suite of technologies that have been developed on the hybrid silicon platform [6].

Material	Si	GaAs	InP	GaSb	AlSb	GaN
$a_{\|\|}$ (nm)	0.5431	0.56533	0.58688	0.60959	.61355	.3189/.5189
a/a_{si}-1	0	4.09%	8.06%	12.24%	12.97%	16.9% on Si(111)
$\alpha_L(10^{-6}K^{-1})$	2.6	5.7	4.6	7.75	4.22	5.59
α_L/α_L^{Si}-1	0	119%	76.9%	198%	62.3%	115%
E_d (eV)	-	1.25	1.2	1.2	-	2.1
V_d (μm/yr)	-	1∼5	10	15	-	1×10^{-13}

Table 1.2: Basic properties of Si and III-V semiconductors (RT values)[7, 8] $\alpha_{||}$=lattice constant, α_L = linear thermal expansion coefficient, E_d=activation energy for dislocation motion, V_d = dislocation velocity.

1.3 Quantum dot lasers on silicon

Direct growth of high gain III-V laser material onto large area, low cost silicon substrates is well suited for high volume applications. Unfortunately, large dislocation densities result from the growth process due to fundamental material differences between III-V compound semiconductors and silicon - as shown in Table 1.2. For example, GaAs layers grown on silicon typically have greater than $10^8/cm^2$ threading dislocations generated from the 4.09% lattice mismatch, as well as the 119% thermal expansion mismatch (see Table 1.2). Anti-phase domains have historically been an issue due to the polarity mismatch between III-Vs and silicon, but can be largely eliminated with a proper misorientation in the substrate [9]. Despite several decades of research, the threading dislocation problem remains largely unsolved, necessitating the need for thick buffer layers, cyclic annealing, and/or strained superlattices in order to generate adequate device quality layers. Room temperature quantum well lasers have been demonstrated using this approach, however these devices still suffer from high thresholds and/or poor reliability due to remnant threading dislocation densities, dislocation climb, and rough surfaces from the strained heteroepitaxial growth front [10, 11]. These issues are usually compounded when the laser is designed to emit at longer datacom and telecom wavelengths,

Year	I_{th} (mA)/J_{th} (A cm^{-2})	Max lasing temp (^{o}C)	Device size (μm^2)	λ(μm)	Ref.
1999	788/3850 (Pulsed 80 K)	-	800×50	1 (80 K)	[17]
2005-2009	500/900 (Pulsed)	95 (Pulsed)	600× 80 (lowest threshold) 800×8 (highest temperature)	1	[18, 19, 12]
2011	1087.5/725 (Pulsed)	42 (Pulsed)	3000×50	1.3	[20]
2012	45/64.3 (Pulsed) 114/163 (CW)	84 (Pulsed) 30 (CW)	3500×20 (lowest threshold) 3000×20 (highest temperature)	1.26	[21]
2014	150/200 (Pulsed)	111 (Pulsed)	3000×25	1.25	[22]
2014	16/430 (CW)	119 (CW) >130 (Pulsed)	(700-1200)×(4-12)	1.25	[23]
2016	100/62.5 (CW)	75 (CW)	3200×50	1.32	[24]

Table 1.3: Representative summary of In(Ga)As/GaAs self-assembled quantum dot lasers epitaxially grown on silicon

which necessitates the use of higher indium content wells with larger strain (with respect to both silicon and GaAs) that are more easily dislocated. A primary focus of III-V growth on silicon has therefore been to minimize the number of generated dislocations as much as possible. Despite significant reductions in dislocation density to 10^5-10^6 cm^{-2}, dislocation densities near native substrate levels (10^3 cm^{-2}) appear difficult to achieve in planar bulk layers.

Recent reports investigating the use of quantum dot active regions in place of traditional quantum wells to mitigate the negative effect of residual dislocations on laser performance have yielded very promising results [12, 13, 14]. Efficient capture and three-dimensional confinement of injected carriers by the individual dots leads to reduced nonradiative recombination at defects or dislocations [15, 16]. As a result, the effect of dislocations still present in the active layer is greatly diluted by the total number of dots, which are independent of each other. Table 1.3 is a representative sample of various different quantum dot lasers grown on silicon which have been reported over the years. As is evident in the table, there has been rapid progress in this field in recent years.

1.4 Thesis Outline

The outline of this thesis is as follows. We begin with an introduction to semiconductor quantum dots, followed with the method for their growth in Molecular Beam Epitaxy. We will then review the performance of two different kinds of InAs/GaAs quantum dot lasers directly grown on silicon-based substrates as quantified by lasing threshold, output power, and maximum operating temperatures. In the first part, quantum dot lasers grown on intentionally miscut Ge/Si substrates are studied, and a comparison with InGaAs quantum well lasers on similar substrates and with the same device design will be shown. Accelerated aging studies of the aforementioned quantum dot lasers will be presented and compared to previous results of GaAs based quantum well lasers on silicon. In the second part, quantum dot lasers grown on GaP/Si substrates without offcut are studied. Measurements of the relative intensity noise of the aforementioned devices subjected to various levels of optical feedback will be shown, which suggests their potential for stable operation without the need for an optical isolator. Finally, we outline research avenues towards improved performance as well as possible applications that leverage the inherent advantages of this technology.

Chapter 2

Background

This thesis assumes a working knowledge of semiconductor lasers, thus an introduction of which will be omitted. The reader is referred to Professor Larry Coldren's excellent textbook - Semiconductor Lasers and Photonic Integrated Circuits [25], from which I gained most of my semiconductor laser knowledge. The background information presented in this chapter will thus focus on quantum dots and quantum dot lasers specifically. Quantum dot lasers present several advantages over quantum well lasers: 1) lower threshold current (densities); 2) high temperature operation; 3) reduced sensitivity to defects/dislocations which enables us to grow them on silicon as well as make smaller devices without suffering from surface recombination; and 4) reduced reflection sensitivity, which may allow them to operate without an isolator. Items 1-3 will be detailed in the subsequent sections, while the reduced sensitivity of quantum dot lasers to reflections/optical feedback will be introduced in Chapter 6.

2.1 Semiconductor quantum dots

A semiconductor quantum dot is formed when a low bandgap semiconductor material - such as InAs - is surrounded in all three spatial dimensions by a material of higher bandgap - such as GaAs. Assuming the band alignments form a type I straddling alignment [26], electrons and holes in the conduction and valence bands respectively are likely to be "trapped" or spatially confined to the low band-gap region. Electronically, this looks like a three dimensional potential well, and the carriers are forced to exist in a bound state with discrete allowed energies, as opposed to the continuous band of energies associated with typical bulk semiconductors. An upper bound on the confinement energy levels can be described by the energy levels for the infinite potential well [25]:

$$E_{tot} = E_x + E_y + E_z$$

$$E_i^{\infty}(n) = \frac{n_i^2 h^2}{8mL^2}, \qquad E^{\infty}(1) \approx 3.76 \left(\frac{m_0}{m}\right) \left(\frac{100\mathring{A}}{L}\right)^2 meV$$

where L is the confining distance along the dimension of interest, m is the particle (electron or hole) mass, and m_0 is the free electron mass. Thus we see that the emission wavelength of quantum dots can be easily tuned by controlling the dot size and confinement potential/composition profile. Since actual band offsets will always be finite, the actual quantum confinement energies will be slightly lower than the infinite potential well.

InAs/GaAs quantum dots will be the primary focus of this thesis. As will be detailed in the sections below, this quantum dot system is very versatile and allows for the realization of a wide range of wavelengths and morphology. Figure 2.1 compares two samples grown at different growth conditions. One sample was grown at 505°C by depositing 2.2 ML of InAs at 0.06 ML/s and capped with GaAs, while the other was grown at 500°C

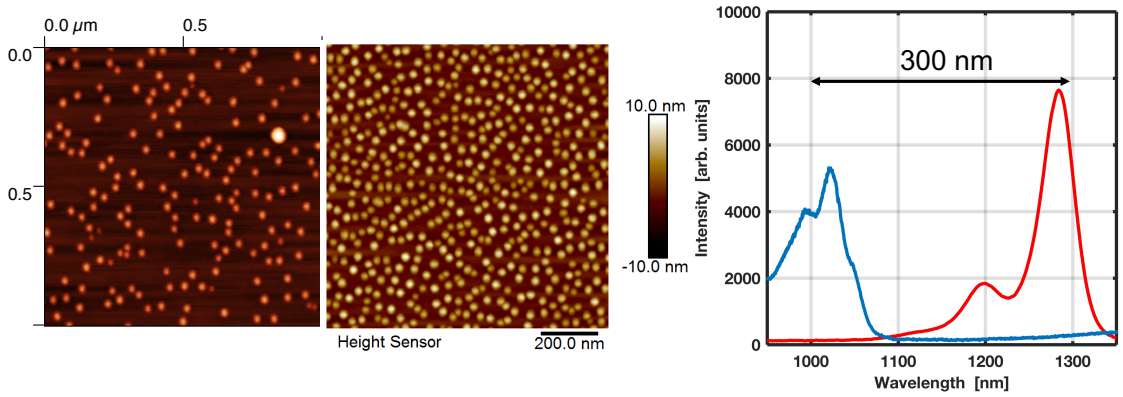

Figure 2.1: Left and center: $1 \times 1 \mu m^2$ AFM scans of InAs/GaAs quantum dots grown at different conditions. The sparse sample was grown at 505°C by depositing 2.2 ML of InAs at 0.06 ML/s and capping with GaAs, while the denser sample was grown at 500°C by depositing 2.75 ML of InAs at 0.11 ML/s and capping with $In_{0.15}Ga_{0.85}As$. The plot on the right compares the photoluminescence spectra of the two samples, with the blue curve corresponding to the sparse sample and the red curve corresponding to the dense sample.

by depositing 2.75 ML of InAs at 0.11 ML/s and capped with $In_{0.15}Ga_{0.85}As$. With these two growth conditions we are able to tune the dot density from 1.7×10^{10} cm^{-2} to 5×10^{10} cm^{-2}, and the peak wavelength from 1000 nm to 1300 nm.

2.2 Quantum dot lasers

Not too long after the quantum well laser was invented, Arakawa and Sakaki proposed the use of three dimensionally confined structures for further improvement in laser performance, giving rise to the field of quantum dot (QD) lasers [27]. Since then, semiconductor quantum dot lasers have gone from a pure thought experiment to widespread commercialization.[27, 28, 29] Semiconductor QD lasers have been the subject of intense interest in recent years due to the promise of being more efficient and stable light emitting devices than current state of the art quantum well (QW) lasers. 1.3 μm InAs/GaAs self-assembled quantum dot lasers are the most well studied semiconductor quantum dot

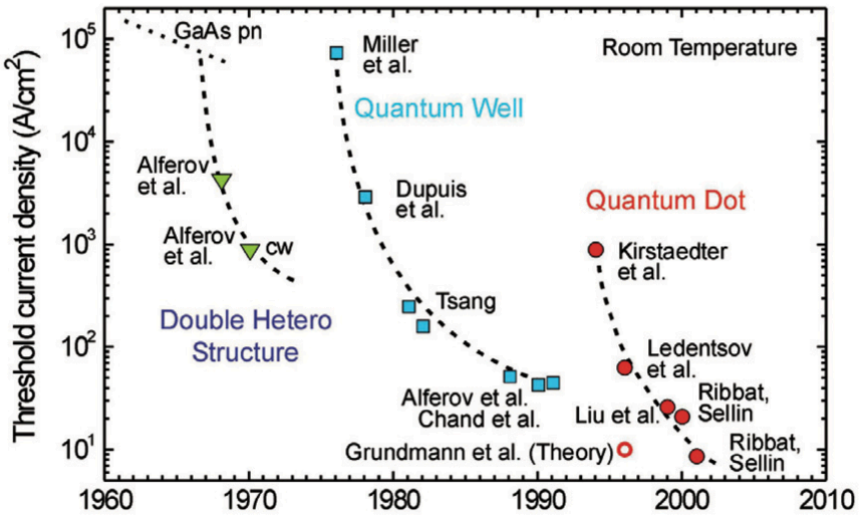

Figure 2.2: Historical trends of threshold current densities (J_{th}) for semiconductor lasers, showing lower ultimate values of J_{th} with each additional degree of confinement. InAs/GaAs quantum dot lasers hold the lowest threshold current density values reported to date among all semiconductor lasers (10 A/cm^2). From [30], © Elsevier Ltd 2011.

system and have demonstrated the lowest threshold current densities (10 A/cm^2, Figure 2.2) and highest lasing temperatures (220° C) of any semiconductor laser [30, 31]. They are thus an attractive light source to meet low power consumption and athermal performance demands for silicon photonics devices.

2.2.1 Reduced threshold and high temperature operation

Self assembled quantum dots (SAQD) are easily grown using Molecular Beam Epitaxy (MBE) or Metal-organic Chemical Vapor Deposition (MOCVD), and the InAs/GaAs QD system has been extensively studied since their discovery. Being essentially a zero-dimensional structure compared to the spatial extent of the carrier wave-functions, the density of states - ρ - of an ensemble of QDs are discrete peaks slightly broadened from the finite size distribution of the dots, meaning a large number of states are available to carriers in a small energy range (see Figure 2.3). This results in higher material gain

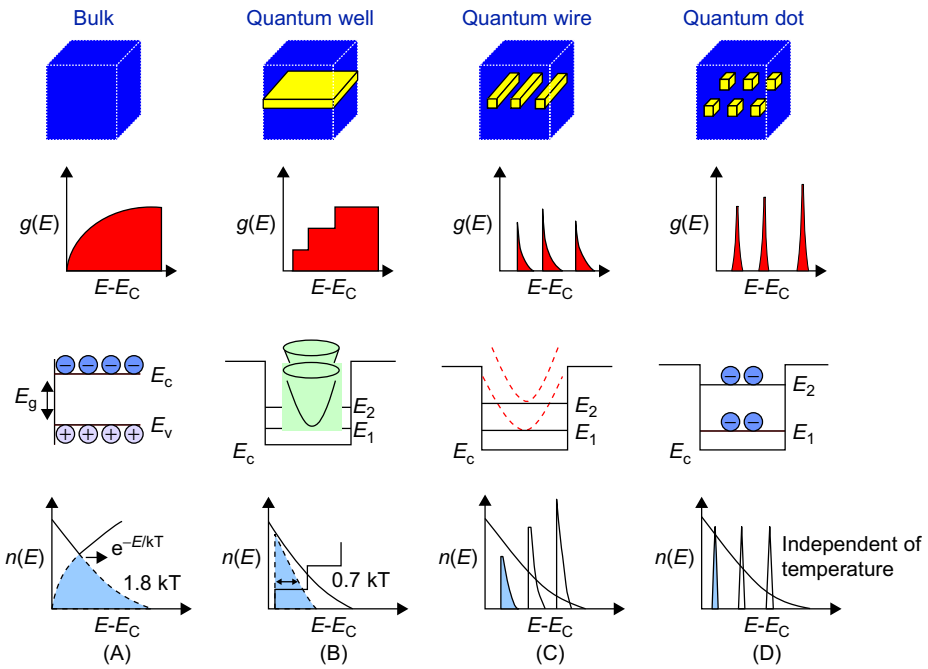

Figure 2.3: Variation in the density of states with degrees of quantum confinement. A perfect quantum dot ensemble has discrete peaks for its density of states. From [32], © IEEE 2011.

($g \propto \rho_r(F_c - F_v)$), a lower threshold carrier density N_{th} (less carriers are required for population inversion), and subsequently low threshold current densities [32]. Furthermore, because of large intersubband separations on the order of 75-85 meV, QD lasers can be made to sustain lasing at high temperatures. With the addition of modulation p-doping they can have essentially a constant threshold current density over a wide range of temperatures [28]. Their emission wavelength can be easily tuned by controlling the dot size and/or composition to tune the quantum confinement energy, allowing emission between 900-1300nm with the InAs/GaAs system as was shown in Figure 2.1. The maximum wavelength is limited by the critical thickness for inelastic strain relaxation from excessive indium content or accumulated strain. Longer wavelengths ($\geq$1.5μm) may be achieved with the InAs/InP system [33].

2.2.2 Reduced sensitivity to dislocations

One key advantage offered by quantum dots that is exploited for this thesis is the fact that quantum dot optoelectronics exhibit decreased sensitivity to dislocations compared to quantum wells [16, 34, 35]. This unique property among semiconductor quantum dots has allowed for the recent achievement of room temperature 1.3 μm lasing on silicon and germanium by direct epitaxial growth [36, 20, 21, 14]. The physical mechanism for this trait is because in a layer of QDs, carriers are confined to the spatial extent of the dots themselves. Thus, defects and dislocations will only affect carriers in the near vicinity of the dislocation and degradation to the device performance is minimized. Conversely in a quantum well, the active region may be rendered useless given the same density of dislocations since carriers in the well are still free to move about within the plane of the well and encounter a defect prior to recombining radiatively. This principle is illustrated in Figure 2.4.

Another way to view this is that the non-radiative capture cross section of a defect depends on the mean diffusion length of the carrier, and related to the non-radiative lifetime as: $\tau_{nonrad} = \frac{4}{\pi^3 \rho_{tdd} D}$, where D is the ambipolar diffusion coefficient, and ρ_{tdd} is the threading dislocation density [37]. To first order, the presence of a high density of dots serves to decrease the mean carrier diffusion length or diffusivity D, thereby increasing the nonradiative lifetime. Figure 2.5 shows the relative variation in internal quantum efficiency ($\eta_{IQE} = \frac{\tau_{nonrad}}{\tau_{nonrad}+\tau_{rad}}$) as a function of dislocation density in GaAs computed using reported ambipolar carrier diffusion coefficients for InGaAs QWs (20 cm^2/s) [38] and QDs (2 cm^2/s) [39]. The radiative lifetime τ_{rad} was assumed to be roughly 3 ns and is roughly the radiative lifetime at a current density of 500 A/cm^2, extracted from a quantum dot gain model based on microscopic theory fitted to experimental data [40]. As can be seen, a decrease in the ambipolar carrier diffusivity has profound impact on

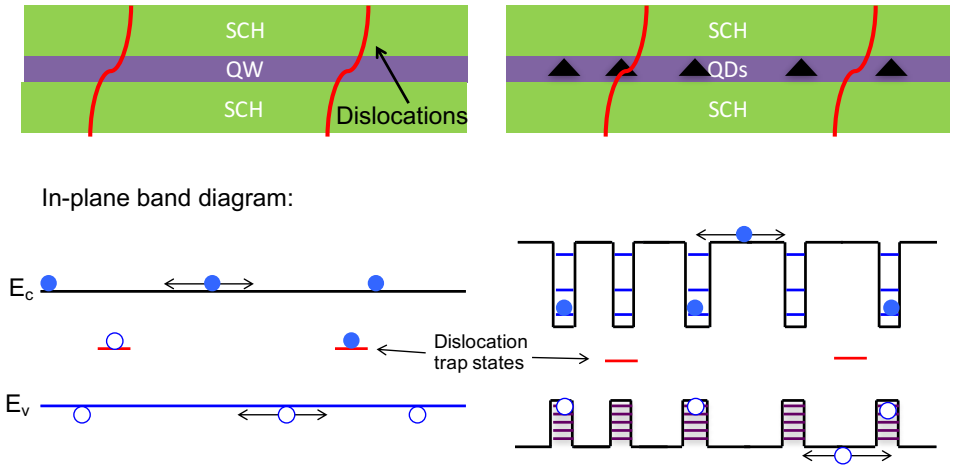

Figure 2.4: The three dimensional confinement potential of quantum dots significantly reduces carrier migration to defect states, unlike the quantum well case where carriers are free to move in the plane of the well.

the device efficiency at relatively high dislocation densities. In essence, as long as the dot density far exceeds the dislocation density, the laser should be able to operate with high efficiency despite high dislocation densities. The same logic is the reason why GaAs quantum dot lasers are also observed to have significantly lower surface recombination velocities compared to GaAs quantum well lasers, as the reduced carriers diffusivity in a quantum dot active region limits the amount of carrier that are able to diffuse to a surface [41].

2.3 Characterization of quantum dots using photoluminescence

Photoluminescence is the main method used to ascertain the optical quality of quantum dot samples grown for this thesis. Using a combination of low and high power photoluminescence we can estimate the relative material gain/threshold current for a given QD sample against a reference sample with known photoluminescence character-

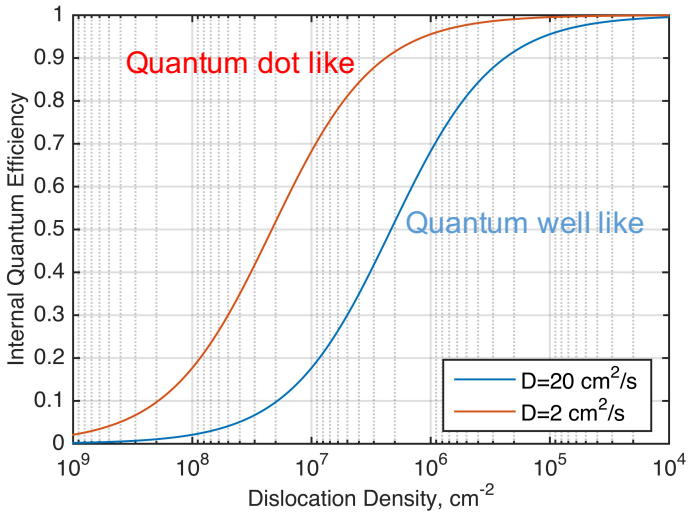

Figure 2.5: relative variation in internal quantum efficiency ($\eta_{IQE} = \frac{\tau_{nonrad}}{\tau_{nonrad}+\tau_{rad}}$) as a function of dislocation density in GaAs computed using reported ambipolar carrier diffusion coefficients for InGaAs QWs (20)[38] and QDs (2 cm^2/s [39]. The radiative lifetime τ_{rad} was assumed to be 3 ns.

istics, and a well characterized laser made with same quantum dot growth conditions. Then by comparing PL characteristics we can infer what the threshold will be like relative to the reference sample without having to process and test devices [42, 43]. The main PL characteristics of interest are peak intensity and full width at half maximum (FWHM) of the ground-state peak, as well as separation and relative intensities between the ground state peak and the various excited states and wetting layer peaks.

Disclaimer: many things can affect the PL intensity. These include but are not limited to sample quality, PL pump laser power, free space attenuation losses of the PL optics, reflections or scatterings from the sample surface, or the phase of the moon. One should always bear this in mind when suspicious looking measurement results arise. Many of these uncertainties can be eliminated by always having a reference PL sample from which the laser characteristics are well known, such that if ever the setup configuration is in doubt it can be re-measured and compared with a prior measurement to see if the setup conditions has drifted to affect the absolute intensity, from which intensity variations due

to relative material quality can be accurately deduced.

For a comprehensive review of the underlying physics see [43]. In brief, recombination processes in a laser (below threshold) is a combination of nonradiative recombination R_{nr} (which may be defect related Shockley-Read-Hall processes proportional to the carrier density $\propto AN$, or Auger which is proportional to the cube of the carrier density $\propto CN^3$), and/or radiative recombination R_{sp}, proportional to the carrier density squared $\propto BN^2$:

$$R_{rec} = R_{nr} + R_{sp} = AN + BN^2 + CN^3 \qquad [25]$$

The total recombination rate should be equal to the carrier generation rate (proportional to pump power):

$$R_{rec} = \frac{P_{in}\eta_{in}}{h\nu} = AN + BN^2 + CN^3$$

where $\eta_{in}P_{in}$ is the input PL laser pump power, and η_{in} is the coupling coefficient that accounts for any attenuation of the pump light on the path to the sample surface as well as any reflection or scattering from the semiconductor-air interface. The detected PL signal intensity (power out from the wafer) can be expressed as:

$$P_{out} = \eta_{out} h\nu R_{sp} = \eta_{out} h\nu BN^2$$

Where η_{out} is the output optic collection efficiency. The uncertainty in the absolute values of η_{in} and η_{out} can be eliminated in the end by making relative comparisons, as alluded to above.

If the material quality is poor and the quantum dot active region is full of defects or dislocations, SRH processes will dominate and:

$$P_{in} = ANh\nu/\eta_{in}, \longrightarrow P_{out} \approx \eta_{out} B(\eta_{in}P_{in}/(Ah\nu))^2, \text{or } P_{out} \propto P_{in}^2$$

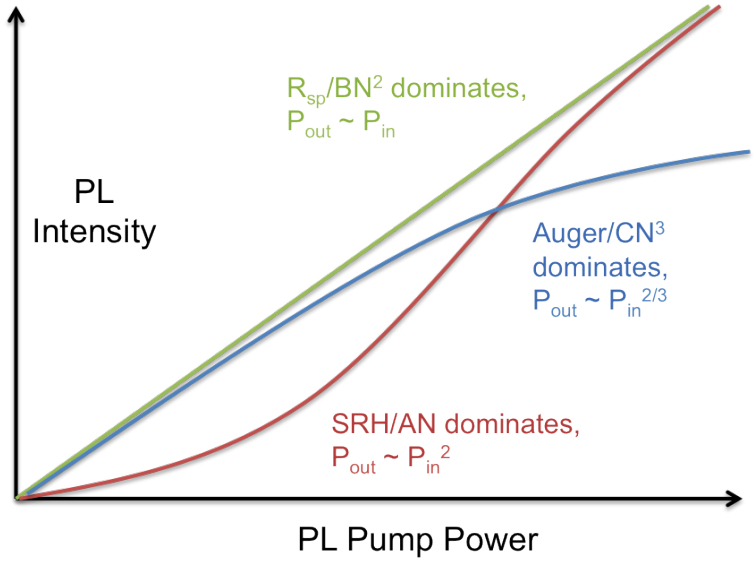

Figure 2.6: PL intensity dependence on pump power for various dominating recombination mechanisms

If the material quality is good, radiative recombination dominates and:

$$P_{in} \propto BN^2, \longrightarrow P_{out} \propto P_{in}$$

If Auger dominates, then:

$$P_{in} \propto CN^3, \longrightarrow P_{out} \propto P_{in}^{2/3}$$

Since we can measure P_{out} (just the intensity of the PL signal) and P_{in} (the PL laser pump power), we can gauge the sample quality by looking at the dependence of the output PL signal with varying PL pump power (see Figure 2.6).

A full sweep of PL intensity versus the input pump power is the most accurate way to observe the described relations above. Because we need to screen through many samples, in this thesis two representative PL measurements for the same sample were taken, one at low PL excitation chosen as the lowest pump power at which an appreciable signal

can be obtained and one at high PL excitation that is close to the saturation power of the pump laser. Typical PL characteristics of 1.3 μm QDs are shown in Figure 2.7. For good laser operation the following characteristics are desirable:

- High ground state (GS) peak intensity at low excitation (indication of low defect density & high radiative efficiency)
- Narrow PL linewidth at low excitation (to minimize QD size distribution and maximize material gain at peak emission wavelength)
- High GS peak intensity at high excitation (indication of high dot density & high maximum modal gain). QWs have a very high density of states in the non-confined dimensions, and as a consequence show no saturation in high pump power PL. 1.3 μm QDs on the other hand, have well defined ground and excited states per dot, and due to their finite density can be easily saturated with a sufficiently high pump power. Because of this, the saturated PL intensity can be correlated with the number density of active QDs, allowing us to quantify the maximum modal gain of the QD layer and compare with other samples through the saturated ground state PL intensity.
- Low wetting layer (WL) intensity at high excitation (indication of efficient carrier capture & strong carrier confinement by the QDs)
- Large separation between the first excited state (ES) and GS peak wavelengths at high excitation. In a similar vein, it is desirable to maximize the separation between the ground state and the WL peak. These metrics are effectively a measure of the depth of the confinement potential. In addition, a low WL peak intensity with respect to the QD peaks at high excitation is desirable because it tells us that more carriers are recombining in the QD than the WL (and/or that the carriers

are well confined to the dots themselves and not escaping out of the QDs). As one may guess these two factors are typically related, and in general the shorter the emission wavelength the brighter the WL peak because of the reduced confinement potential. The major reason for poor thermal stability of the lasing threshold (characterized by the characteristic temperature T_0 in the $I_{th}(T) = I_0 e^{T/T_0}$) in QD lasers is due to carriers escaping out of the QDs into the wetting layer at elevated temperatures, as well as inhomogeneous broadening (i.e. carriers escaping out of a QD that subsequently are captured by a different sized quantum dot which does not contribute to the lasing mode). Thus for good T_0 it is desirable to have the same PL characteristics that indicate good carrier confinement (large WL and GS separation, low WL intensity), and a narrow PL linewidth at low excitation. This is even more important for heteroepitaxial lasers on silicon because good carrier confinement will keep carriers away from dislocations generated from heteroepitaxy and mitigate the increase in threshold. In general adding more indium to the active region increases the QD size, which reduces the quantum confined energy levels with respect to the conduction (and valence) bandedge, and overall increases the confinement potential (band offset between QD and matrix material). As explained above this keeps carriers away from defects in the barrier region outside of the dots, and improves T_0. But excess indium will generate dislocations from the lattice mismatch, decrease the radiative efficiency of the material, and increase threshold. Luckily we can compare these different characteristics in PL to determine the best growth conditions.

At UCSB, the pump laser on our PL setup has a wavelength of 785 nm. This is below the bandgap of GaAs and therefore will be absorbed by not just the quantum dot layers but also the surrounding GaAs matrix. One must therefore consider the carrier

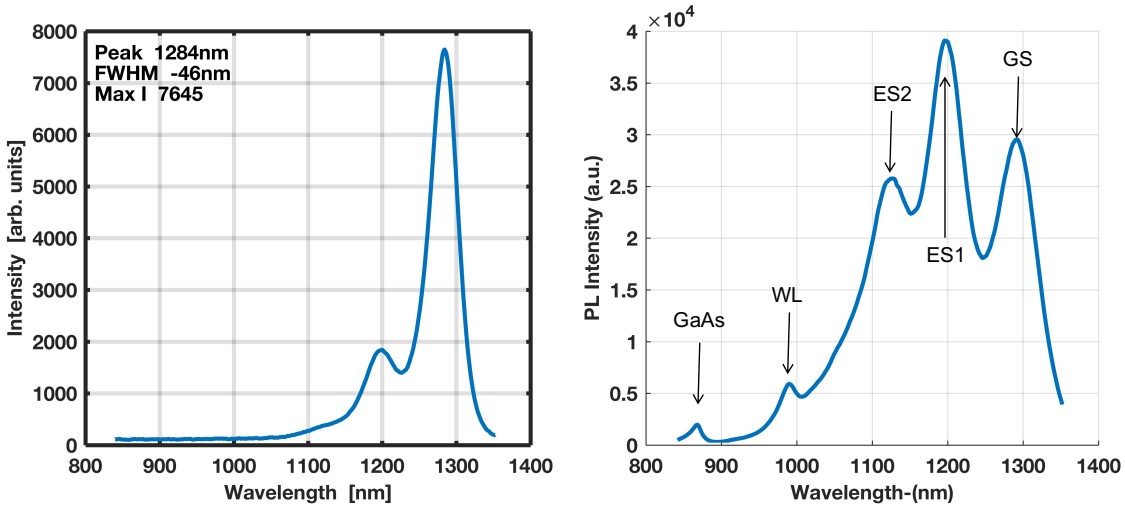

Figure 2.7: Typical PL characteristics of 1.3 μm QDs at low (left) and high (right) PL excitation. Under high excitation, one should be able to resolve the ground state (GS), two excited states (ES), the wetting layer (WL), and the GaAs peak.

transport process when comparing PL intensities. It may be useful to acquire a new pump laser whose wavelength is transparent to GaAs such that it will only be absorbed by the active region. Comparing the relative intensities of two measurements made with these two separate lasers, one that is transparent to the cladding layers and one which is absorbed by the cladding, could then tell us how much of a change in the PL intensity is due to a change in the radiative efficiency of the active region versus carrier transport issues in the cladding or waveguide layers.

2.4 MBE Growth of Quantum Dots

Self assembled InAs quantum dots form via the Stranski-Krastinow (SK) growth mode, which is a strain relaxation driven process. The characteristic of this growth mode is an initial pseudomorphically strained 2D layer growth, followed by the formation of three-dimensional islands with additionally deposited strained layers, illustrated in Figure 2.8. For a very small growth window, the three-dimensional islands are coherent

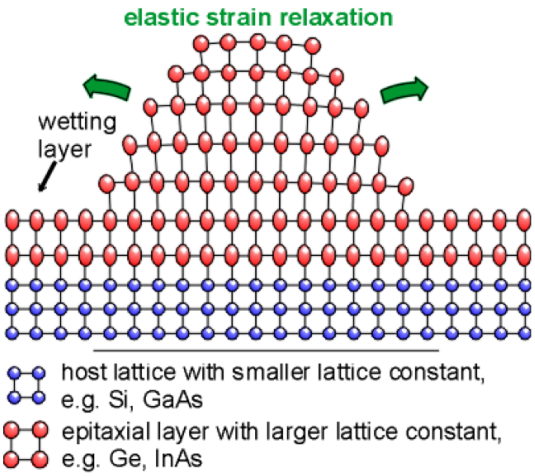

Figure 2.8: An illustration of self assembled quantum dot formed via Stranski-Krastanow (SK) growth. From [44], © 2001 Elsevier Science B.V.

with the surrounding lattice and can be dislocation free. If too much strained material is deposited, then inelastic strain relaxation involving the creation of additional dislocations will occur. The evolution from initial strained 2D layer growth to elastically relaxed 3D growth (coherent formation of QDs), to inelastic strain relaxation (dislocation generation) occurs on the order of just a few monolayers of deposited InAs, as shown in Figure 2.9. Growth of high optical quality quantum dots thus necessitates a very precise control of the deposition thickness and growth conditions.

In MBE growth of self-assembled quantum dots the initial transition from 2D to 3D growth modes characteristic of the SK formation of QDs can be easily monitored with *in situ* Reflection High Energy Electron Diffraction (RHEED), as shown in Figure 2.10. Since the formation of the dots via SK growth marks a change from two dimensional to three dimensional growth, the RHEED pattern will change from a streaky to spotty pattern indicative of the transition. As deposition continues, the RHEED intensity increases indicating a concurrent increase in the density of the QDs as well. The following subsections describe how the desired optical properties of InAs QDs can be achieved by

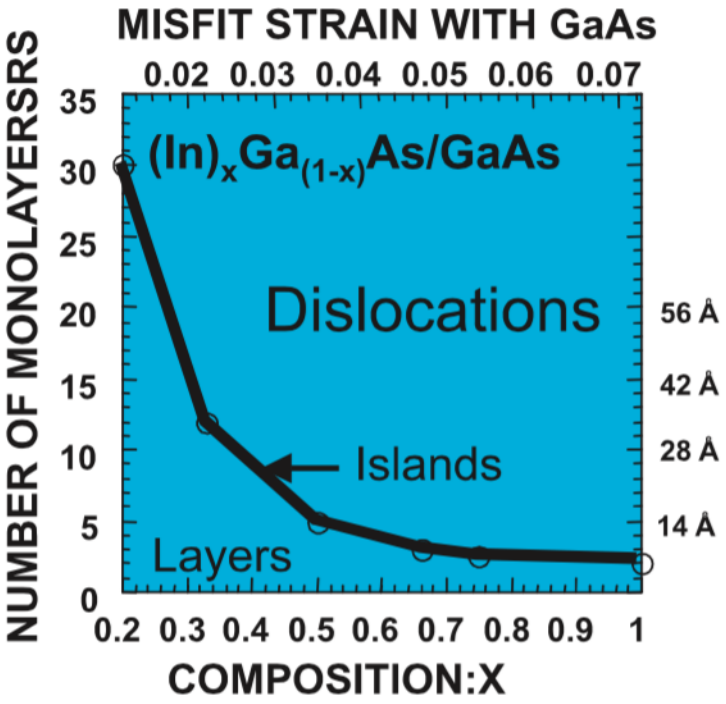

Figure 2.9: A phase diagram of Stranski-Krastanow growth of $In_xGa_{1-x}As$ quantum dots on GaAs. The initial growth is layer by layer, past a certain thickness which is demarked by the solid line three dimensional islands begin to form. However a very small growth window exists for the coherent growth of these islands, and as growth proceeds further with deposition of strained In(Ga)As inelastic strain relaxation via dislocation nucleation will occur. From [45], © Springer-Verlag Berlin Heidelberg 2003.

tuning their growth conditions.

2.4.1 Adatom diffusion length

An important concept for controlling the morphology of SAQDs is recognizing the different growth parameters that affect the mean adatom mobility or diffusion length on the growth front. In general, longer mean diffusion length/increased adatom mobility means bigger and more uniform QDs at the expense of lower QD density, and vice versa. Factors that affect adatom mobility in MBE growth include substrate temperature, growth rate, growth interruptions, V/III flux ratio, and surface roughness.

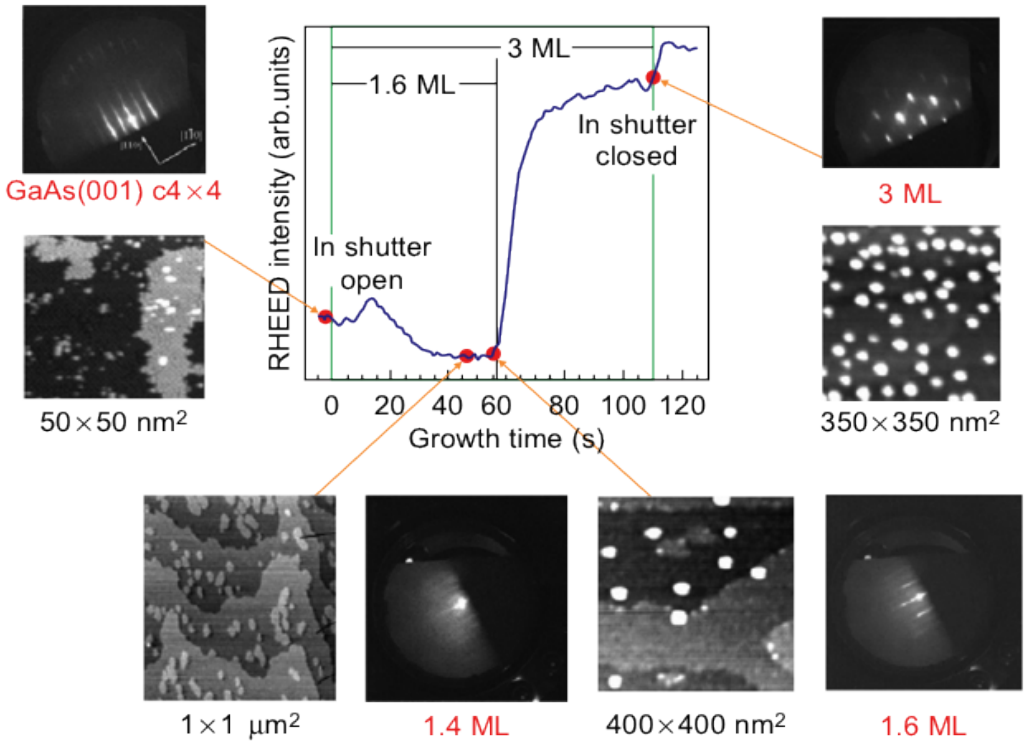

Figure 2.10: RHEED pattern and intensity evolution with increasing InAs deposition thickness during InAs/GaAs quantum dot growth in MBE. From [46], © Elsevier 2011.

2.4.2 Size/wavelength control

For growth on GaAs, self assembled InAs QDs form via SK growth around a nominal InAs deposition thickness of 1.6 MLs. By increasing deposition the average QD size (and emission wavelength) can be continuously increased. Other methods to control the average size of QDs involves changing growth parameters to tune adatom mobility as was alluded to above. At higher temperatures, indium adatoms are more mobile and can therefore traverse large distances to be incorporated into stable nucleation centers resulting in a larger dot size for the same amount of material deposited. Likewise, the effect is similar for slower growth rates (low indium flux) and low arsenic overpressure in MBE, as the mean diffusion length of indium adatoms on the surface increases with de-

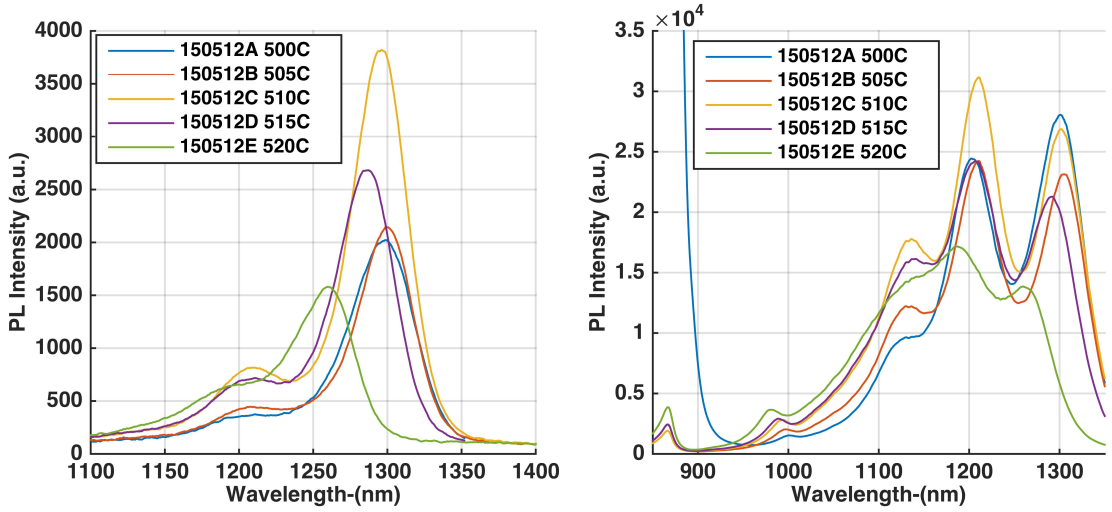

Figure 2.11: Evolution of the optical properties of quantum dots as a function of growth temperature for excitation densities of 1.17 (left) and 59.36 (right) W/cm^2, respectively.

creasing impinging flux due to less collisions with other adatoms or QD nuclei. However, at too high temperatures or too low V/III ratios, indium desorption from the surface becomes significant, leading to a wavelength blueshift due to the decrease in average indium content [47]. These effects are illustrated in Figures 2.11 and 2.12.

2.4.3 Density control

Contrary to adjusting the size of QDs by increasing the mean diffusion length, for a high density of QDs it is desirable to decrease the diffusion length to increase the number nucleation sites. Therefore to increase density one may either decrease the growth temperature, increase the growth rate, or increase the arsenic overpressure. Note that changing these parameters will also change the average size of the dots for the same amount of material deposited as was discussed in the previous section, so one should properly compensate for these effects by increasing or decreasing the total amount of material deposited.

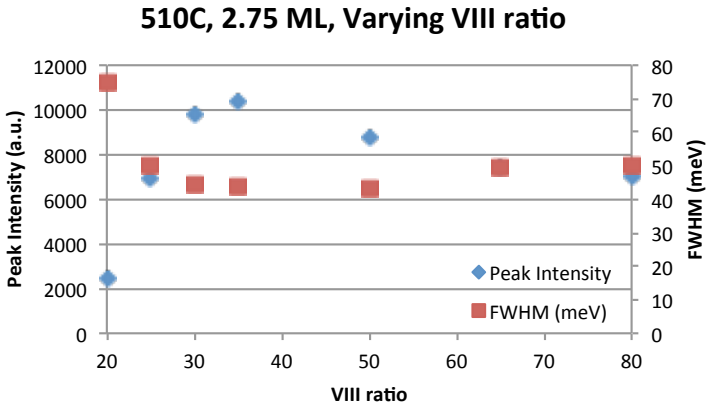

Figure 2.12: The influence of different V/III ratios on the optical properties of InAs/GaAs quantum dots.

One common method to increase the density of QDs on GaAs without changing any of the growth conditions is by depositing a thin (∼2 nm) $In_xGa_{1-x}As$ buffer layer (with x < 20 %). The existing strain field inside the InGaAs buffer causes material from both the InGaAs buffer and the SK wetting layer to be absorbed into the QDs [48]. A similar method for increasing the QD density is the use of antimony (Sb) assisted growth whereby the QD growth surface is irradiated with Sb to form a Sb-terminated surface prior to commencing growth. Upon deposition of InAs on the Sb terminated surface, very high densities of QDs can be obtained. The mechanism for this is not yet clear, although Sb is known to have surfactant like properties and InAs deposited on a Sb terminated surface has been observed to form a high density of one dimensional wires prior to QD formation, which could provide an increased number of QD nucleation sites. [49]

2.4.4 Uniformity /size distribution

Historically, a major perceived negative characteristic of physical QDs is the so called "inhomogeneous broadening" caused by size fluctuations within the ensemble. Unless these size fluctuations were minimal, QDs were predicted to offer no significant advantage

over bulk or QW materials in terms of optical gain [50]. Self-assembled QDs, in particular InAs/GaAs QDs, have now been sufficiently developed in the past two decades such that inhomogeneous broadening can be minimized and photoluminescence linewidths comparable to QWs can be obtained. In other applications, it may even be advantageous to have a large inhomogeneous broadening or a wide gain spectrum, such as broad band light sources.

Size uniformity is generally improved with increasing adatom mobility. If adatoms on the surface have very little time to move around before being incorporated into a QD nuclei, then there will be a large variation in the average size of the QDs due to local fluctuations in adatom mobility, surface energy/chemical potential, etc. If the migration time were increased, then these fluctuations would be averaged out statistically and as a result one will get a fairly uniform ensemble of QDs. Therefore we can expect more uniform dots for low growth rates, low arsenic over-pressures, longer post-growth ripening times, and high temperatures. In the photoluminescence (PL) spectra of an ensemble of QDs, the full width at half maximum (FWHM) of the ground state peak can be used to directly quantify the size fluctuations of the QD ensemble and is inversely proportional to the size uniformity of the dots. For laser devices a small FWHM (high uniformity) is desirable to attain a high gain in the active region. Typically, quantum confinement in the growth direction dominates the total confinement energy, and therefore improving the height uniformity of the dots can lead to significant improvements in the PL FWHM. This is detailed in the following section on the quantum dot capping process.

2.4.5 Capping

The QD capping process is a critical step in the growth of optical quality QDs. The emission wavelength, crystalline quality, and inhomogeneous broadening of the QDs are

all strongly influenced by this step. For InAs/GaAs QDs, the natural capping material would be GaAs. Although this scheme provides strong confinement, the large lattice mismatch between GaAs and InAs generates large strain fields during the capping process and can cause strain driven dissolution of QDs [51], formation of nanovoids [52], and in certain instances dislocations [53]. The emission wavelength of this system is also limited to 1.2 μm.

The aforementioned negative characteristics associated with GaAs capping can be eliminated by using a strain-reducing InGaAs capping layer [51, 53, 52]. Longer emission wavelengths can be obtained by this technique because the InGaAs cap suppresses indium diffusion out of the QDs and reduces the confinement potential. One must carefully control the composition of the InGaAs and avoid growing thick layers of this strained material to avoid the formation of dislocations (see Figure 2.9) [45]. Other capping materials include InAlAs and GaAsSb to extend the emission wavelength beyond 1.3 μm [51]. In general InGaAs is the most commonly used capping material because it produces high optical quality QDs and minimizes the growth complexity.

Improvement of the QD size uniformity in the growth direction and subsequent reduction of the FWHM in PL is also possible through the indium flush method [54]. The premise of this method is to partially cap the quantum dots, then pause the growth. During the growth interruption, the exposed portions of uncapped quantum dots can either desorb from the surface or planarize themselves by diffusing away from the apex of the quantum dots to the side, thus evening out the height of the quantum dots. Since most of the confinement energy is from the Z-confinement (growth) direction, this can result in significant improvements in the PL FWHM. A similar method can be used whereby the dots are capped to cover all but the largest dots which are likely to be incoherent and form dislocations upon fully capping, then raising the growth temperature to intentionally evaporate out the large and incoherent dots before resuming growth [55].

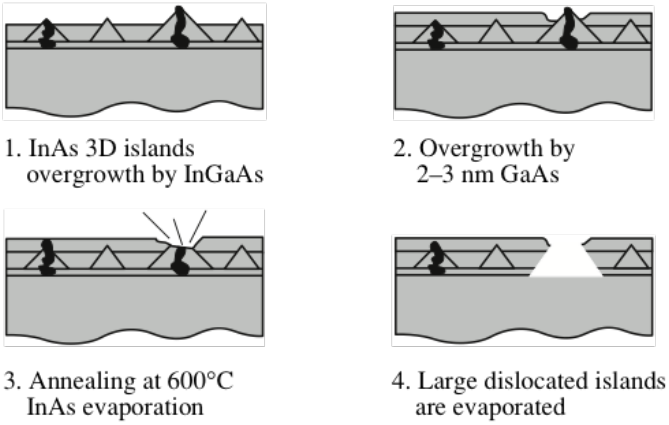

Figure 2.13: A capping process to selectively evaporate out large and dislocated dots. From [55], © 2002 MAIK "Nauka/Interperiodica".

2.5 Relating dot properties to laser performance

The tricky thing with quantum dots is that it is not very straightforward to optimize every desirable characteristic, and almost always there is some sort of trade off for an improvement in a different aspect. For example, shorter wavelength QDs have brighter luminescence compared to longer wavelength QDs because they are smaller so higher densities can be achieved, and they are not as strained as the larger/longer wavelength dots so there are in general less growth related defects. However they generally have poor confinement and T_0. Therefore, the grower/device-designer bear in mind these facts when trying to engineer quantum dots to meet specific performance metrics.

A theoretical model was developed by Weng Chow from Sandia National Labs which can be used to predict how qualitative changes in dot properties will affect the modal gain versus current density in a laser using the dots as the active region [40, 56]. This model makes use of experimental data from this thesis. The experimentally measured spontaneous emission spectra (photoluminescence) as well as modal gain curves (extracted from devices presented in Chapter 3, shown in Figure 3.27) are first compared with microscopic theory to extract values of the inhomogeneous broadening (20 meV)

and non-radiative losses (A=1.2 $\times$ 10^9 s^{-1}, C=10^{-28} cm^{-6} s^{-1}). The material gain in this case was defined for an 8 nm $In_{0.15}Ga_{0.85}As$ quantum well embedding $5 \times 10^{10}/cm^2$ of quantum dots and the associated wetting layer. The material gain is multiplied by the confinement factor Γ to obtain the modal gain Γg, wherein information on the physical properties of the dots (e.g. volume and density) is taken into account through Γ. Holding everything else constant, the dot density, inhomogeneous broadening, and the Shockley-Read-Hall (SRH) recombination rate (A) is then varied and the resulting modal gain curve is computed and compared with the reference experimental data, shown in Figure 2.14. We observe that doubling of the dot density doubles the maximum saturated gain at the expense of increased transparency current density, similar to the effect of increasing the number of quantum wells in a multi-quantum well laser. Decreasing the defect or Shockley-Read-Hall recombination rate decreases the transparency current density while keeping everything else the same. Finally, maintaining the same density and SRH recombination rate but decreasing the inhomogeneous broadening by a factor of two increases the maximum saturated gain by a factor of two without any trade-off in transparency current density.

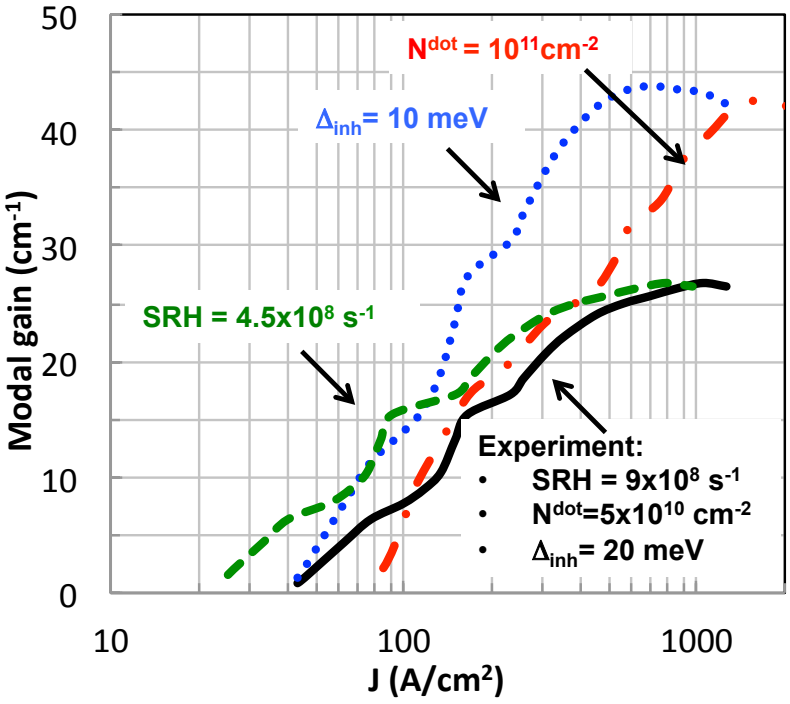

Figure 2.14: Predicted change in the modal gain versus current density J against measured experimental results (black) for: doubling of the dot density (red), halving of the Shockley-Read-Hall recombination rate (green), or halving of the inhomogeneous broadening (blue), with everything else kept the same in each case [40, 56]. Note that the current density plotted here J is the total experimentally applied current density instead of just the amount that reaches the active region ($\eta_i J_{tot}$).

Chapter 3

InAs/GaAs quantum dot lasers on Ge/Si

3.1 First generation devices

3.1.1 Sample growth

Ge-on-Si substrates with a 500 nm Ge buffer grown by chemical vapor deposition (CVD) and an additional 1 μm GaAs buffer grown by MBE were used for the laser growth. The silicon wafer was (100) with a 6° miscut towards [111] to suppress the formation of antiphase domains. The Ge and GaAs layers were deposited by IQE. During the MBE growth process, the thermal treatment of the Ge surface along with the GaAs nucleation conditions were critical to obtain films with mirror-like surfaces and reasonable dislocation densities. The process employed was previously optimized, and includes a thermal anneal to form biatomic step arrays on the Ge surface to promote proper GaAs nucleation [57]. The entire GaAs nucleation and buffer layer was grown as a single-stage process at a constant substrate temperature around 600°C, totaling 1 μm in thickness.

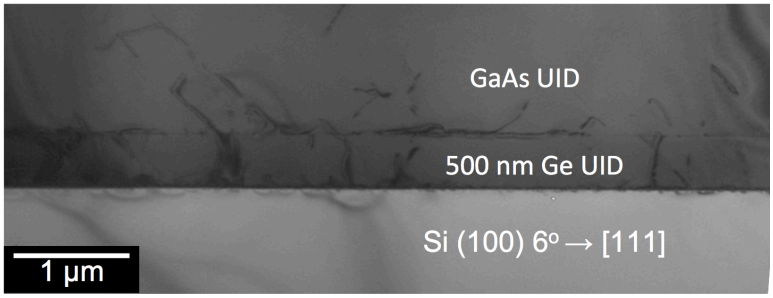

Figure 3.1: Cross sectional transmission electron microscopy (TEM) image of the GaAs buffer grown by molecular beam epitaxy (MBE) on Ge-on-Si substrates.

The sample was then unloaded and diced into smaller pieces to be used as virtual GaAs substrates for the laser growths. The dislocation density in the GaAs layer of the substrate was estimated to be of the order of $\sim 10^8$ cm^{-2} by cross sectional TEM, shown in Figure 3.1. Following a solvent clean and a dilute HF dip, samples were loaded into the MBE machine where they were subsequently cleaned with cracked atomic hydrogen for 30 minutes at a substrate temperature of 420 °C under a hydrogen beam equivalent pressure (BEP) of $3.5\times$ 10^{-6} torr (filament temperature 2200 °C). After the hydrogen cleaning the RHEED was (2x4), corresponding to the GaAs surface reconstruction. A standard in-plane separate confinement heterostructure was then grown (see Figure 3.2.) The active region consisted of 5 layers of InAs quantum dots (∼2.96 ML) embedded in an 8 nm $In_{.15}Ga_{.85}As$ quantum well separated by 37.5 nm GaAs spacer layers, grown at 520°C, and 0.09 ML/s, in punctuated growth mode with a V/III ratio of 35.

3.1.2 Device Fabrication

The as-grown sample was processed into narrow ridge lasers of varying widths ($4-12\mu$ms) and cavity lengths ($800, 1000, \&1200$ μm) using standard lithography, dry & wet etching, and metalization techniques. After dry-etching a mesa to define the ridge waveguide, AuGe/Ni/Au (85/15/500 nm) and Ti/Pt/Au (5/30/1000 nm) were deposited

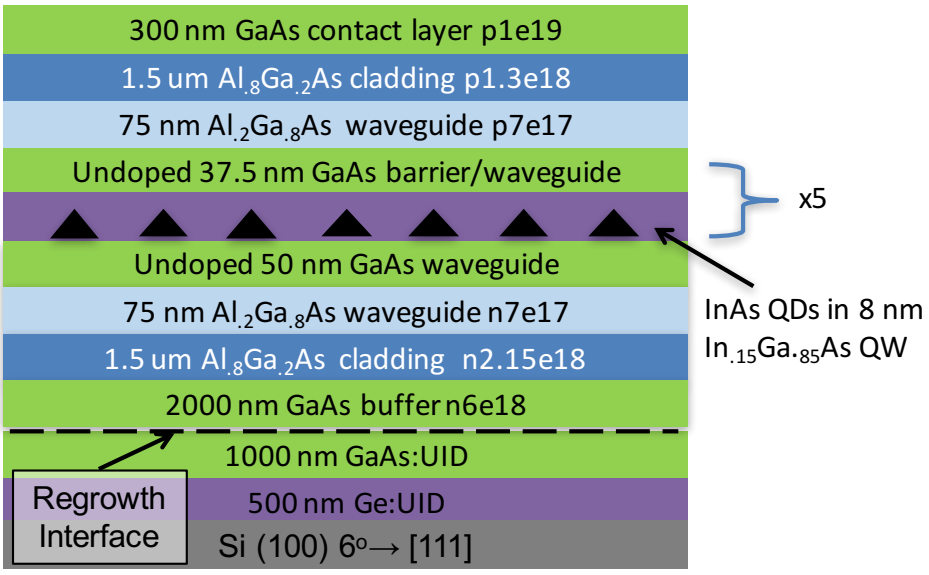

Figure 3.2: Layer structure of the ridge waveguide laser grown on Ge-on-Si substrate.

as the N and P contact metals respectively. The ridge was then passivated with a PECVD SiN_x layer. After etching vias through the passivation dielectric to expose the contact metal, Ti/Au (30/3000 nm) was deposited as the probe metal. The lasers were then diced and the facets polished down to 20 nm RMS roughness.

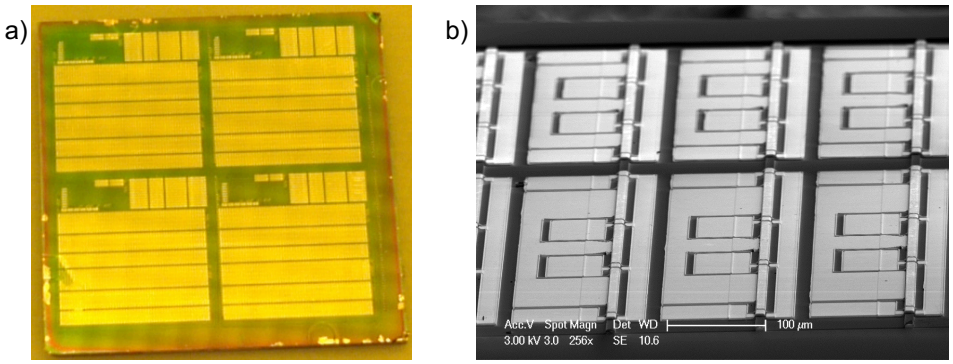

Figure 3.3: a) An optical micrograph of the fabricated chip with four dies. b) A SEM micrograph of two rows of lasers.

3.1.3 Results and discussion

The devices were tested with a broad area InGaAs detector at room temperature under both pulsed (5 μs pulse width, .5% DC) and continuous wave (CW) conditions. Under pulsed operation, the threshold current varied from around 100 to 200 mA for 800 to 1200 μm long devices, respectively. Figure 3.4 shows a comparison of the best laser on GaAs compared with the best laser on silicon. Under CW operation, the threshold current was as low as 160 mA for an 1200 $\times$ 8 μm device with maximum output power around 5 mW (see Figure 3.5). The most promising aspect of the devices was that the threshold current and slope efficiency for the best devices on silicon were comparable to reference devices grown on GaAs and processed together with the ones on silicon (see Figure 3.4). Devices grown on GaAs and silicon both exhibited excited state lasing around 1.15μm compared to the ground state at 1.25μm as was resolved by photoluminescence (samples on silicon had slightly blue-shifted spectra compared to samples on GaAs), suggesting that lasing is from the ground state and that there was significant room for improvement in terms of the optical quality of the active region quantum dots and that even lower thresholds are attainable.

3.2 Second generation devices

The main issues with the first generation devices were: excited state lasing, high thresholds, and poor continuous-wave performance. Several significant changes were made with respect to the design of the first generation devices to improve device performance:

- Digital alloy graded composition layers were added to the interfaces to reduce heterojunction resistance.

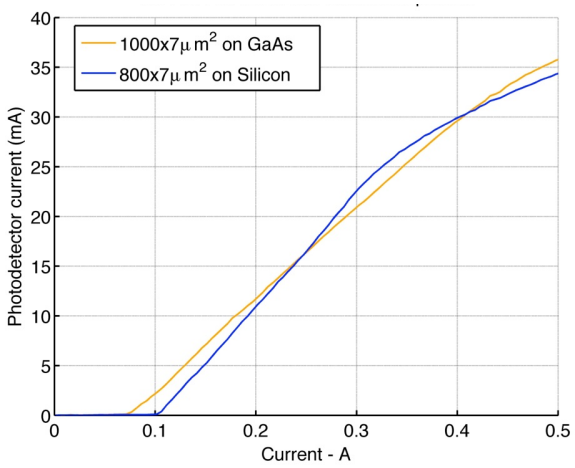

Figure 3.4: Best devices on GaAs and silicon under pulsed measurements at room temperature. Photodetector responsivity is ∼0.9 A/W at the lasing wavelength (the coupling loss from the laser to the photodetector was not properly calibrated for this measurement, thus we refrain from converting to absolute power values).

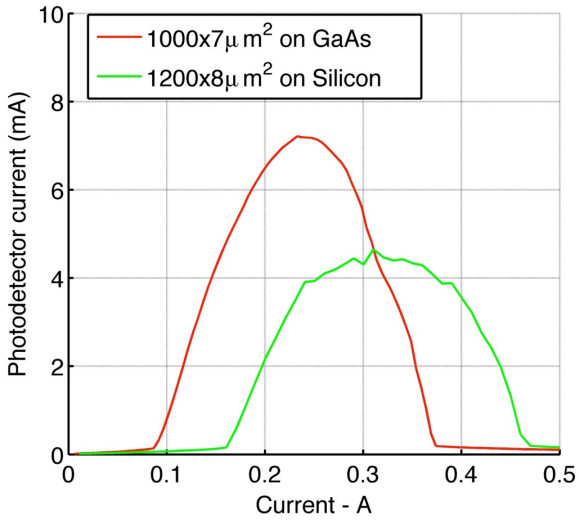

Figure 3.5: Best devices on GaAs and silicon under CW measurements at room temperature. Photodetector responsivity is ∼0.9 A/W at the lasing wavelength (the coupling loss from the laser to the photodetector was not properly calibrated for this measurement, thus we refrain from converting to absolute power values).

- A low loss doping profile was implemented.
- The cladding composition was reduced to 40 percent aluminum from 80 percent, which compromised the confinement factor but was better for doping efficiency and reliability, and therefore continuous wave operation [58].
- The number of active region quantum dot layers was increased from five to seven to increase the maximum modal gain to ensure ground state lasing.

Additionally, the quantum dot growth conditions were completely overhauled and re-optimized, as described below.

3.2.1 Photoluminescence Optimization of the Quantum Dot Active Region

Special photoluminescence structures were grown on semi-insulating GaAs substrates to determine the quantum dot optical quality and for growth optimization. After oxide desorption at 620°C for 5 minutes, the substrate temperature was ramped down to 600°C and a 100 nm GaAs buffer was grown to planarize the surface, followed by a 50 nm digital alloyed $Al_{.4}Ga_{.6}As$ barrier and an additional 50 nm GaAs layer. A dot in a well (DWELL) structure was then grown consisting of InAs quantum dots embedded in 8 nm of $In_{.15}Ga_{.85}As$ [48]. A 50 nm GaAs/50 nm $Al_{.4}Ga_{.6}As$/50 nm GaAs stack completed the growth.

Growth conditions for the InAs quantum dots were optimized as follows: starting from a common set of growth conditions, a set of three or more samples were grown varying only a single growth parameter. Photoluminescence (PL) spectra of each sample was recorded, with care taken to ensure that each sample was measured under identical conditions. An outline for photoluminescence optimization of quantum dots for use in

lasers was given in Chaper 2. At low excitation, defect states are unpopulated and a high GS PL intensity indicates good material quality and high radiative efficiency, while a narrow linewidth is desirable for a uniform dot distribution to maximize gain at the peak emission wavelength. At high excitation, defect states are populated and the GS peak intensity is now directly proportional to the dot density (and the modal gain). A high GS peak intensity along with a low wetting layer intensity are desirable implying high modal gain and efficient carrier capture by the quantum dots. Thus our growth conditions were optimized to give these characteristics, which are beneficial for laser operation (Figure 3.6). Here we define "low excitation" as the minimum pump laser power needed to resolve a clear GS peak, which for our setup corresponds to approximately 1.17 W/cm^2. "High excitation" is taken to be the largest available laser pump power, and is limited to 59.36 W/cm^2 on our setup. The optimum growth conditions from the best sample were then used for the next set of samples while varying a different parameter. This process was repeated for the growth temperature, growth rate, amount of material deposited, V/III ratio, growth interruption time, capping sequence, and post growth annealing time. The optimum growth conditions derived from this process for a high optical quality DWELL structure are: 2.75 ML of continuously deposited InAs at 510°C at a growth rate of 0.11 ML/s, V/III ratio of 35, growth interruption time of 60s after QD formation, and an annealing time of 5 minutes at 600°C after punctuated capping at the QD growth temperature.

A major problem with quantum dot laser growth is potential In-Ga intermixing which occurs during the overgrowth of the upper cladding and contact layers at higher temperatures relative to the quantum dot growth temperatures (i.e. GaAs/AlGaAs is typically grown >580°C while InGaAs is grown around 510°C) [60]. This was found to be an issue for the first generation devices, and historically has impeded the development of high quality long wavelength InAs quantum dot lasers in MOCVD due to the relatively

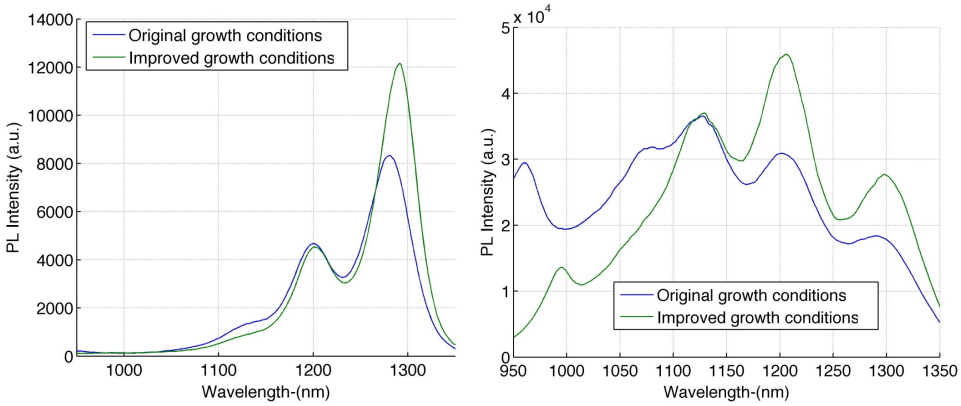

Figure 3.6: Low (1.17 W/cm^2) and high excitation (59.36 W/cm^2) PL spectra of the original and improved growth conditions after optimization (left and right, respectively). The higher ground state peak indicates higher dot density, which translates into higher modal gain for lasers, and the lower ratio of wetting layer to ground state peak intensities indicates a larger fraction of carriers are recombining in quantum dots. From [59], © 2014 AIP Publishing LLC.

hotter growth temperatures needed for efficient precursor pyrolysis [61]. Our improved growth conditions show no significant PL degradation after a 1 hour *in situ* anneal at typical GaAs/AlGaAs growth temperatures of 600°C. On the other hand, quantum dots grown with the original conditions show a 20 nm peak wavelength blueshift and a 6 meV increase in linewidth after annealing, as shown in Figure 3.7. The improvement is hypothesized to arise from the colder growth temperatures and faster growth rates, which suppresses initial In-Ga intermixing during the quantum dot growth and the capping layer growth. The higher dot density in the newly optimized dot samples may also help to suppress In-Ga intermixing, if we consider that the intermixing occurs to relieve local strain (and therefore a higher density of dots will result in lower reduction of local strain from intermixing). The punctuated capping process may also play a role by allowing excess indium on the growth surface to reincorporate into smaller quantum dots or be "flushed" from the surface, [54] reducing alloy intermixing upon overgrowth with GaAs at hotter temperatures.

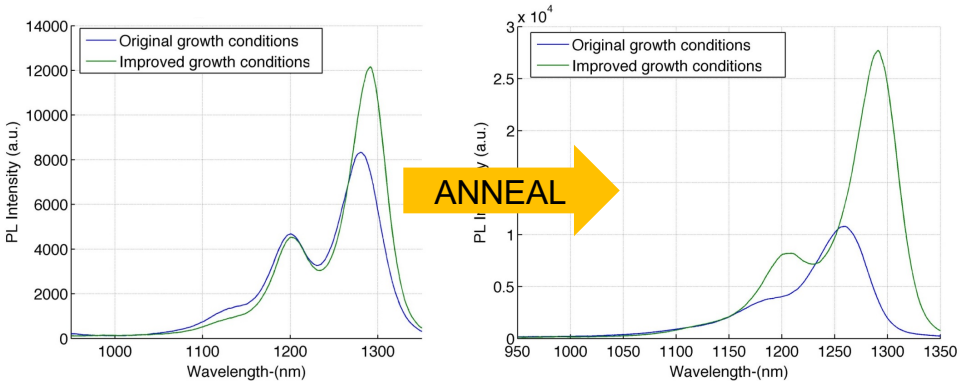

Figure 3.7: Low excitation PL spectra of 5 layer quantum dot samples grown with the original and improved conditions before (left) and after (right) a 50 minute *in situ* anneal at 600°C. While a 20 nm blueshift accompanied by a 6 meV PL broadening was observed for the original conditions used in the first generation devices, the improved growth conditions show negligble broadening and wavelength shift.

3.2.2 Second generation laser growth

The new quantum dot growth conditions were used for the growth of new lasers on Ge/Si with the additional design changes mentioned above. The substrates were degreased with a solvent clean followed by a 30s dip in dilute (10%) HF prior to loading into a Varian Gen II MBE machine. After a dehydration bake at 200 °C in the load lock, the substrate was transferred into the MBE prep chamber where the surface was cleaned with a (Veeco) atomic hydrogen source for 45 minutes at a substrate heater temperature of 420 °C and a hydrogen beam equivalent pressure of $\sim 3.5 \times 10^{-6}$ torr to remove residual carbon or oxygen impurities prior to commencing growth. Two GaAs/$Al_xGa_{1-x}As$ graded index separate confinement heterostructure (GRINSCH) lasers were grown on such substrates. InAs quantum dots embedded in an 8 nm $In_{0.15}Ga_{0.85}As$ quantum well and separated by 37.5 nm GaAs barriers were grown as the active region. In one laser, the GaAs barriers separating the quantum dots was modulation p-doped using beryllium, otherwise the two structures are nominally the same, as shown in Figure 3.8. A separate photoluminescence structure similar to the ones used for optimizing growth conditions

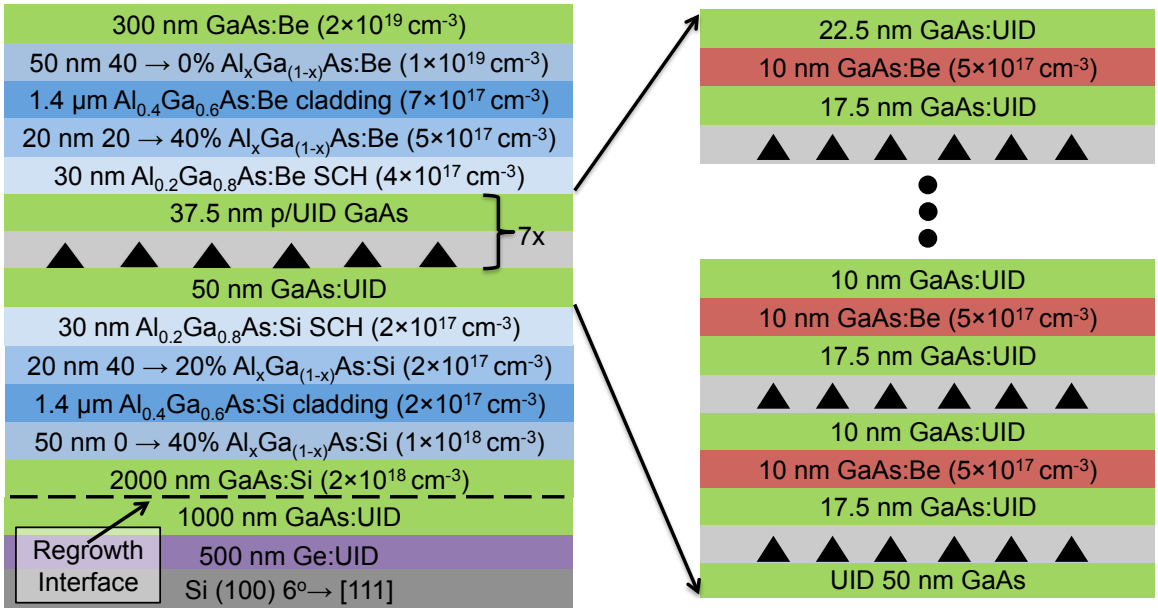

Figure 3.8: Complete layer structure for the GRINSCH quantum dot laser with a modulation p-doped active region. From [59], © 2014 AIP Publishing LLC.

was grown with the optimal conditions on an identical silicon substrate to compare with quantum dots on GaAs.

The same mask and fabrication process was used to fabricate ridge waveguide lasers out of the new material. AuGe/Ni/Au and Ti/Pt/Au were used as the N and P contacts, respectively. Plasma enhanced chemical vapor deposition (PECVD) SiO_2 was used as an electrical isolation layer, and vias were opened to the contacts prior to deposition of Ti/Au probe metal. The lasers were then diced into varying cavity lengths and the facets were formed by polishing. A subset of devices were coated with 95% high reflection (HR) coating on the rear facet, while another subset of these devices were coated with 20-25 nm of silicon nitride on both facets before applying HR coating to the rear facet. The difference in facet reflectivity due to the nitride layer is determined to be less than 4% from simulation and measurements on calibration samples, thus yield data for the two sets are presented together. The labels 'HR/SiN' and 'HR/Polish' will be used to differentiate nitrided and non-nitrided devices, respectively. Likewise, the labels 'undoped' and 'p-

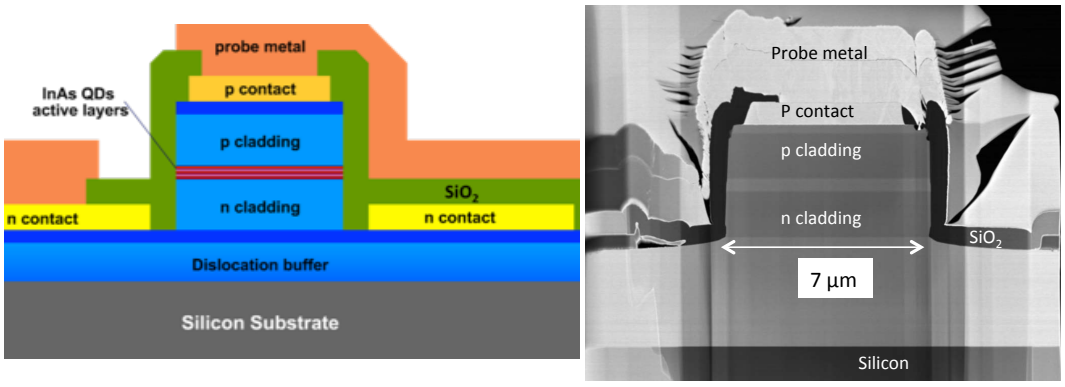

Figure 3.9: Left: A cross-sectional schematic of the ridge waveguide laser devices. Right: A cross-sectional slice created via focused-ion-beam milling as viewed in SEM.

doped' will be used to distinguish between devices with intrinsic or modulation p-doped active regions, respectively. Laser bars were probed on a copper heat sink and thermal paste was applied to the substrate side to ensure temperature uniformity. A device schematic along with a corresponding cross-sectional view is shown in Figure 3.9.

3.2.3 Results and Discussion

Morphological and optical properties of quantum dots grown with the optimized conditions are compared by photoluminescence and atomic force microscopy (AFM) scans (Figure 3.10 and Figure 3.11). Compared to growth on native GaAs substrates, the room temperature peak PL intensity of the QDs on Si shows a slight degradation in intensity to $\sim 80\%$ with an approximate 25 nm blueshift in the peak wavelength. The PL characteristics between the two are otherwise qualitatively similar. A similar blueshift has been seen in other InAs quantum dots grown on silicon, possibly due to residual compressive stress between GaAs and silicon [62, 13]. The quantum dots grown on silicon are similar in morphology to those grown on GaAs. Although the quantum dots on GaAs seem to be slightly denser compared to those grown on silicon ($\sim 5 \times 10^{10}/\text{cm}^{-2}$ on GaAs versus $\sim 4 \times 10^{10}/\text{cm}^{-2}$ on silicon), it is unclear to what extent this is due to

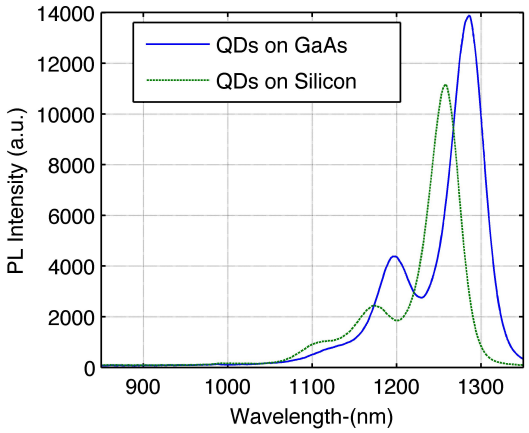

Figure 3.10: Low excitation PL spectra of InAs QDs grown with the optimized conditions on GaAs (solid blue) and silicon (dashed green).

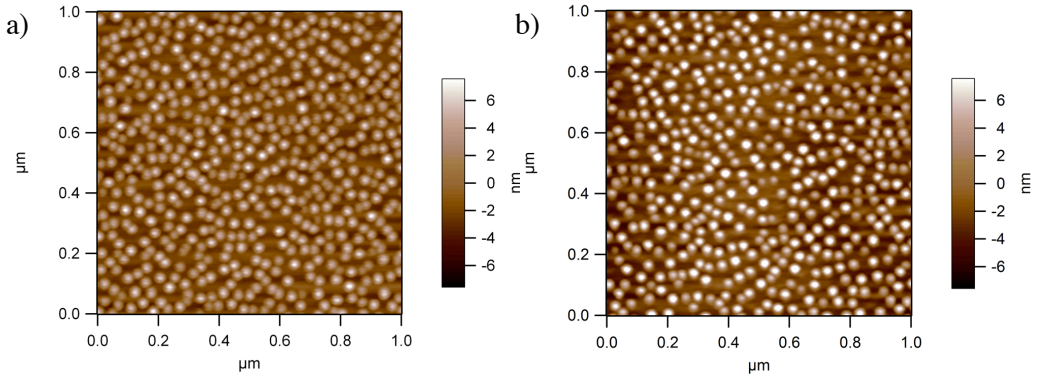

Figure 3.11: 1×1 μm^2 AFM scans of the optimized InAs quantum dots grown on GaAs (left) and silicon (right).

unintentional run-to-run variations in growth conditions, or the effect of residual stress on the quantum dot formation kinetics. A more systematic study will be needed to resolve these effects in order to make a fair comparison between the two cases.

Uncoated devices

Ridge waveguide lasers fabricated from the as grown material exhibit repeatable continuous wave (CW) performance higher than previous quantum dot lasers grown on silicon. Figure 3.12 shows the light output-versus-current (LI) curve of a 1155×5 μm^2

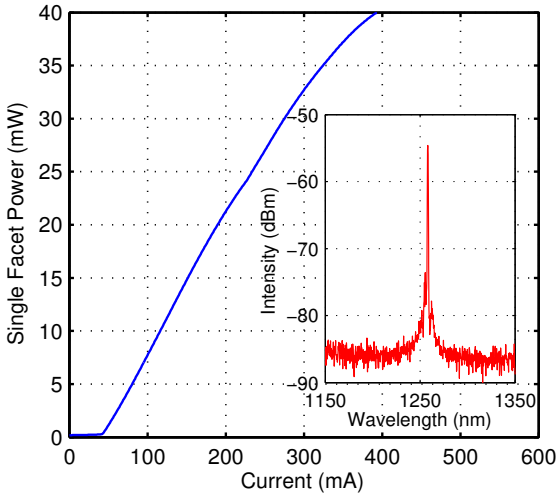

Figure 3.12: (Color online) Continuous wave light output versus current (LI) at 20°C for a p-doped 1155×5 μm^2 laser with polished facets. (Inset: Room-temperature continuous wave lasing spectra of a p-doped laser at 1.2×I_{th}. A clear lasing peak is observed around 1258 nm.) From [59], © 2014 AIP Publishing LLC.

p-doped device with a CW threshold of 42 mA and more than 40 mW of output power from a single facet. Figure 3.13 shows CW LI curves taken at different temperatures for an identically sized p-doped device on a different part of the die, with a similar LI curve at room temperature as the one in Figure 3.12. Modulation p-doping of the active region has been used to significantly enhance the T_0 of InAs quantum dot lasers grown on native GaAs substrates,[63] and we achieve the same effect for InAs quantm dot lasers grown on silicon. T_0 of 75K between 20-60°C and 52K between 60-120°C are calculated from pulsed measurements to eliminate self heating effects. These values are higher than typical values of T_0 for 1.3 μm quantum dot lasers with intrinsic active regions, which are around 30 to 60 K [36]. Ground state lasing for these devices occurs around 1258 nm at room temperature (inset of Figure 3.12). The maximum CW lasing temperature for the device shown in Figure 3.13 is 95°C.

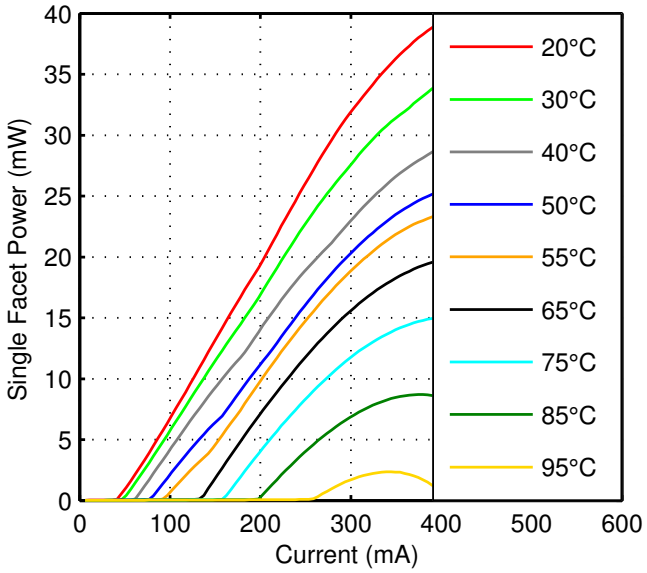

Figure 3.13: (Color online) Continuous wave light output versus temperature for a 1155×5 μm^2 p-doped laser. T_0 is 75K between 20-60°C and 52K between 60-120°C. From [59], © 2014 AIP Publishing LLC.

HR Coated Devices

Continuous wave (CW) thresholds as low as 16 mA and output powers exceeding 50 mW are simultaneously achieved for a 937×4 μm^2 HR/Polish device with an intrinsic active region measured at 20°C, shown in Figure 3.14. Emission spectra as a function of injection current is shown in Figure 3.15 for the same device, displaying clear lasing peaks around 1250 nm which coincide with the ground state photoluminescence peak (Figure 3.10). This device has a maximum CW lasing temperature of 110°C (Figure 3.16). Pulsed light-current (LI) curves were used to calculate T_0 to eliminate self heating effects, yielding a value of 43 K from 20-110°C. Previous work on 1.3 μm InAs quantum dot lasers with intrinsic active regions grown on Ge and Ge-on-Si substrates showed similar values of T_0 as reported here with CW lasing up to 60°C and 30°C, respectively.[36, 21] Figure 3.17 shows the light-current-voltage (LIV) plot for an undoped 1130×10 μm^2 HR/SiN laser with up to 176 mW of output power in CW operation, the highest reported for telecom

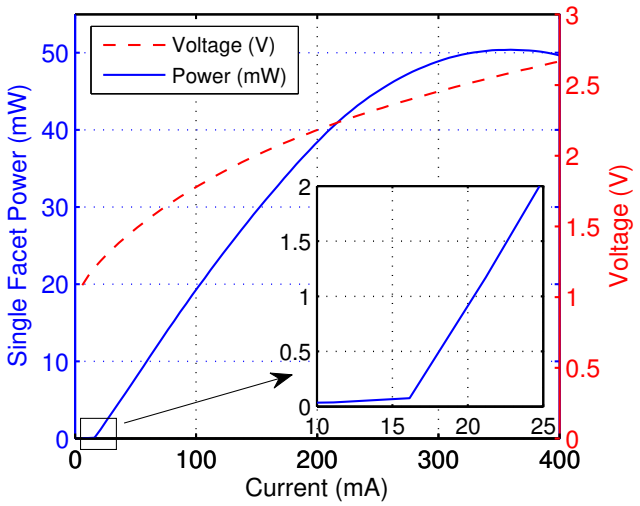

Figure 3.14: LIV plot of an undoped 937×4 μm^2 HR/Polish laser. Inset: threshold kink at 16 mA. From [14], © 2014 AIP Publishing LLC.

lasers on silicon. The maximum single side wall plug efficiency for this device is 18% at 150 mA with a corresponding differential efficiency of ∼37%.

Similar device characteristics are obtained for the same nominal laser structure grown on a separate wafer but with modulation p-doped active regions. For example, a p-doped 1155 × 4 μm^2 HR/Polish device has a 21 mA threshold with nearly 54 mW of output power at 20°C. Figure 3.18 shows LI curves at different temperatures for a p-doped 993×5 μm^2 HR/SiN device. T_0 for this device as estimated from pulsed measurements is 143K from 20-40°C and 41K from 40-120°C. Examination of the lasing spectra as a function of current and temperature indicates that the second kink in the LI curve at 70°C is due to the onset of dual state lasing with the excited state, commonly reported for InAs quantum dot lasers where gain and carriers are not fully clamped at threshold. As the temperature is increased, the ground state power is reduced until ground state lasing is quenched around 100°C in pulsed operation and 80°C in CW operation. For the device shown in Figure 3.18, CW lasing continues in the excited state up to 119°C, while lasing continued in pulsed operation until testing was stopped at 130°C. This is

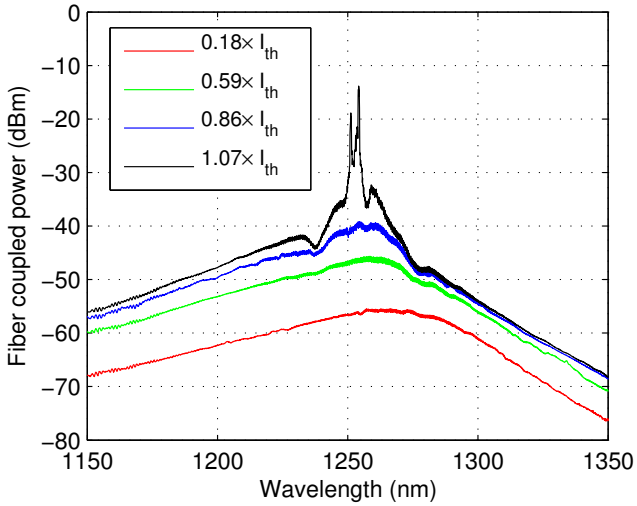

Figure 3.15: Room temperature continuous wave emission spectra of the device in Figure 3.14 at different injection currents. From [14], © 2014 AIP Publishing LLC.

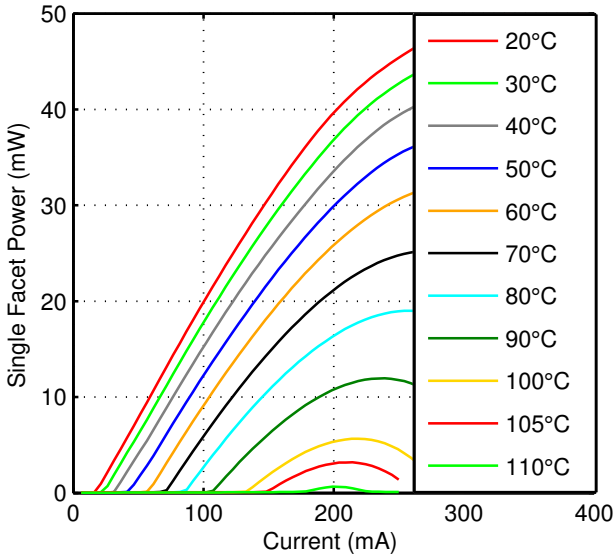

Figure 3.16: CW LI curves at various stage temperatures for the device in Figure 3.14 showing lasing up to 110°C. From [14], © 2014 AIP Publishing LLC.

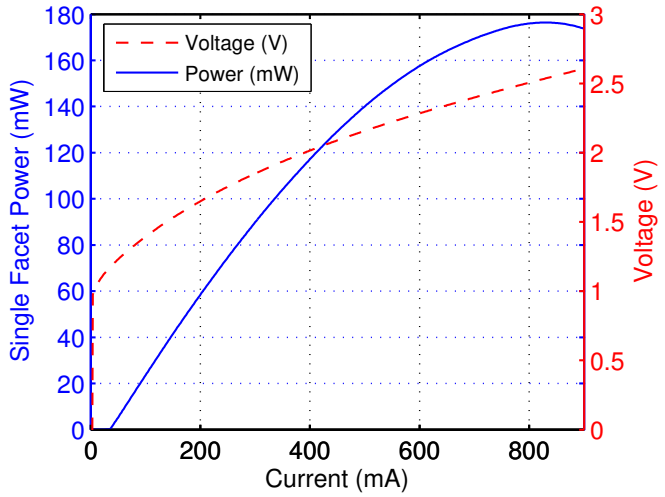

Figure 3.17: LIV plot of an undoped 1130×10 μm^2 HR/SiN laser. Threshold is 38 mA with 176 mW of output power at 20°C. From [14], © 2014 AIP Publishing LLC.

the highest CW lasing temperature for lasers on silicon, exceeding the previous record of 105°C reported for a 1.3 μm AlGaInAs quantum well hybrid silicon laser[64].

Threshold versus temperature is plotted for several p-doped devices with 4-5 μm ridge widths and various cavity lengths in Figure 3.19 and compared with the undoped device in Figure 3.14. The data range is restricted to 20-70°C where ground state lasing is dominant and the beneficial effects of p-doping are most pronounced. Near room temperature (20-40°C) T_0 is usually in the range of 100-200K for p-doped devices, generally increasing with cavity length (lower mirror loss). Similar T_0 values and high temperature pulsed lasing over 100°C were reported for p-doped InAs quantum dot lasers grown on native substrates and wafer-bonded to silicon, although no CW characteristics were reported [65]. The change in lasing wavelength versus stage temperature in pulsed operation for a p-doped HR/SiN laser is shown in Figure 3.20, with an approximate change of 0.4 nm/K from 20 to 100°C, until a switch to excited state lasing at 110°C.

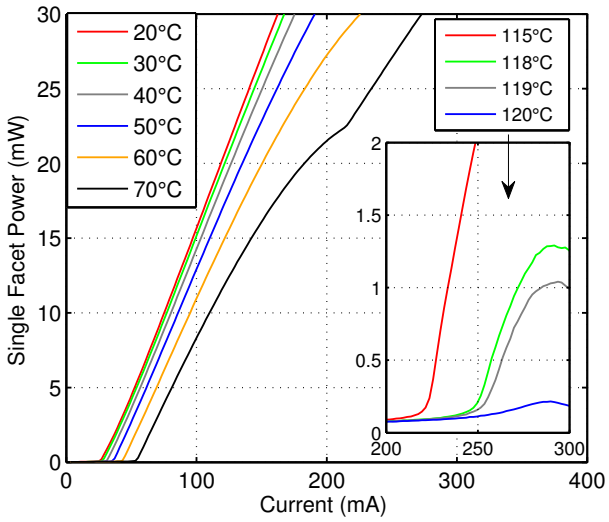

Figure 3.18: CW LI curves at various stage temperatures for a p-doped $993\times5\mu m^2$ HR/SiN laser. CW lasing is observed up to 119°C (see inset). Pulsed T_0 for this device is ∼140 K around room temperature. From [14], © 2014 AIP Publishing LLC.

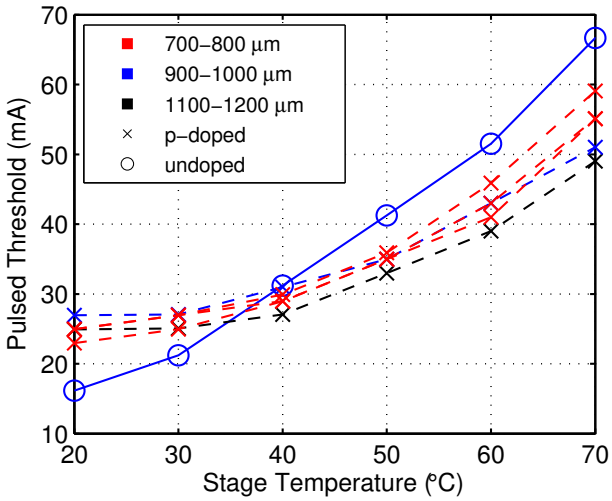

Figure 3.19: Pulsed threshold versus stage temperature for various p-doped devices (x) compared with the undoped device in Figure 3.14 (o). The different colors correspond to different cavity lengths. From [14], © 2014 AIP Publishing LLC.

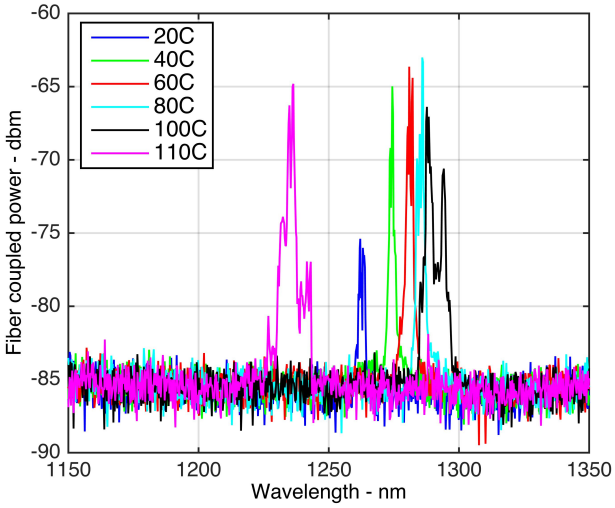

Figure 3.20: Lasing wavelength versus stage temperature for a p-doped HR/SiN laser in pulsed operation.

Yield data

Laser performance for ridges widths from 4 to 12 μm were studied. Mask splits for the ridge widths are 1×4 μm, 2×5 μm, 3×6 μm, 4×7 μm, 5×8 μm, 4×9 μm, 3×10 μm, 2×11 μm, 1×12 μm, hence less data points are available for the narrowest or widest ridges. The data presented in Figure 3.21-Figure 3.23 are of more than 330 working lasers from the two separately grown wafers.

Current-voltage (IV) data and visual inspection indicates that the main reason for turn-on failure are probe metal shorts, while other discrepancies in performance are primarily related to facet damage incurred during polishing (see Appendix B). The threshold data shows a remarkably linear trend over the entire range of ridge widths studied, implying minimum sidewall recombination and lateral carrier diffusion due to excellent carrier confinement within the quantum dots (inset of Figure 3.21)[41]. A histogram of the corresponding threshold current densities show a very narrow spread and implies excellent material uniformity across the two different chips (Figure 3.21). The lowest threshold current density was 253 A/cm^2, and with the average centered around 500 A/cm^2. Note

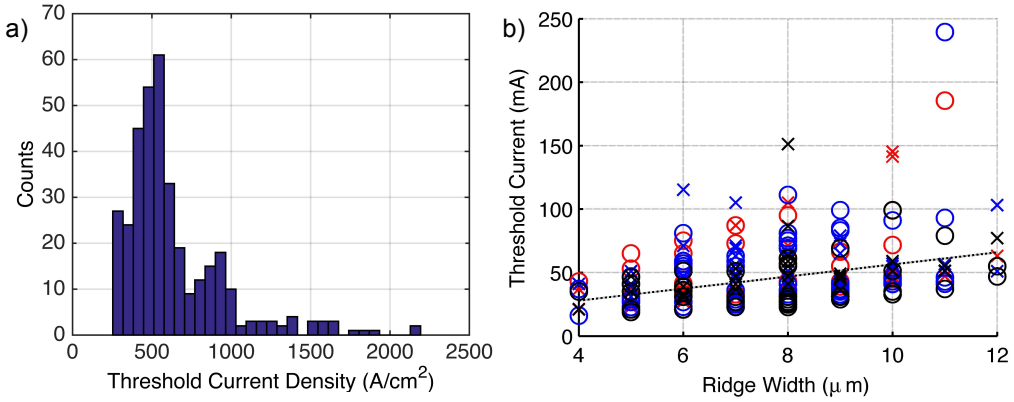

Figure 3.21: A) A histogram of CW threshold current density at 20°C (both p-doped and undoped). The lowest threshold current density was 253 A/cm^2, and with the average centered around 500 A/cm^2. b) Corresponding threshold currents plotted against ridge width, the dashed best fit line has a slope of 4.75 mA/μm.

that the difference in cavity lengths will induce a small spread in the average threshold current density as well, due to the difference in mirror loss. Similarly, output power increases more or less linearly with the ridge width, although the data is more scattered due to non-uniform facet polishing (Figure 3.22). The maximum output power versus the corresponding drive current (the roll-over inflection point in the LI curve) are plotted for all devices in Figure 3.23. The slopes of the best fit lines for the undoped and p-doped data points in this plot are 0.2252 and 0.1752 W/A, respectively, and can be used as a conservative estimate of the average slope efficiency for our devices. The higher slope efficiency of undoped laser devices are in agreement with the expected increase in optical loss from p-doping the active region, leading to slightly higher thresholds and lower slope efficiencies [63]. The highest output powers and lowest thresholds were from devices with intrinsic (undoped) active regions.

Overall the performance of the second generation devices were significantly improved from the first generation devices. This was mostly due to the improved growth conditions and epi design as detailed previously, as well as improved device processing and the application of HR coatings. The plot in Figure 3.24 illustrates the relative improvement

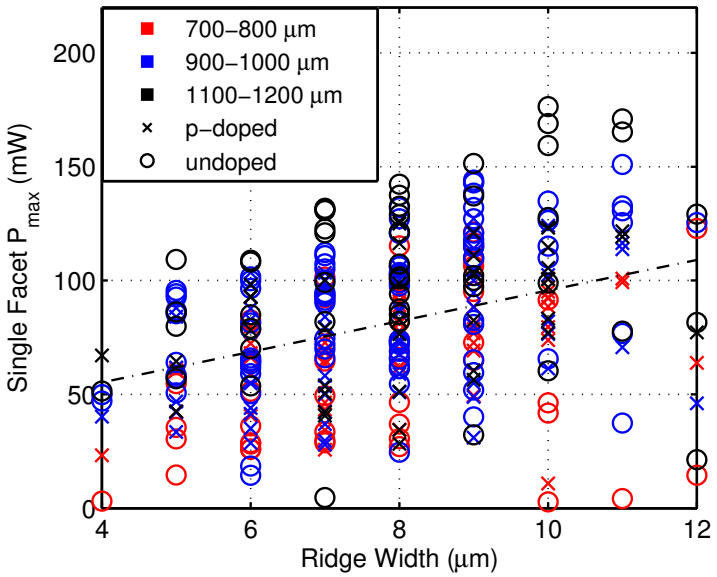

Figure 3.22: Maximum CW output power at 20°C (both p-doped and undoped) plotted against ridge width. The dashed best fit line has a slope of 6.73 mW/μm. From [14], © 2014 AIP Publishing LLC.

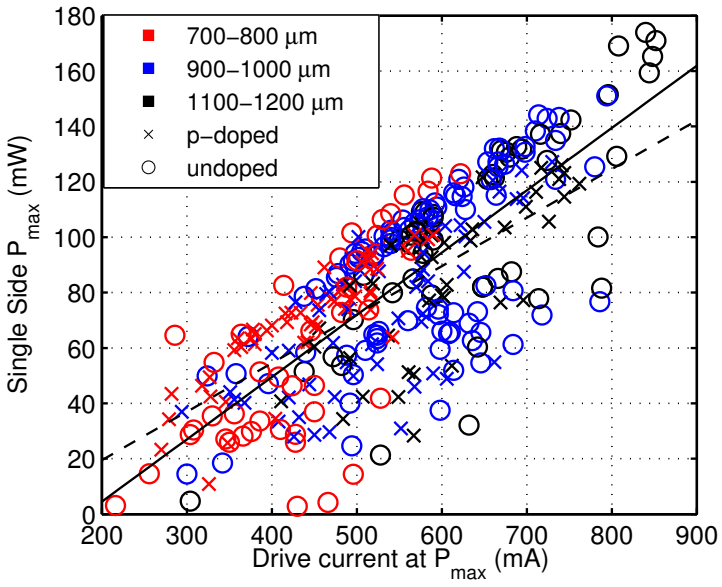

Figure 3.23: Maximum CW output power at 20°C (both p-doped and undoped) versus corresponding drive current. The solid and dashed lines are best fits for the undoped and p-doped devices with slopes of 0.2252 and 0.1752 W/A, respectively. From [14], © 2014 AIP Publishing LLC.

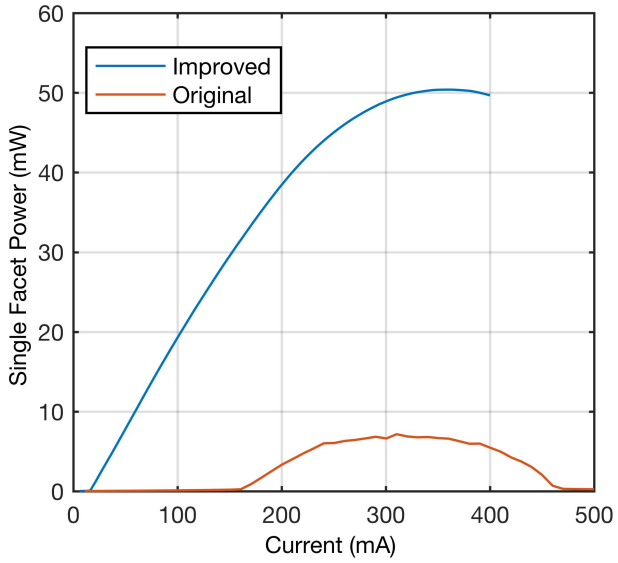

Figure 3.24: A LI comparison of lasers from the two different generations of devices. The 'original' curve is the laser on silicon shown in Figure 3.5, while the 'improved' curve is the device shown in Figure 3.14

between the two generations of devices.

3.3 Quantum dot versus quantum well lasers epitaxially grown on silicon

Up to this point we have been operating under the assumption that quantum dots are inherently more tolerant of dislocations compared to quantum wells. While our initial results of lasers on Ge/Si substrates are very good relative to previous lasers epitaxially grown on silicon, we cannot claim *a priori* that this is solely due to the benefit of having a quantum dot active region. Therefore we set out to conduct a systematic comparison with quantum well lasers grown on the same Ge/Si substrates, having the same layer structure and device design/fabrication steps as the quantum dot lasers. The goal is to compare both the relative change in performance of either quantum dots or quantum wells

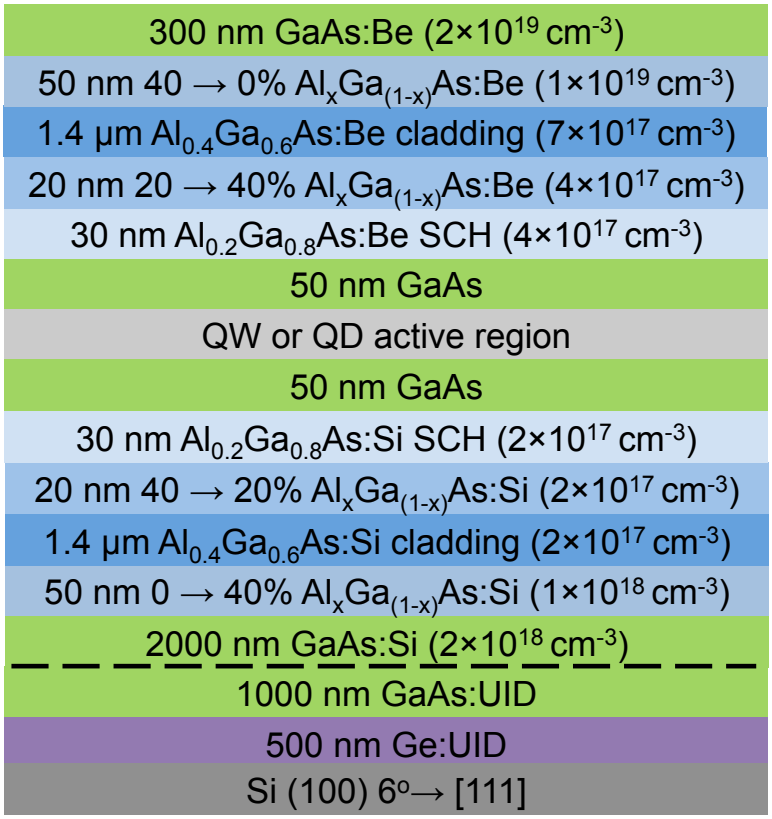

Figure 3.25: Layer structure of the QW or QD GaAs/AlGaAs lasers on silicon. From [35], © 2015 Chinese Laser Press.

for the same lasers on GaAs versus Ge/Si substrates, as well as the relative performance of quantum dots to quantum wells on the same substrates.

3.3.1 Experimental Procedures

Ideally we would compare the same material system at the same wavelength of 1.3 μm. However the emission wavelength of InGaAs/GaAs quantum wells is limited to around 1100 nm by the strain of the system, as longer wavelengths require high indium content and/or thicker wells that are likely to cause inelastic strain relaxation and misfit dislocation formation. $In_{0.20}Ga_{0.80}As$/GaAs quantum well (QW) lasers emitting around 980 nm are one of the most mature laser systems on GaAs and also well developed at

UCSB by the Coldren group for high speed VCSELs. They were thus chosen for this study to compare with 1.3 μm InAs/GaAs quantum dot (QD) lasers. The following cases are examined:

- InGaAs QW lasers vs. InAs QD lasers on native GaAs substrates (dislocation density $\leq 10^3$ cm^{-2})
- InGaAs QW lasers on silicon vs. InAs QD lasers on silicon (dislocation density $\geq 10^8$ cm^{-2})

Both photoluminescence (PL) and full laser structures are studied. Growth was performed by Molecular Beam Epitaxy (MBE). The PL structures consist of a single QW or QD active region cladded on either side by GaAs (50 nm)/$Al_{0.40}Ga_{0.60}As$ (50 nm)/GaAs (50 nm). Growth procedures for the QDs have been reported previously [59]. Growth conditions for the QW are: 8 nm of $In_{0.20}Ga_{0.80}As$ grown at 2.23 A/s, 530°C, and under a V/III ratio of 20.

GaAs/$Al_xGa_{1-x}As$ laser structures were grown with either 3×[$In_{0.20}Ga_{0.8}As$ (8 nm) / GaAs (8 nm)] multiple quantum wells, or InAs QD/GaAs (37.5 nm) multiple quantum dot layers (five for lasers on GaAs and seven for lasers on silicon) (see Figure 3.25). Samples on GaAs were grown on cleaved pieces of a semi-insulating two inch GaAs (100) wafer, and samples on silicon were grown on 2×2 cm^2 pieces diced from a 150 mm GaAs (1 μm)-on-Ge (500 nm)-on-Si template provided by IQE, the same ones as was used in the above sections. The as-grown epi were then processed into either broad area or narrow ridge waveguide lasers using standard lithography, dry etching, and metallization techniques.

3.3.2 Results and discussion

Broad area laser and modal gain characteristics

50 μm wide broad area lasers with as-cleaved facets were first fabricated from the GaAs wafers with either 5x InAs/GaAs quantum dots or 3x InGaAs quantum wells as the active region to assess the quality of the active region. For each type of laser (QD or QW), the light-vs-current (LI) characteristics for lasers with various cleaved cavity lengths were measured on over 100 devices. From the measured LI curves, the inverse of the external differential quantum efficiency was plotted against the cavity length, as shown in Figure 3.26. Injection efficiency (η_i) and optical loss (α_i) were extracted from the best fit line of the average inverse differential efficiency versus the cavity length. The extracted values for the injection efficiency and waveguide loss are: $\eta_i = 0.61 \pm 0.04, \alpha_i = 3.17 \pm 0.41$ cm^{-1} for the QD lasers; and $\eta_i = 0.64 \pm 0.03, \alpha_i = 6.79 \pm 0.59$ cm^{-1} for the QW lasers. Pulsed measurements with a duty cycle of 0.5% (5 μs pulse width, 1000 μs pulse period) were used for this analysis, although continuous wave measurements were also performed with both quantum well and quantum dot lasers demonstrating good performance at room temperature.

Subsequently, a modal gain ($\Gamma g_{th} = \frac{1}{L}\mathrm{Ln}\frac{1}{0.32} + \alpha_i$) versus current density curve was generated by plotting the modal gain versus average threshold current density of each different cavity length. Also plotted are the average threshold current densities as a function of cavity length, both of which are shown in Figure 3.27. The modal gain versus current density curve was fitted with a simple logarithmic function: $\Gamma g_{th} = \Gamma g_{0J} Ln(J/J_{tr})$. The extracted average transparency current density J_{tr} per layer of quantum dots is 11.6 A/cm^2, and 72.8 A/cm^2 for the quantum wells. The gain coefficient Γg_{0J} is 2.36 cm^{-1} per layer of quantum dots, and 19.26 cm^{-1} per layer of quantum wells. We see that in low loss cavities, quantum dots hold a significant advantage in terms of lower transparency

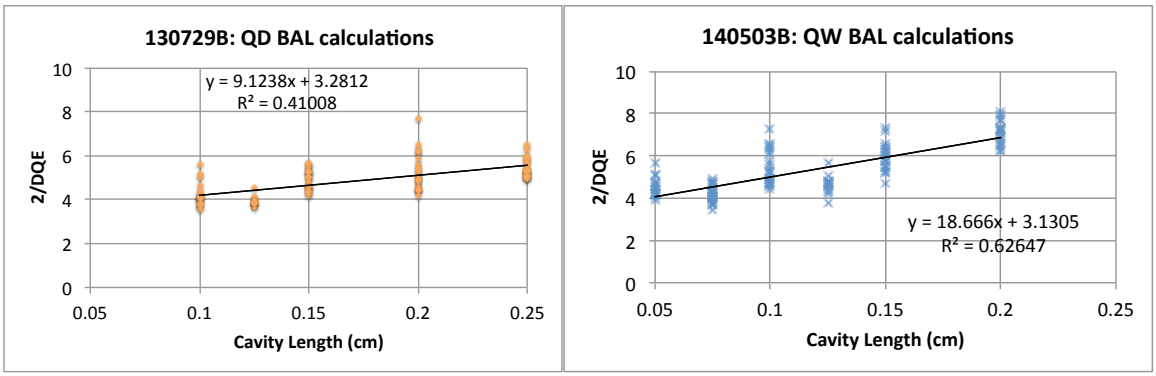

Figure 3.26: Broad area laser cut-back measurements of $In_{0.2}Ga_{0.8}As$ quantum well and InAs quantum dot lasers on GaAs substrates. In each case various cavity lengths were measured in pulsed mode, and the inverse external differential quantum efficiency plotted against cavity length, then fitted to a line to extract the modal loss and injection efficiency.

and threshold current density. Note that for all plots and analysis shown here the current density value plotted is the total experimentally applied current density, before any injection efficiency losses (i.e. not $\eta_i \times J_{applied}$). In general both types of active regions were performed reasonably well for the devices on GaAs.

This analysis which relies on measurements of the external differential quantum efficiency assumes complete pinning of the Fermi levels past threshold. This assumption may not be completely valid for the analysis of quantum dot lasers, for which the carrier density (and η_i) may not completely pin at threshold but can still increase slightly with increasing current density [66]. This is a result of the inhomogeneous broadening and non-equilibrium carrier distribution within quantum dot ensembles. More measurements and simulations will be necessary to address this issue, which is beyond the scope of the present investigation.

Photoluminescence comparison

Room temperature PL spectra of the same QW or QD structure grown on GaAs versus silicon is shown in Figure 3.28. While the ground state intensity of the QW

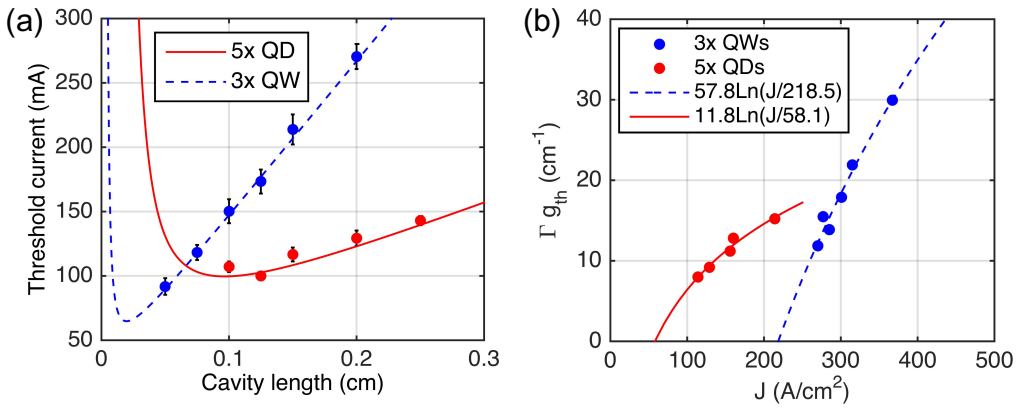

Figure 3.27: Room temperature broad area laser characteristics of $In_{0.2}Ga_{0.8}As$ quantum well and InAs quantum dot lasers on GaAs substrates: (a) threshold current versus cavity length and (b) modal gain versus injected current density. Fitting parameters are listed in Table 7.1. From [35], © 2015 Chinese Laser Press.

degraded by more than a factor of 10 when grown on silicon, the ground state intensity of the InAs QDs is roughly 80% of the reference QDs grown on GaAs with comparable linewidths (∼35 meV).

Cross-sectional TEM comparison

Cross-sectional transmission electron microscopy (TEM) images of the QD and QW laser structures grown on silicon are shown in Figure 3.29. Similar dislocation densities are observed for both structures, thus we may infer that the dislocation densities in the PL structures grown on silicon are also comparable (since the substrates were all diced from the same parent wafer).

Ridge laser comparison

Ridge waveguide lasers were fabricated from the two different kinds of laser epi on silicon using the same fabrication procedure as described in the earlier sections. Contact resistance measured from devices on the two separate silicon based epi were similar at around $1\times10^{-6}\Omega$ cm^2, as to be expected since doping levels were nominally identical and

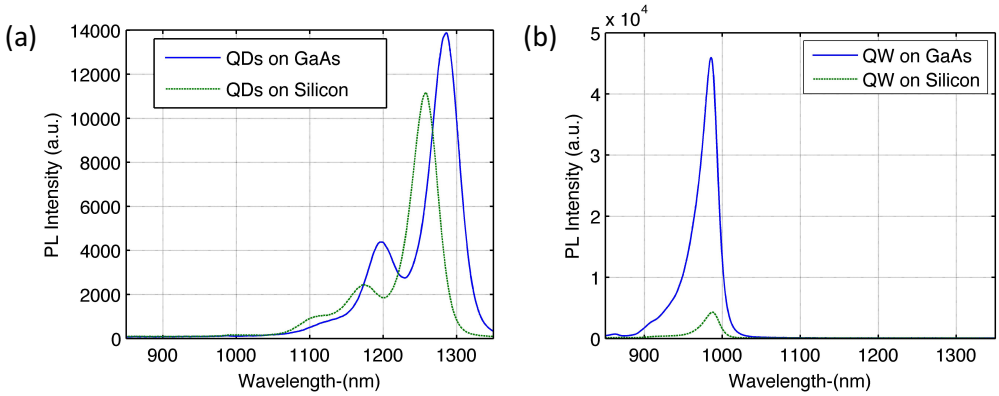

Figure 3.28: Room-temperature photoluminescence comparison of (a) single InAs quantum dot layer and (b) single 8 nm $In_{0.20}Ga_{0.80}As$ quantum well grown on GaAs versus silicon substrates. From [35], © 2015 Chinese Laser Press.

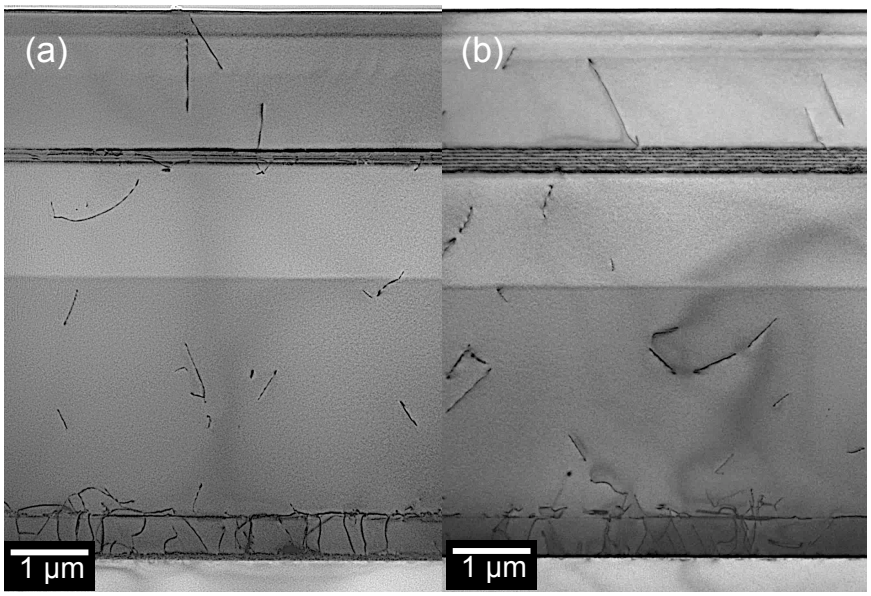

Figure 3.29: Bright field cross sectional TEM images of (a) the QW laser and (b) the QD laser grown on silicon. Dislocations manifest as irregular dark lines. (Scale is approximate). From [35], © 2015 Chinese Laser Press.

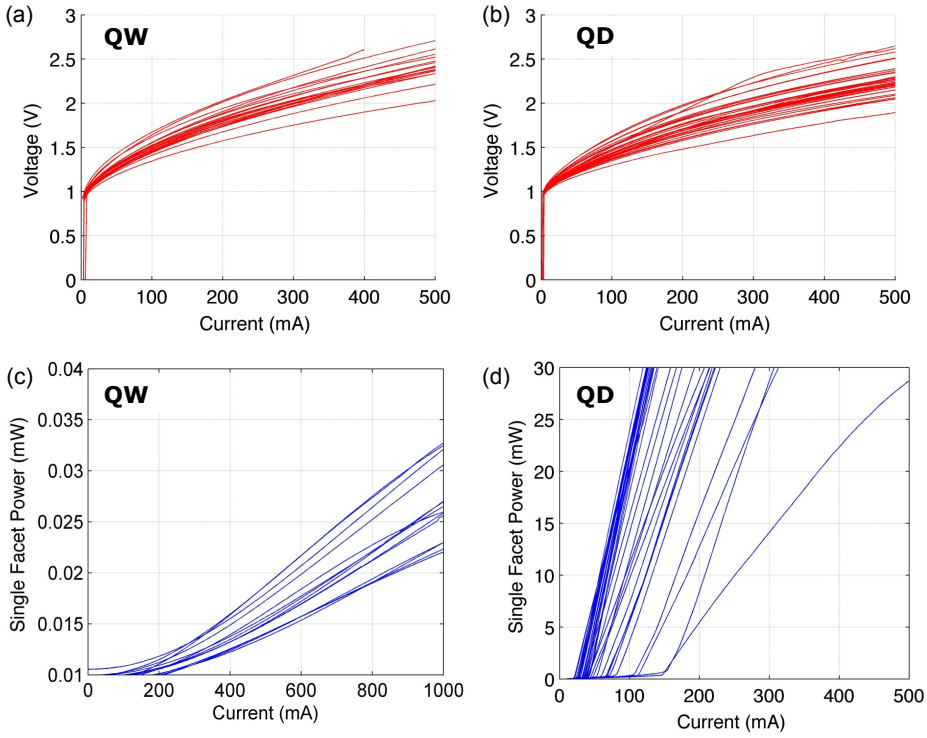

Figure 3.30: Room-temperature continuous wave current-voltage (a-b) and light-versus-current (c-d) plots for both the $In_{0.20}Ga_{0.80}As$ quantum well (a, c) and InAs quantum dot lasers (b, d) grown on silicon substrates. From [35], © 2015 Chinese Laser Press.

the metallization procedures were the same. I-V characteristics between devices from the two separate wafers also show similar series resistance (Figure 3.30 a&b). However, contrary to the case of the two lasers on GaAs substrates, in this case none of the quantum well devices were able to achieve continuous wave lasing at room temperature (Figure 3.30c). In comparison, the InAs quantum dot lasers grown on silicon show very reasonable continuous wave lasing characteristics, shown in Figure 3.30d and reported in detail in the previous sections [14]. The turn-on voltage of the quantum well lasers are also lower than what would be expected from the bandgap of the quantum wells, indicating some possible current leakage. These results clearly confirm the hypothesis that quantum dot lasers can be much less sensitive to dislocations compared to quantum wells.

3.4 Summary

We have demonstrated repeatable record performance 1.3 μm InAs quantum dot lasers epitaxially grown on silicon with low thresholds (16 mA), high output power (176 mW), high temperature lasing (up to 119°C), and high T_0 (> 200 K). These continuous wave output power levels and lasing temperatures are the highest reported for lasers on silicon. These results are a significant improvement from the first generation devices, resulting from a combination of improved quantum dot growth, device design, and device fabrication. We have also provided a systemic study of InAs/GaAs quantum dot versus $In_{0.15}Ga_{0.85}As$/GaAs quantum well lasers grown on the same Ge/Si substrates and with the same device design/fabrication process. The results of the latter study show unequivocally the reduced sensitivity to dislocations of quantum dot active regions compared to quantum wells.

Chapter 4

Reliability of InAs/GaAs quantum dot lasers on Ge/Si

4.1 Introduction

GaAs/AlGaAs compounds are known to be susceptible to recombination enhanced defect reactions, whereby energy released from non-radiative recombination at point defect or extended defect (dislocation) sites contribute to a local enhancement of defect/dislocation mobility and density [67]. This phenomenon is a common cause of failure in GaAs/AlGaAs quantum well lasers, and becomes more pronounced with higher dislocation densities [68, 11]. For GaAs based quantum well lasers epitaxially grown on silicon - where relatively high dislocation densities are present compared to growth on native substrates - reported lifetimes have ranged from a few seconds [69] to around 200 hours [70] under room temperature testing.

Long-term reliable operation is a pre-requisite for consideration in commercial applications. There have been several reports on the reliability of InAs/GaAs quantum dot lasers grown on native GaAs substrates [71, 72, 31], however the reliability charac-

teristics of previous quantum dot lasers epitaxially grown on silicon have not yet been reported. Here we present the first study on the reliability of InAs/GaAs quantum dot lasers epitaxially grown on silicon and a comparison with similar devices grown on GaAs.

4.2 Experimental procedure

Ridge waveguide Fabry-Perot cavity lasers were fabricated from InAs/GaAs quantum dot laser material emitting around 1.3 μm grown by molecular beam epitaxy on both native (100) GaAs substrates as well as GaAs/Ge/Si templates [14, 59], where the Si substrate is (100) with a 6° miscut towards [111]. The growth and fabrication steps of all the lasers used for reliability testing were identical except for the choice of substrate (GaAs vs. GaAs/Ge/Si), the number of active layers (five on GaAs substrates and seven on GaAs/Ge/Si), and the facet formation process. For the lasers grown on silicon, the cavities were defined by dicing the metallized chips into laser bars, facet polishing, deposition of a thin 20-25 nm SiN passivation layer on both facets and a 95% highly-reflective (HR) dielectric coating on one facet. The lasers on GaAs were cleaved with no subsequent facet coating. Detailed epitaxial growth and device fabrication procedures have been reported previously [14, 59].

Figure 4.1 shows a cross-sectional transmission electron microscope (XTEM) image of unprocessed laser material on silicon from a separate wafer but grown with the same conditions as the material used for device fabrication. The viewing area is $\sim 11\mu$m wide. A high density of threading dislocations is visible. Despite the high density of dislocations, lasers fabricated from such material have shown reasonably good performance as characterized in detail in Chapter 3, demonstrating the unique advantage of quantum dots.

Nine devices of various sizes were selected for aging in an accelerated aging test rack

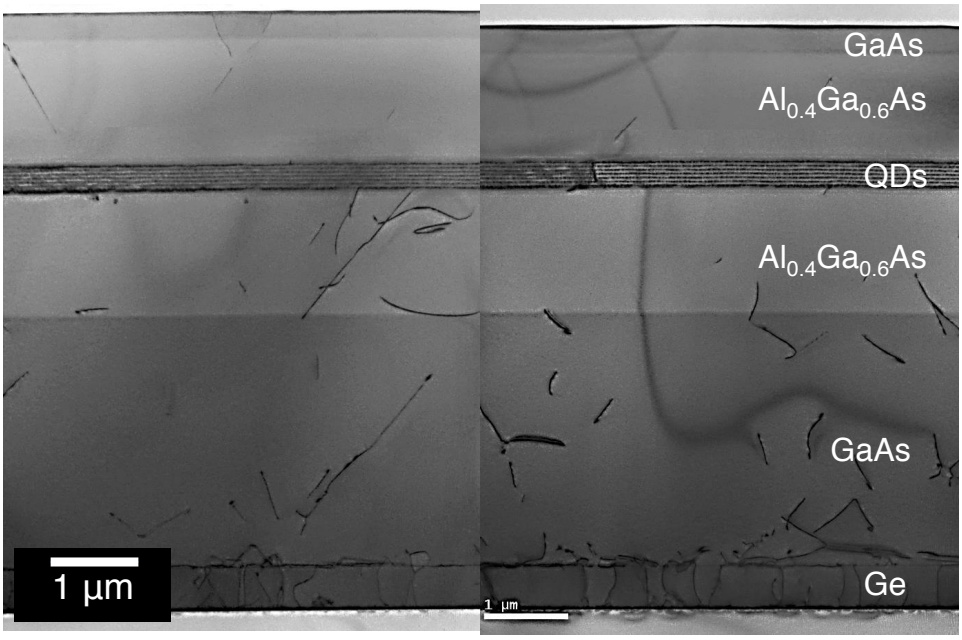

Figure 4.1: Cross-sectional TEM (XTEM) of the as-grown laser epi on Ge/Si sustrates. The threading dislocation density is estimated to be 4×10^8 cm^{-2}. From [23], © 2015 IEEE.

at Aurrion Inc. Of the selected devices, three were quantum dot lasers grown on GaAs substrates, while the rest were on silicon. Laser bars containing one or more individual devices to be tested were mounted onto AlN carriers with non-conductive epoxy and the contacts wire-bonded to probe pads on the carrier. A thermistor was mounted onto the carrier as well to monitor the temperature during aging.

All devices were aged in auto current control (ACC) mode at 30°C under 100 mA of constant applied current (1.1-2.5 kA/cm^2 depending on device size). The initial single facet output powers at these conditions varied from 3.3-16.6 mW. Periodic light-current-voltage (LIV) sweeps at 30°C were taken to monitor changes in the lasing characteristics, where the light was collected from a photodiode normal to the facet of the aged devices in the aging rack. Due to limitations of the mask layout and the wire-bonding setup, only a single wire-bond was done for the p and n contacts of each laser - namely due to the small size of the probe pads compared to the minimum achievable wirebond size

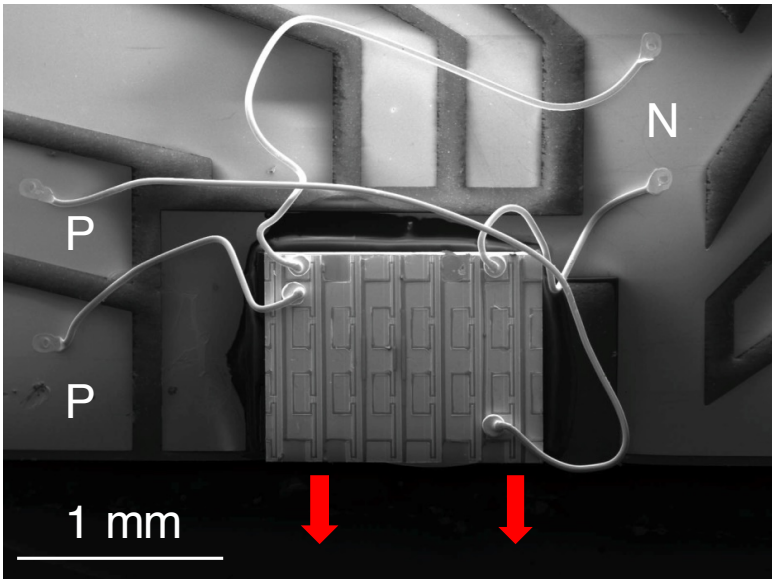

Figure 4.2: A SEM photograph of the packaged laser for lifetime testing. Two devices are being aged in this case. The thermistor is not visible. The original mask design constrained us to a single n and p wire bond per device.

(see Figure 4.2). Because of this, the differential resistance of the wire-bonded lasers at the aging current of 100 mA increased by 0.205-0.735 ohms compared to direct probing. This manifested in a reduced maximum output power and earlier thermal rollover in the LI curves of the mounted/wire-bonded lasers measured at room temperature.

One additional laser on silicon was tested in-house at UCSB so as to be able to perform additional characterization during the aging process (Figure 4.4, VII). In this case, a packaged laser device on an AlN carrier without any wire bonding was directly probed on a heated copper stage and operated continuously using a Keithley 2602 current source. Periodic LIV sweeps were programmed with a MATLAB script and the output light was collected with an integrating sphere. With the exception of modulation p-doping in the active region, the epitaxial material and device structure were identical to the ones tested at Aurrion.

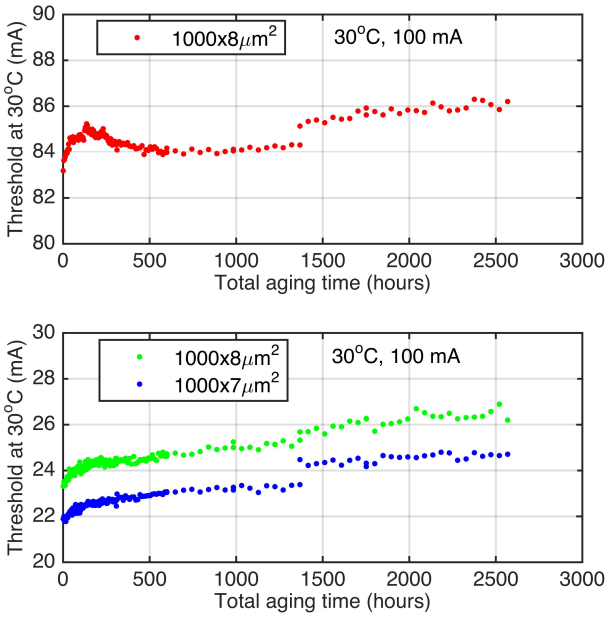

Figure 4.3: Aging data (at 30°C/100 mA) for three quantum dot lasers on GaAs. The discontinuity around 1400 hours coincides with relocation of the testing equipment. The legends denote the device size as (cavity length) x (ridge width). From [23], © 2015 IEEE.

4.3 Lifetime testing results

4.3.1 Threshold behavior

Figure 4.3 shows the aging data for the quantum dot lasers on GaAs. A small increase in threshold (2-3 mA) over the course of the aging period is observed for all lasers, with most of the increase occurring in the early stages of testing. The threshold behavior was otherwise relatively stable. Sudden kinks in the threshold versus time plots at around 1400 hours coincide with relocation of the testing setup.

Figure 4.4 shows the aging data for the lasers on silicon. The data is grouped into three subsets according to active region area/applied current density for the devices stressed together in the aging rack (labeled I through VI), and separately for the p-doped laser aged on a probe station (VII). The lasers can be seen to degrade at various rates during

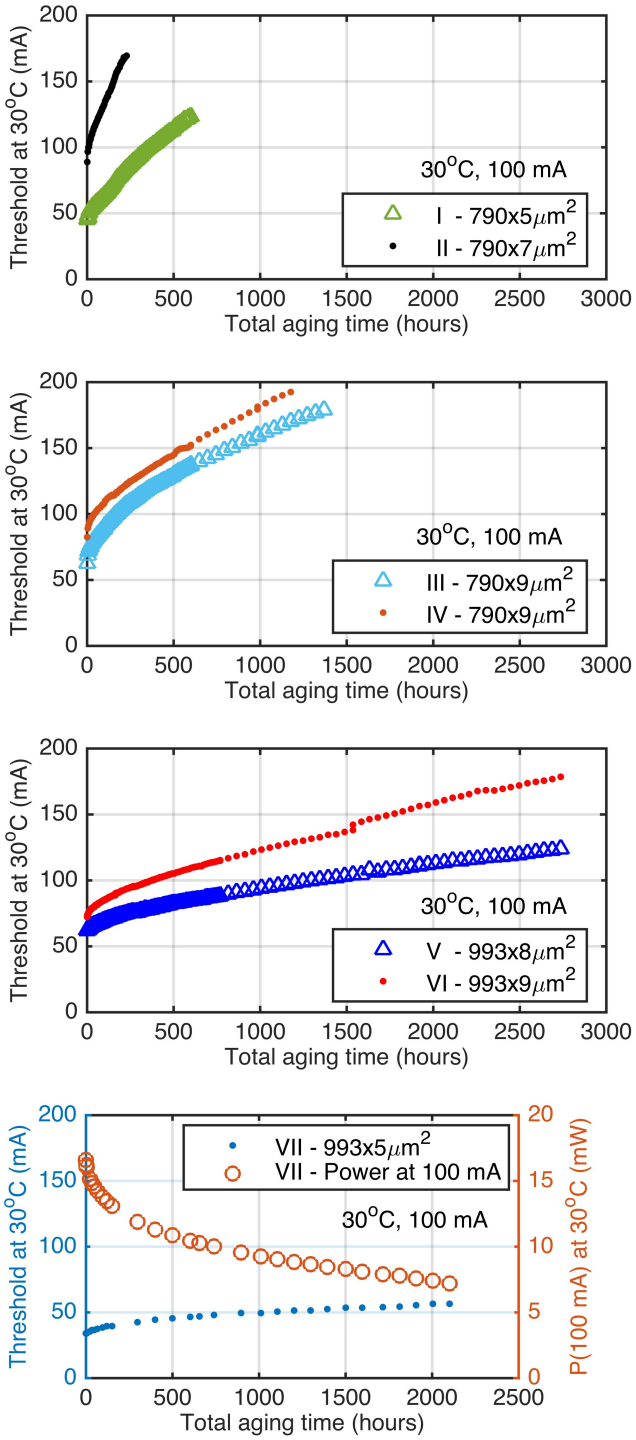

Figure 4.4: Aging data (at 30°C/100 mA) for six quantum dot lasers on silicon stressed in a commercial laser reliability aging test rack (I-VI). VII is a laser with p-doping in the active region and stressed on a probe station. The legends denote the device size as (cavity length) x (ridge width). From [23], © 2015 IEEE.

the aging process, but no catastrophic failures are observed. Devices II, III and IV slowly degraded until the threshold was too high to permit lasing. After 600 hours, devices I (still lasing) and II were removed for TEM characterization. Aging of V, VI, and VII were stopped after 2736, 2736, and 2100 hours, respectively.

A sub-linear model is used to fit the threshold behavior over time as was proposed in an earlier work [73, 74]:

$$I_{th}(t) = I_{th}(0)(1 + at^m)$$

$$MTTF = \left(\frac{1}{a}\right)^{1/m}$$

In the above equations, t is the elapsed aging time and $I_{th}(t)$ is the threshold as a function of aging time. The MTTF criterion can take on various levels of rigor depending on the device application. Here we define it as a doubling of the threshold for ease of comparison with similar reliability data of epitaxial lasers on silicon. The p-doped laser showed the best lifetime with an extrapolated MTTF of 4627 hours. Typically, semiconductor laser lifetime is modeled by a temperature and applied current density dependence:

$$MTTF = AJ^{-n} \exp\left(\frac{E_a}{kT}\right)$$

where T is the junction temperature, E_a is an activation energy that describes the change in degradation rate across a temperature range, and n describes the current-density dependence on degradation. MTTF versus applied current density is plotted in Figure 4, and the current exponent is estimated to be ~ 2.7 for devices I-VI (data for VII was not included for consistency because of the different gain characteristics and carrier dynamics of p-doped lasers, as well as the different testing setup). We note that this is only a rough estimate due to the small sample size as well as other effects present, which cannot be properly decoupled such as differences in thermal and electrical resistances of different

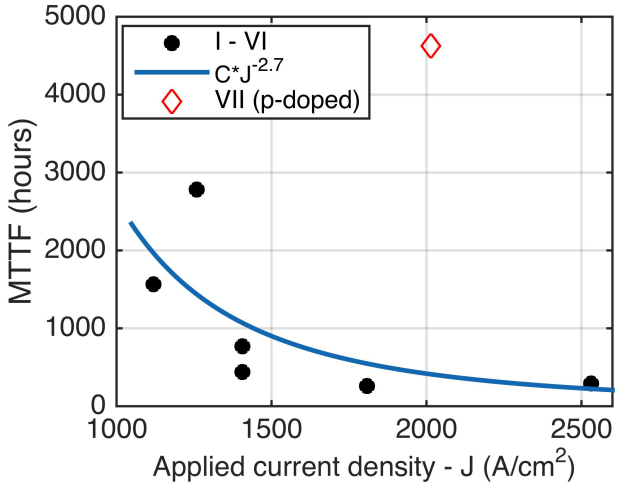

Figure 4.5: MTTF versus the applied current density for devices I-VII. The blue line is a best fit curve for devices I-VI (VII not included due to the different testing setup and p-doping in the active region). The current exponent n is approximately 2.7. From [23], © 2015 IEEE.

device sizes. Due to lack of temperature dependent data we are unable to estimate the thermal activation energy.

4.3.2 (S)TEM investigation

Plan-view TEM (PVTEM) specimens were prepared from device I which has been heavily degraded after 600 hours, as well as unaged devices spaced approximately 300 μm away on the same laser bar for comparison. The PVTEM specimens were taken from approximately the center of the InAs quantum dot active region, and estimated to be 100-120 nm thick, with ∼20 nm of amorphous material on each side of the foil caused by FIB damage. Due to significant warping of the TEM foils causing irregular diffraction conditions across the sample, the images were taken in multi-beam diffraction conditions in STEM mode to best illuminate the dislocations. The results are visible in Figure 4.6. A network of misfit dislocations is visible in both the aged device as well as the unaged one, which was not readily observable in cross-sectional TEM. The majority

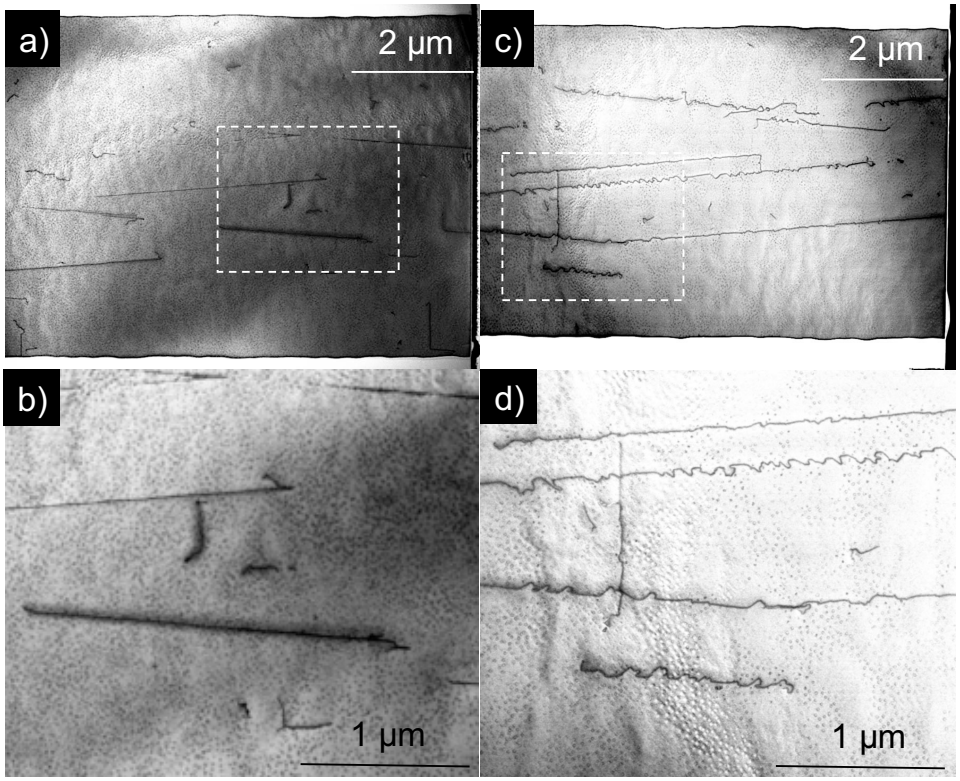

Figure 4.6: Plan-view TEM images of the active region of an unaged laser (a & c), and that of device II which was aged for 600 hours (b & d). Boxed regions in a&b correspond to the regions where c&d were imaged, respectively. The speckled background is due to individual quantum dots. The dislocation density is on the order of 10^8 cm^{-2} in both cases. The helical component of the misfit dislocations in the aged sample is characteristic of dislocation climb. From [23], © 2015 IEEE.

of them are aligned nearly parallel to the [011] direction separated by an angle that is proportional to the substrate offcut [75], forming V shapes where they cross. The total dislocation density is on the order of $\sim 10^8$ cm^{-2} in both cases. Comparing the aged and un-aged cases, the dislocations in the aged device seem to acquire a helical component, characteristic of growth by dislocation climb [76]. We note that this device (I) was still lasing with roughly 4 mW of maximum output power at the time testing was stopped for TEM characterization.

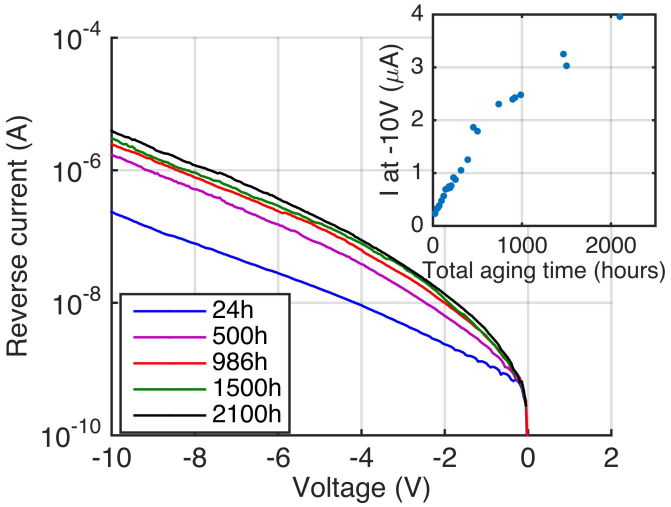

Figure 4.7: Reverse leakage current for device VII measured in roughly 500-hour intervals at the aging temperature of 30°C. Inset: reverse current at -10V as a function of aging time. From [23], © 2015 IEEE.

4.3.3 Reverse bias leakage current versus aging time

The reverse bias leakage current was measured at different aging time intervals for device VII at 30°C. The results are shown in Figure 4.7. After a relatively large initial increase in the leakage current, the rate of increase becomes smaller for roughly the same time interval as aging progresses (see inset of Figure 4.7). This trend is similar to the threshold versus time data. Materials with defects or dislocations typically exhibit much higher reverse leakage currents compared to low defect density material [76, 77, 78]. This suggests that the degradation is due to defect/dislocation growth within the material, and is consistent with the observation of dislocations with signatures of climb in Figure 4.6.

4.3.4 Post-aging lasing spectra

Figure 4.8 shows the lasing spectra at 30°C for device VII after the aging process was stopped at 2100 hours. The measured threshold after 2100 hours of testing was 57 mA at the aging temperature. Sharp lasing peaks at the wavelength of 1267 nm are visible in

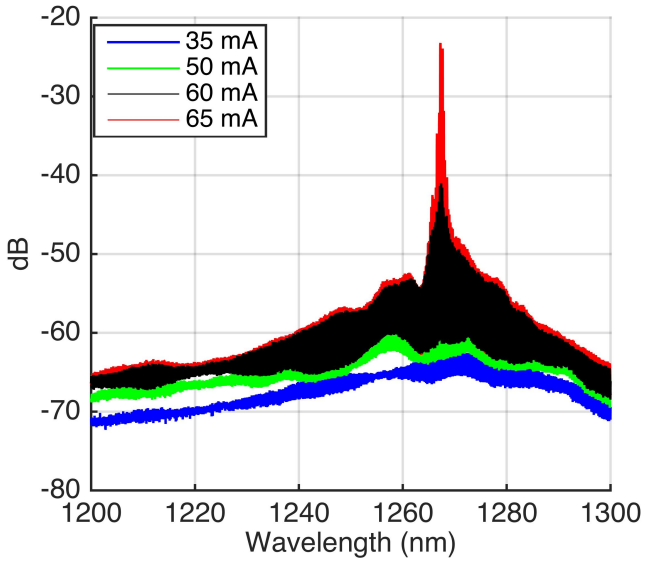

Figure 4.8: Lasing spectra at 30°C for device VII after 2100 hours of lasing. A lasing peak at the wavelength of 1267 nm appears at 60 mA and becomes well developed by 65 mA, confirming lasing action in this device. From [23], © 2015 IEEE.

the lasing spectra at 60 mA and become well developed at 65 mA, confirming sustained ground state lasing oscillation during and after the aging process.

4.4 Discussion

Since the quantum dot (QD) lasers grown on GaAs exhibited good lifetime characteristics, we conclude that the degradation of QD lasers on silicon is caused by either the higher dislocation density from growth on silicon and/or damage induced from the facet polishing process (examples are given in Appendix B). While we cannot rule out the latter, for applications in silicon photonic integrated circuits facets are either formed in a passive waveguide material decoupled from the active gain media or not used at all, making III-V facet damage less relevant for reliability [74]. We will focus our discussion on the evidence of dislocation growth in the active region. Both threading dislocations and misfit dislocations are present within the lasers on silicon at high densities, visible

in the TEM images in Figure 4.6. The high density of misfit dislocations in the active region was unexpected and could have been caused by relaxation of the $In_{0.15}Ga_{0.85}As$ quantum well confining the QDs. A literature survey of GaAs based lasers grown on silicon reveals a surprising finding: despite the fact that pseudomorphically strained $In_xGa_{(1-x)}As$/GaAs quantum well (QW) lasers significantly outperform their unstrained GaAs QW counterparts when grown on GaAs, the opposite is true for the same lasers on silicon where InGaAs QWs have failed to show the same superior performance compared to unstrained GaAs/AlGaAs QW devices [79, 80, 81]. Although the reason has not been extensively investigated, it is possible that this is due to a metamorphic relaxation of the strained InGaAs typically grown near the critical thickness on GaAs. Extra compressive strain induced by the temperature increase from quantum well/dot growth temperatures to hotter GaAs growth, along with an increased possible number of nucleation sites for misfit dislocations from the presence of pre-existing threading dislocations and an inherent surface roughness, likely induces an earlier critical thickness for plastic relaxation of the InGaAs QWs (or InAs QDs). Increased misfit dislocations in the QW when grown on Si versus growth on native substrates have also been observed experimentally by TEM in a recent study [81].

Although strained InGaAs quantum well lasers show significantly improved lifetimes compared to unstrained quantum well lasers, it has been demonstrated that when grown near or past the critical thickness, their lifetimes become worse than those of unstrained GaAs quantum well lasers [82]. The study in [82] looked at three sets of lasers where the quantum well thickness varied by approximately 2 nm. The corresponding lifetimes varied from well over 3000 hours for the laser that was below the critical thickness, to 1000 hours near the critical thickness, to less than 100 hours above the critical thickness. Therefore, the creation of extra misfit dislocations possibly related to the strain relaxation of the DWELL may be an important factor in the lifetime of these devices. In many studies,

the same growth conditions are used to compare material grown on GaAs to growth on Si for consistency. However, in light of this analysis, this is not an optimal route as the same growth conditions on GaAs may exceed the critical thickness on silicon. Strain compensation via the introduction of tensile barriers or proper adjustment of the layer composition and thickness should be made for growth on silicon for better reliability. Degradation in this case most likely proceeds via non-radiative recombination of minority carriers at such dislocations outside the InAs QDs (i.e. in the confining $In_{0.15}Ga_{0.85}As$ well and GaAs barriers), which leads to subsequent dislocation climb. This recombination enhanced process has been shown to be proportional to the current density [67, 83], which in the active region is governed by the lasing threshold condition involving different competing carrier processes such as carrier capture and escape within individual dots or defect states.

4.5 Degradation model

A schematic in-plane band diagram illustrating the various processes present is shown in Figure 4.9. The non-radiative lifetime associated with a defect or trap state can be roughly expressed as $\tau_{NR} = 1/(\sigma v_{th} N_D)$ where σ is the capture cross-section of the defect, v_{th} is the thermal velocity of the minority carrier, and N_D is the defect density. The internal quantum efficiency can then be expressed as [84]:

$$\eta_{IQE} = \left(1 + \frac{\tau_r}{\tau_{NR}}\right)^{-1} = (1 + \tau_r(\sigma v_{th} N_d))^{-1} = (1 + C(\sigma N_D))^{-1} \tag{4.1}$$

For QD lasers, the capture cross-section of the defect would be inversely proportional to the dot density (or the mean diffusion length). As the dislocation length increases through recombination enhanced dislocation climb, the the product σN_D increases causing de-

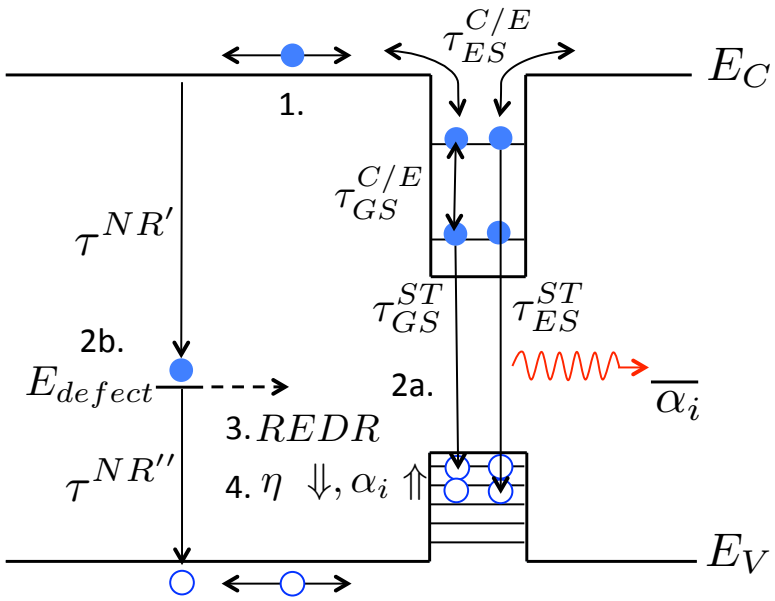

Figure 4.9: A simplified schematic of the aging process showing the various capture (C), emission (E) and recombination (non-radiative: NR; or radiative/stimulated emission: ST) processes involved. Only electron processes are shown for simplicity. Here, the defect is an electron trap. When carriers are injected into the active region (1), they may relax via radiative transitions if captured by a quantum dot (2a) or a non-radiative transition if trapped by a defect (2b). In the latter case, recombination enhanced defect reactions (REDR) may lead to growth or formation of new defects (3). Laser efficiency (internal quantum efficiency η_{IQE} inside active region, injection efficiency η_i outside active region) decreases and absorption loss increase(4). (GS ground state; ES excited states).

creases in the injection efficiency and/or internal quantum efficiency, while introducing additional absorption loss α_i into the cavity. This subsequently increases the threshold current density within the device, and leads to more non-radiative recombination events [11, 85].

Consider the recombination enhanced defect reaction mechanism, which is at the heart of the degradation process. The basis of this reaction is that thermal energy released from a non-radiative recombination (NRR) process helps to overcome an activation energy barrier for the growth of dislocations, ostensibly through migration of point defects.

This enhanced reaction rate can be given by [67]:

$$R_{RE} = \eta \frac{\exp[\Delta S/k]}{N_i} R_{nr} \exp[\frac{-(E_m - E_{nr})}{kt}] \tag{4.2}$$

where $\exp[\Delta S/k]$ is an entropy factor, N_i is the number of diffusion jumps required to each the final state, and η is an efficiency factor representing the probability that only a small fraction of recombination events will result in the configuration that allows activation over the migration barrier. This factor is usually $\ll 1$, and for GaAs it is $\approx 10^{-3}$ [67, 86]. Setting the valence band maximum as our reference energy, the maximum possible energy released from a non-radiative recombination at a trap is the trap energy itself E_d, so the equation becomes:

$$R_{RE} = \eta \frac{\exp[\Delta S/k]}{N_i} R_{nr} \exp[\frac{-(E_m - E_d)}{kt}] \tag{4.3}$$

The reaction in consideration is the absorption of point defects (either native to the material or created by bond breaking and emission of vacancies) to already existing extended defects, thus resulting in an increase in the dislocation length and effective defect density. Here we must make a clarification: although point defects may also have

an associated energy level with them, rapid degradation is typically associated with the growth of extended defects such as dislocations, therefore we take trap or defect levels here to mean dangling bond levels associated dislocations [87]. We further assume that the rate limiting step in this reaction is the concentration of dislocations, i.e. the reaction rate is independent of the point defect concentration in the material.

Ignoring Auger recombination in this analysis, the non-radiative component of the threshold is assumed to be purely due to Shockley-Read-Hall (SRH) recombination. This recombination rate, assuming equal capture cross sections of electrons and holes for simplicity, is defined as [84]:

$$R_{nr} = R_d = \sigma v_{th} N_d \frac{pn - n_i^2}{n + p + 2n_i cosh\frac{(E_d - E_i)}{k_b T}} \tag{4.4}$$

Where σ is the capture cross section in cm^2 of the defect, $v_{th} = \sqrt{3k_B T/m^*}$ is the thermal velocity ($\approx 10^7$ cm/s at RT), and N_t is the trap density in cm^{-3}. Degradation will be monitored by the evolution of the lasing threshold versus time. Taking into account the two dominant choices for recombination in the diagram above (2a and 2b), the threshold current of the laser is defined as:

$$I_{th} = \frac{qV}{\eta_i}(R_{sp}(N_{th}) + R_{nr}(N_{th})) \tag{4.5}$$

Where η_i is the injection efficiency, R_{sp} is the radiative spontaneous recombination rate, R_{NR} is the total non-radiative recombination rate, and N_{th} is the threshold carrier density. Here we make the approximation that the radiative and non-radiative current terms are "non-interacting". That is to say, as defects grow during the aging process the optical quality of quantum dots are unaffected, the total optical gain remains the same for the same amount of radiative current, and that increases in threshold are due

to increases in the non-radiative current term. We base this approximation on the fact that individual quantum dots are more or less non-interacting with neighboring dots or dislocations, carriers captured by a quantum dot become localized and can no longer diffuse toward a dislocation. Further, considering that the dot density is usually hundreds of times that of the defect density (5×10^{10} dots versus 10^8 dislocations per cm^2), this is not an unreasonable approximation at least for the early stages of degradation (see Figure 4.10).

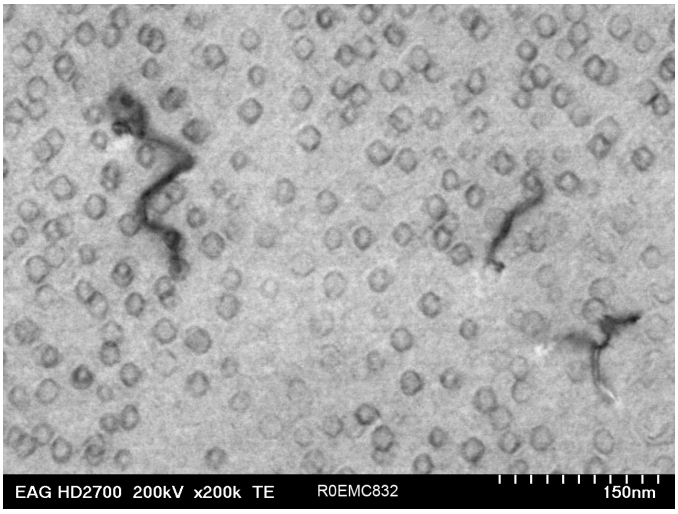

Figure 4.10: A typical plan-view TEM image of the quantum dot active region, illustrating that the surface coverage ratio of quantum dots is much greater than that of dislocations.

4.5.1 Numerical Algorithm

The above model can be used to generate a numerical algorithm to simulate the aging process. We begin by identifying the time dependence in the relevant equations that one may expect during aging. Here we assume that past lasing threshold the carrier density

in the active region is N_{th} which is the same for p and n:

$$R_{nr}(t) = \sigma v_{th} N_d(t) \frac{N_{th}^2(t) - n_i^2}{2N_{th}(t) + 2n_i \cosh \frac{(E_d - E_i)}{k_b T}} \tag{4.6}$$

$$R_{RE}(t) = \eta \frac{\exp[\Delta S/k]}{N_i} \exp[\frac{-(E_m - E_d)}{kt}] \left[\sigma v_{th} N_d(t) \frac{N_{th}^2(t) - n_i^2}{2N_{th}(t) + 2n_i \cosh \frac{(E_d - E_i)}{k_b T}} \right] \tag{4.7}$$

$$N_d(t) = N_d(0) + \int_0^T N_d(0) R_{RE}(t) dt \tag{4.8}$$

$$\tau_{nr}(t) = \frac{1}{\sigma v_{th} N_d(t)} \tag{4.9}$$

$$N_{th}(t) = N_r + R_{nr}(t) \times \tau(t) \tag{4.10}$$

Algorithm:

1. Set initial threshold carrier density $N_{th}(0)$ (assume p=n), initial defect density N_d, initial R_{nr}
2. Compute current non-radiative lifetime as $\tau_{nr} = \frac{1}{\sigma v_{th} N_d}$, and $\tau = \frac{\tau_r \tau_{nr}}{\tau_r + \tau_{nr}}$
3. Compute corresponding non-radiative carrier density N_{nr} as $N_{nr} = R_{nr}\tau$
4. Compute new threshold carrier density as $N_{th} = N_{th}(0) + N_{nr}$
5. Compute defect density growth from present R_{nr} as $N_d = N_d + R_{re}dt$
6. Compute new R_{nr} with new defect density and threshold carrier density
7. repeat 2-6

An attempt was made to evaluate the above algorithm to estimate the minimum acceptable defect level needed for lifetimes required of commercial applications. Unfortunately, it seemed that no matter what the initial parameters, the final threshold carrier density converged to a finite value proportional to the non-radiative recombination rate,

indicating a logical flaw with the physics assumed for the algorithm. Although this model is flawed, I included it here in the hopes that it will be taken up and improved by one more skilled in the arts of numerical modeling and laser reliability than myself. However we can speculate on the aging behavior from a qualitative standpoint. Examining (4.6)-(4.10), we see that they can be re-written as a set of coupled differential equations. The solutions, given the self-dependence on time, are most likely some form of exponentials. Thus, we expect that laser lifetimes should exhibit an exponential dependence on the defect density (or some equivalent combination of defect level and defect density. This has been observed experimentally, at least for GaN laser diodes [88].

The Shockley-Read-Hall analysis does not take into account kinetic or occupancy limitations (e.g. carrier diffusion, state of the trap level). However, some generic conclusions can be made. In general, defect density affects the lifetime much more than the trap level positioning, unless the traps are very shallow. Laser lifetimes are expected to show an exponential dependence on defect density. Future models should incorporate a better method to estimate the evolution of threshold versus time. Perhaps by estimating carrier leakage loss or cavity optical absorption loss versus defect density, from which a the threshold can then be estimated from an experimentally measured gain curve. Further, here we assumed an infinite source of point defects to fuel defect growth. This is not strictly true as degradation usually follows two stages, the first a rather"rapid" stage followed by decreasing rate of degradation where local point defect concentrations have been depleted and the reaction rate is thus reduced. This suggests that future models should also take into account the "atomic-hop-distance" accounted through inclusion of N_i in (4.2).

4.6 Miscellaneous considerations for reliability

There are many other important factors relevant to the lifetime of this system. These include the wavelength of the laser itself (which is related to the maximum energy released in a non-radiative recombination event), the effect of a non-pinned carrier density above threshold in a QD laser (resulting in increased carrier density for non-radiative recombination) [66], the uniformity of the QD ensemble, the position of the dangling bond levels within the bandgap [89], and residual tensile stress from the thermal expansion mismatch [10, 90]. Here we briefly discuss the implication of each in light of the proposed degradation model.

4.6.1 Impact of lasing wavelength

LED and laser lifetime is in many cases $\propto K/E_g$ or directly proportional to the wavelength [91, 92]. Absorption driven degradation processes will obviously depend on the energy of the photon absorbed, therefore it is reasonable to expect a similar dependence on the wavelength/bandgap energy for the lifetime.

4.6.2 Carrier dynamics

It is interesting to note that the best performing laser also has a p-doped active region. In a laser with an intrinsic active region, and assuming very low background doping levels, both electrons and holes are the minority carriers. The diffusion length of the minority carrier in the active region is related to both the carrier capture and recombination rate. In modulation doped active regions, the minority carrier becomes the opposite carrier type. In p-type modulation doped InAs quantum dot lasers, the electron capture rate has been measured by time-resolved photoluminescence to be nearly three times as fast as the undoped case [93]. P-doping also decreases the temperature sensitivity of the laser

threshold current, and has been postulated to result in a negative Auger coefficient with temperature, such that Auger recombination decreases with increasing temperature. At the moment we are seeing different degradation rates for our lasers with undoped active regions versus lasers with p-doped active regions. The p-doped laser shows significantly slower degradation rate than its undoped counterparts. However, a direct comparison is not possible because of the following reasons:

- The undoped lasers are aged on a carrier in an oven with single wirebonds to the n and p contacts, which significantly increased the series resistance (0.5 Ω) and device heating.
- The p-doped laser is aged at UCSB on a heater stage with multiple probes to its n-and p contacts, thus minimizing device heating compared to the wirebonded lasers.
- Although the p-doped laser is aged on a heater stage at nominally the same temperature as the ones at Aurrion in the oven rack, the ambient temperature can be cooler and thus the device may be not at the same temperature as those being aged at Aurrion.

However this is not to rule out that p-doped lasers may have better reliability than undoped lasers, since the minority carrier diffusion length may be three times less in the p-doped lasers. The carrier pinning (or non-pinning) past threshold may also be different between the two cases. Degradation depends on the square of the injected current as in buried heterostructure lasers [11]. Quantum dot lasers may have more injected current dependence on degradation because the fermi level is not pinned unlike other quantum well lasers [66].

If we instead dope the active region n-type instead of p-type, the minority carrier becomes holes. Holes are more massive than electrons and naturally have shorter diffusion

lengths. In addition, optical losses due to n-type doping is much less than p-type doping. Furthermore, it has been shown that n type GaAs is a harder material than undoped GaAs, and thus can slow the dislocation glide velocity (by a factor of 2) [11]. Perhaps it is possible to improve the reliability of InAs quantum dot lasers on Silicon using this doping scheme.

In essence, we'd like to ensure that most of the carriers injected into the active region are funneled into the quantum dots, that a strong confinement potential exists to localize exciton pairs long enough for them to recombine radiatively within the dot, and should any carriers escape out of the dot its mean diffusion length should be made to be less than the distance from the parent dot to the nearest dislocation but longer than the distance to the next nearest dot (and thus will be more likely to be captured by a different dot than a dislocation).

4.6.3 Effect of aging temperature

As was mentioned above, we were unable to study the activation energy for the thermal dependence of the degradation rate for our devices. In general, lasers tend to degrade faster at higher temperatures because carrier capture rate into a dislocation is limited by the thermal carrier velocity in the material bulk. Dislocations are also more mobile at higher temperatures, resulting in easier glide or climb processes. Furthermore, threshold current density always increases at higher temperatures, thus it would be reasonable to assume that dislocated materials would degrade faster at higher temperatures [94]. However, it has been previously observed that in GRINSCH lasers where there is a built in field, degradation in the graded regions where there is a built in field may actually decrease at higher temperatures because the higher temperatures increases the probability of thermal escape of carriers out of the defect state, and subsequently being swept away

by the built in field before recombining non-radiatively [95].

4.6.4 Effect of residual stress

The thermal expansion mismatch results in formation of dislocations upon cool-down from growth temperature, as well as a residual biaxial tensile stress which enhances degradation rate. For reliable laser operation, the stress should not exceed 10^8 dyne cm^{-2} [96]. For GaAs films heterepitaxially grown on silicon, for any thickness above 100 nm, the film will have a net tensile strain upon cooling down from growth to room temperature due to the difference in thermal expansion coefficients with silicon [90]. The presence of this strain may serve to enhance dislocation glide velocity, often a function of strain:

$$v = v_0 \tau^m e^{-U_p/(kT)}$$

Where τ is the applied shear stress, and m is an exponent that is usually 1.4-2 [97].

4.6.5 Role of dangling bonds

There is an explicit dependence on the average defect level in the expression for the Shockley-Read-Hall recombination rate (4.4). Indeed, different rates of degradation have been correlated with the position of average dangling bond levels in different materials [89, 11, 98]. This is manifested in the different aging characteristics of GaAs lasers versus that of InP based lasers. GaAs based lasers are susceptible to recombination enhanced defect reactions, which drives dislocation climb and leads to rapid and/or catastrophic failures. InP based lasers, on the other hand, are not as susceptible to this mode of failure. This difference has been surmised to be due to the fact that dangling bond levels are shallow or outside of the bandgap in most InP and related compounds, whereas GaAs/AlGaAs defect levels are typically mid-gap. One may also observe that

Year	Description	Aging condition	J(0) (A/cm^2)	P(0) (mW)	Dislocation density (method used)	Longest time to failure*	Ref.
1987	GaAs/AlGaAs SQW	RT APC	–	2	$10^7 cm^{-2}$	$\leq$ 10s	[69]
1991	$In_{0.05}Ga_{0.95}As$/AlGaAs SQW	RT APC	∼2000	2	-	10 hours	[79]
2000	$In_{0.2}Ga_{0.8}As$ "quantum dot like" active region	RT APC	1320	0.5	-	80 hours**	[101]
2001	GaAs/AlGaAs SQW on epitaxial lateral overgrowth stripe	RT APC	810	1	$2 \times 10^6 cm^{-2}$ (etch pits)	200 hours	[70]
2003	GaAs/AlGaAs SQW on graded Ge_xSi_{1-x}/Si	RT ACC	270	< 1	$2 \times 10^6 cm^{-2}$ (PVTEM + etch pits)	4 hours**	[80]
2014	**InAs/GaAs QDs on Ge/Si**	**30°C ACC**	**2000**	**16.6**	**$2 \times 10^8 cm^{-2}$ (PVTEM)**	**4600 hours**	[23]
2016	InAs/GaAs QDs on Si	26°C ACC	131	7	$\sim 10^5 cm^{-2}$ (XTEM)	∼101000	[24]

Table 4.1: A summary of representative lifetime data for GaAs based lasers grown on silicon. *Time to failure is defined either by 2x increase in drive current in APC mode, 2x increase in threshold in ACC mode, or **actual catastrophic failures. The entry in bold is this work.

surface recombination velocities are an order of magnitude less in InP as compared to GaAs. We note that InP quantum well lasers grown on silicon have shown excellent aging characteristics [99, 100].

4.7 Summary

Table 4.1 summarizes some representative lifetime data that have been reported for GaAs based lasers grown on silicon to date. Compared to previous quantum well lasers, the best quantum dot lasers tested in this study have >23x longer lifetimes at harsher operating conditions, despite the very high dislocation densities present ($> 10^8$ cm^{-2}) within the laser material. This apparent improvement in lifetime over GaAs quantum well lasers on silicon cannot be ascribed to differences in material quality, as previous works have mostly reported lower dislocation densities than what is found here. A graphical form of the results tabulated here is shown in Figure 4.11.

We attribute the improvement in lifetime to the same principle that enables the operation of quantum dot lasers despite high defect/dislocation densities, namely that

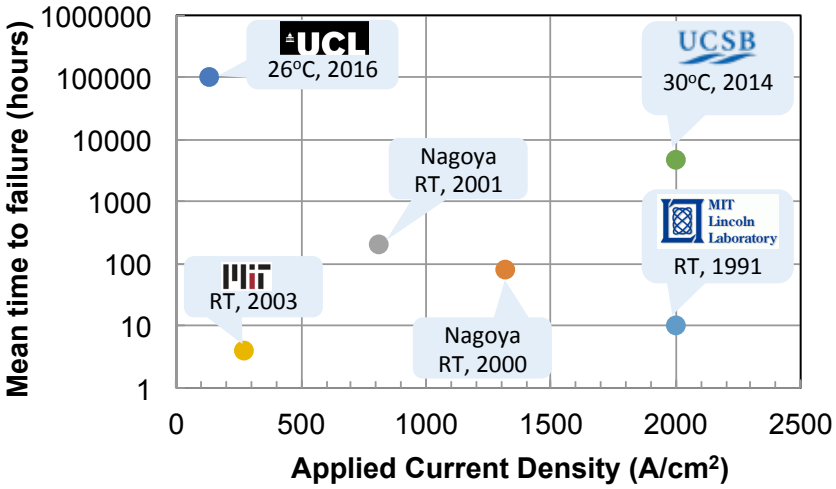

Figure 4.11: A summary of the data shown in Table 4.1, showing mean time to failure (MTTF) plotted against the applied current density used for the stress test. The results reported in this thesis represent the longest obtained lifetimes at the harshest testing conditions so far.

once carriers are captured by a quantum dot they become localized and can no longer diffuse laterally toward dislocations, unlike the quantum well case [16]. If the dot density far exceeds the dislocation density (in this case, >200:1 with a corresponding dot density of $\sim$ 4x10^{10} cm^{-2}), then the non-radiative capture cross section of individual dislocations or defects is effectively reduced due to competing radiative capture of the quantum dot ensemble. The net result is a reduction of the non-radiative recombination rate, which drives device degradation. Further, the strain field of the InAs quantum dots presents an additional mechanical barrier for the propagation of growing dislocation loops (a precipitation hardening effect), and some loops may become pinned by the dots [72].

Chapter 5

Quantum dot lasers on GaP/Si (001)

5.1 Introduction

In the previous sections we described 1.3 μm quantum dot lasers epitaxially grown on Ge/Si substrates with intentionally offcut silicon to suppress antiphase disorder arising from the III-V (polar) on silicon (non-polar) heteroepitaxy. To fully capture their added value, these lasers should be compatible with existing silicon CMOS foundry process flows to enable their integration with other photonic devices on a common silicon substrate. Deviation from the (001) axis would affect both carrier mobility in CMOS transistor channels as well as any processing steps that depend on the crystallographic orientation of silicon, such as KOH etching. Previous work on III-V lasers epitaxially grown on on-axis (001) silicon include continuous wave optically pumped 1.3 μm InAs quantum dot microdisk lasers on patterned (001) silicon [102], pulsed operation of optically pumped 1.3 μm InGaAs/InP distributed feedback lasers on patterned (001) silicon [103], and pulsed operation of electrically pumped 1 μm InGaAs/GaAs quantum well lasers on GaP/Si [81]. Continuous wave operation under electrical pumping has thus far not been demonstrated. In this section, we will demonstrate the first electrically pumped continuous wave III-V

quantum dot laser operating at room temperature and above epitaxially grown on on-axis GaP/silicon substrates without offcut or germanium buffers.

The epitaxial laser stack was grown on a GaP/Si (001) template provided by NAsP III-V GmbH. The original template was a 775 μm thick (001) on-axis p-doped Si substrate, with 200nm thick n-doped Si homo-epitaxial buffer and a subsequent 45 nm thick n-doped GaP nucleation layer, deposited by metal organic chemical vapor phase epitaxy. A 2.3 μm GaAs buffer layer was then grown on the GaP/Si template in solid source MBE, as previously reported in [81]. Following this, an InAs quantum dot laser embedded in a GaAs/AlGaAs graded index separate confinement heterostructure (GRINSCH) waveguide was re-grown on top of the GaAs buffer (see Figure 5.1). The active region consisted of seven stacks of InAs quantum dot layers embedded in 8nm $In_{0.15}Ga_{0.85}As$ quantum wells, which were separated by partially p modulation doped (pMD) GaAs barriers, following previously reported conditions [59]. The same laser structure was also grown on a GaAs substrate for comparison.

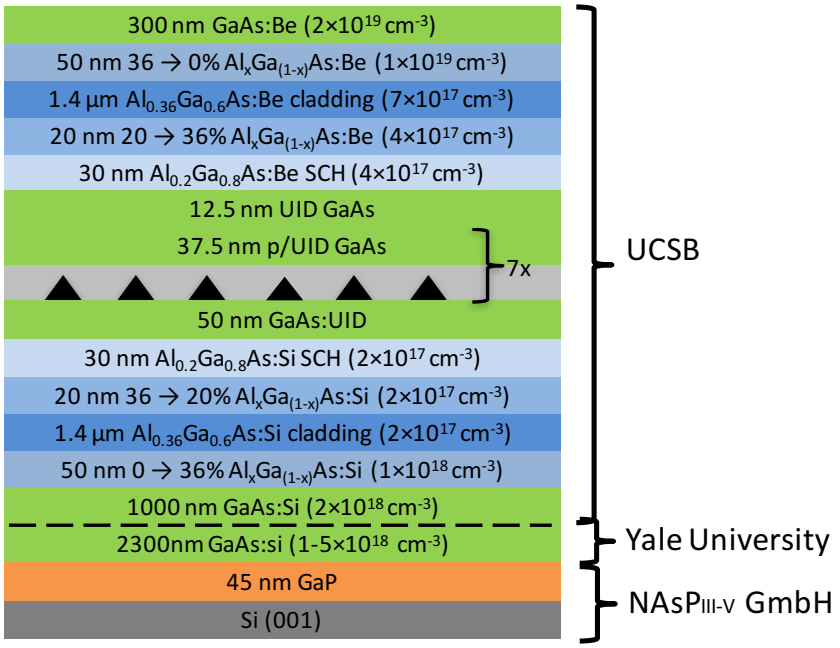

Figure 5.1: A schematic of the epitaxial stack.

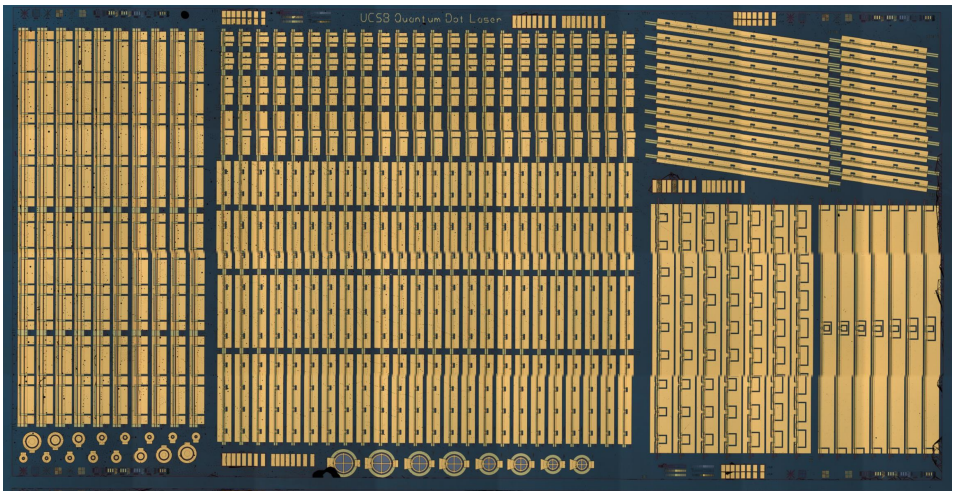

Figure 5.2: Stitched image of an entire fabricated die. The mask contains broad area lasers (left), different ridge laser designs (center), optical amplifiers (upper right), and mode-locked lasers (bottom right).

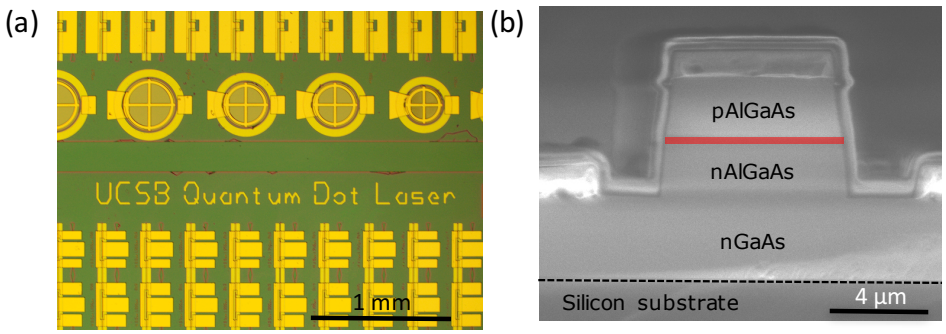

Figure 5.3: a): An optical micrograph of one section of the fabricated chip showing ridge lasers (top), electroluminescence windows, and short-cavity ridge lasers (bottom). b): A scanning electron microscope image of the cleaved cross section for a narrow ridge waveguide laser on GaP/silicon. The shaded red area indicates the approximate position of the active region.

The as grown material was then processed into deeply etched ridge waveguide lasers with varying stripe widths using standard dry etching and metallization techniques. The Ti/Pt/Au p-contact was deposited on top of the etched mesa and AuGe/Ni/Au n-contact metal deposited on the exposed nGaAs layers. An optical micrograph of a complete die is shown in Figure 5.2. Two types of laser geometries were fabricated: the first are broad area lasers 20 or 50 μm wide to ascertain material quality; the second are narrow

ridge waveguide lasers with smaller stripe widths between $2-10$ μm wide and cavity lengths between $750-1500$ μms long. Laser facets were formed by either cleaving or polishing. High reflection facet coatings were applied to the narrow ridge waveguide devices, with $\sim 95\%$ reflectors on the back facet and either $\sim 55\%$ (single DBR pair) or $\sim 80\%$ (double DBR pair) on the front. Optical and scanning electron microscope images of the fabricated devices are shown in Figure 5.3. Unless stated otherwise, all laser measurements presented in this section were conducted in continuous wave (CW) mode.

5.2 Experimental Methods

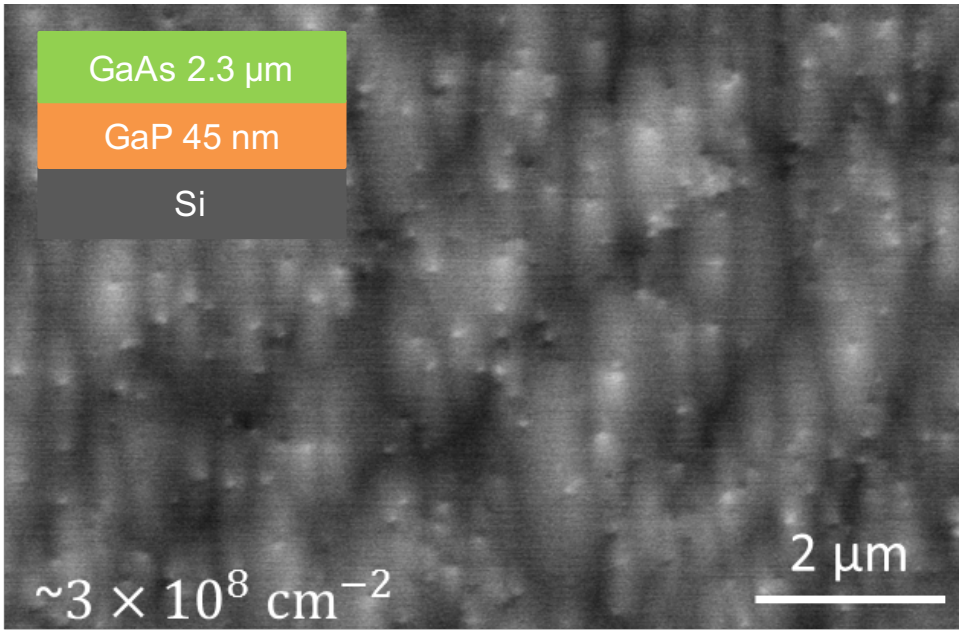

Figure 5.4: An electron channeling contrast image of the GaAs/GaP/Si template provided by Yale, showing a surface threading dislocation density of roughly $3\times10^{8}\text{cm}^{-2}$.

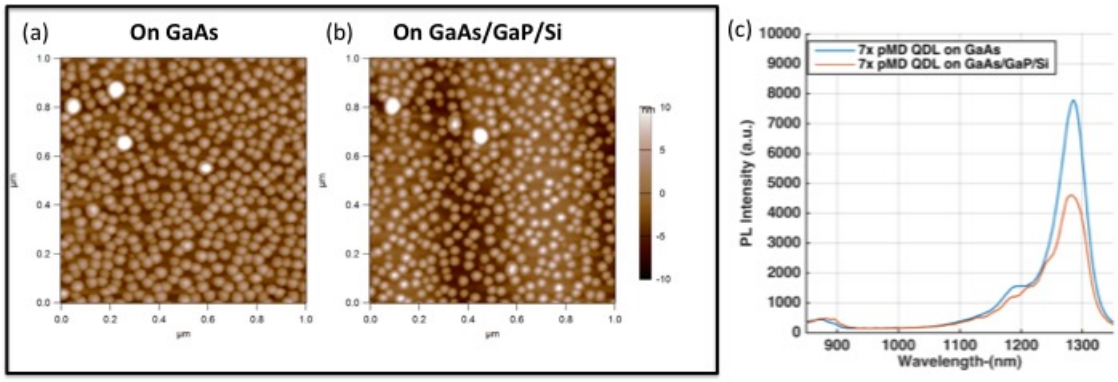

Figure 5.5: $1 \times 1\mu m^2$ AFM scans of InAs/GaAs quantum dots deposited on either a) native GaAs substrates, or b) GaP/Si templates. Qualitatively, the morphology of the quantum dots are similar across the two templates. c): Room temperature photoluminescence comparison of the as-grown laser stacks on GaP/Si to a reference laser grown on GaAs substrate under incident pump power density of 1.17 W/cm^2.

5.3 Results and Discussion

5.3.1 Material characterization

Prior to laser growth, the GaAs/GaP/Si buffer was characterized with electron channeling contrast imaging, which revealed a threading dislocation density of $\sim 3 \times 10^8$/cm^2, as shown in Figure 5.4. $1 \times 1\mu m^2$ AFM comparisons of InAs/GaAs quantum dots deposited on either native GaAs substrates or GaP/Si templates are shown in Figure 5.5. Qualitatively, the morphology of the quantum dots are similar across the two templates. A room temperature photoluminescence comparison of the as grown laser material on GaP/Si to the reference structure grown on GaAs under 1.17 W/cm^2 of excitation from a 785 nm pump laser is shown in Figure 5.5c. Both samples show a similar peak wavelength of 1280nm, while the laser on GaP/Si has a relative peak intensity of 57% compared to the reference sample on GaAs.

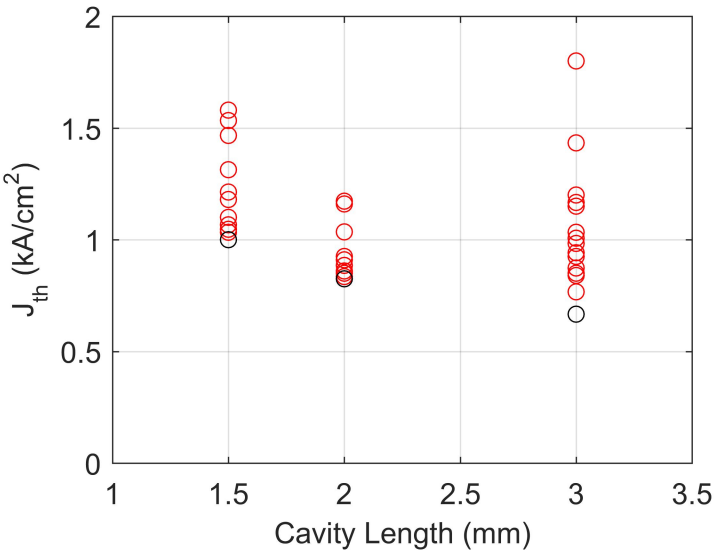

Figure 5.6: Room temperature continuous wave threshold current density (J_{th}) versus cavity length for 51 different broad area lasers (either 50 or 20 μm wide) on GaP/Si measured from the fabricated chip shown in Figure 5.2.

5.3.2 Broad area lasers

A plot of the threshold current density J_{th} versus cavity length for 51 broad area lasers on GaP/Si is shown in Figure 5.6. Although there is significant scatter, the lowest J_{th} value decreases with increasing cavity length, as expected. The lowest measured J_{th} is 667 A/cm^2. Figure 5.7 shows CW light-current (LI) and current-voltage (IV) comparisons of five broad area lasers on GaAs to five on GaP/Si, with the exact same cavity size (2 mm x 20 μm) and no extra high reflection coatings applied to the facets. The lowest threshold current (densities) of the aforementioned devices are 190 mA (475 A/cm^2) for lasers on GaAs, and 345 mA (862 A/cm^2) for GaP/Si. The corresponding differential quantum efficiencies of the aforementioned devices are 16.87% for the laser on GaAs and 8.80% for the one on GaP/Si. As shown in the same figure, single facet output powers up to 110 mW were obtained from the lasers on GaP/Si. We should also note that the lasers on GaP/Si had much lower voltages compared to their counterparts on GaAs. This is

surmised to be due to the higher doping levels used in the GaAs buffer for the devices on GaP/Si ($5 \times 10^{18}\text{cm}^{-3}$), whereas the devices on GaAs used the substrate as the n-contact which had doping levels of around $2 \times 10^{18}\text{cm}^{-3}$. The temperature dependent performance of one of the broad area lasers on GaP/Si is shown in Figure 5.8, showing lasing up to 55°C.

It is interesting to note that the relative percentage increase in threshold current density and decrease in differential quantum efficiency for devices on GaP/Si relative to devices on GaAs are roughly the same. The differential efficiency and threshold current densities are often expressed as:

$$\eta_d = \eta_i \left(\frac{\alpha_m}{\alpha_m + \alpha_i} \right)$$

$$J_{th} = \frac{J_{tr}}{\eta_i} e^{\left(\frac{\alpha_m + \alpha_i}{\Gamma g_{0J}} \right)}$$

where α_i is the cavity optical loss, $\alpha_m = \frac{1}{L} \ln \left(\frac{1}{R} \right)$ is the distributed mirror loss, η_i is the injection efficiency, J_{tr} is the transparency current density, and Γg_0 is an experimentally extracted gain coefficient for the material. We see that differences in either η_i or α_i would have a simultaneous impact on both differential quantum efficiency as well as the threshold current (density). To dissect the problem, we performed cut-back measurements of 20 μm wide broad area lasers of various cavity lengths for both devices grown on GaAs as well as on GaP/Si. As was done before in Chapter 3, we plot the inverse differential quantum efficiency versus cavity length and extract injection efficiency and modal gain parameters from the best fit line. The results are shown in Figure 5.9. As is visible there is significant scatter in the data. The argument can be made that the best possible data represents the true laser properties because the scatter is mostly due to extrinsic yield defects (from polishing, cleaving imperfections, oval defects, etc.), therefore the fit was

done using the best values of of inverse differential quantum efficiency from each cavity length.

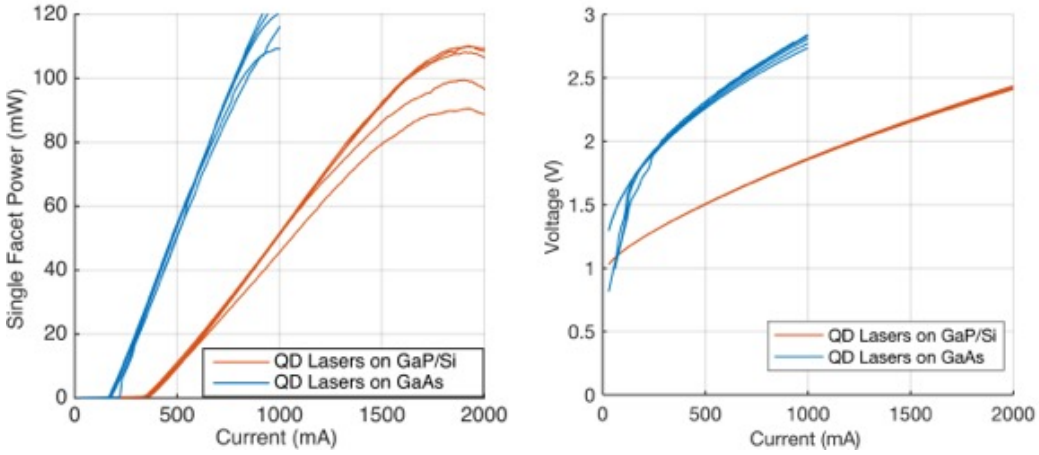

Figure 5.7: Room temperature light-versus-current comparisons of 2mm long by 20 μm wide broad area lasers without facet coating on GaAs (blue) and GaP/Si (red). Five devices of each type are shown. The lowest threshold current (densities) of the aforementioned devices is 190 mA (475 A/cm^2) for lasers on GaAs, and 345 mA (862 A/cm^2) for GaP/Si, with corresponding differential quantum efficiencies of 16.87% and 8.80%.

The extracted values of η_i, α_i, J_{tr} and Γg_{0J} are displayed in Table 5.1. We can see that the ratio of the injection efficiency values between lasers on GaAs to those on GaP/Si is very nearly the same as the observed difference in threshold and slope efficiency. Therefore we can attribute the bulk of the difference in performance to the difference in injection efficiency, which is presumably lower for the lasers on GaP/Si due to the presence of extended defects, which are encountered by carriers during transport from the contact to the active region. The threshold modal gain versus current density curves are plotted in Figure 5.10. After taking into account the discrepancy in injection efficiency, the two curves still do not exactly overlap. If we make the argument that the intrinsic material gain should not vary with the choice of substrate, then the difference would have to come from the confinement factor Γ, which is proportional to the size and density of the dots. Noting that the emission wavelength (and therefore dot size) is

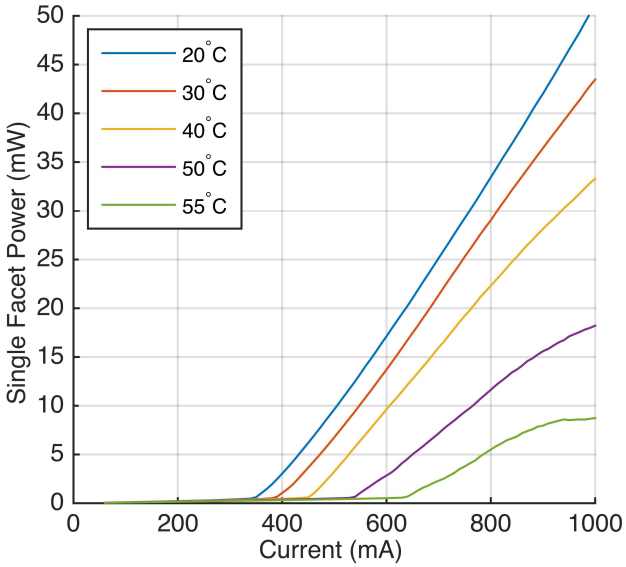

Figure 5.8: Continuous-wave lasing up to 55°C for a 2mm long by 20 μm wide broad area laser on GaP/Si (also shown in Figure 5.7).

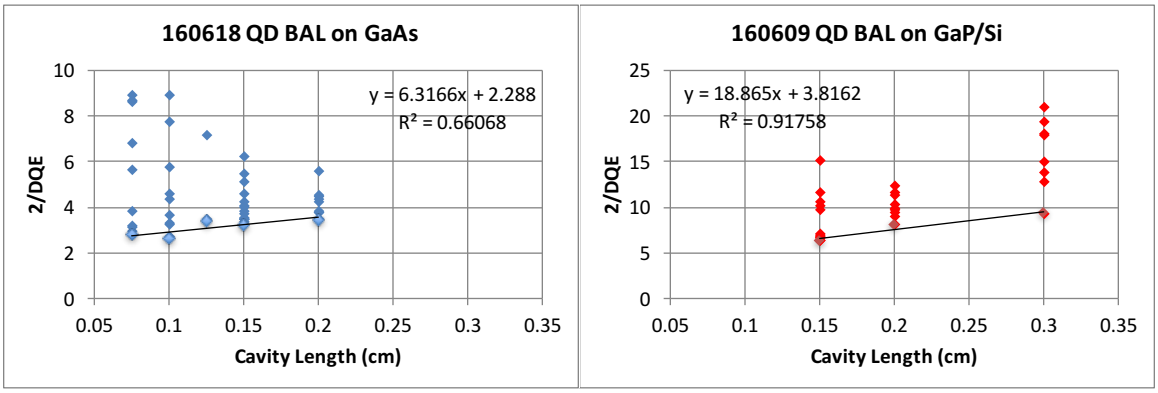

Figure 5.9: Inverse (single side) differential efficiency plotted versus cavity length for 20μm wide broad area laserse on either GaAs or GaP/Si.

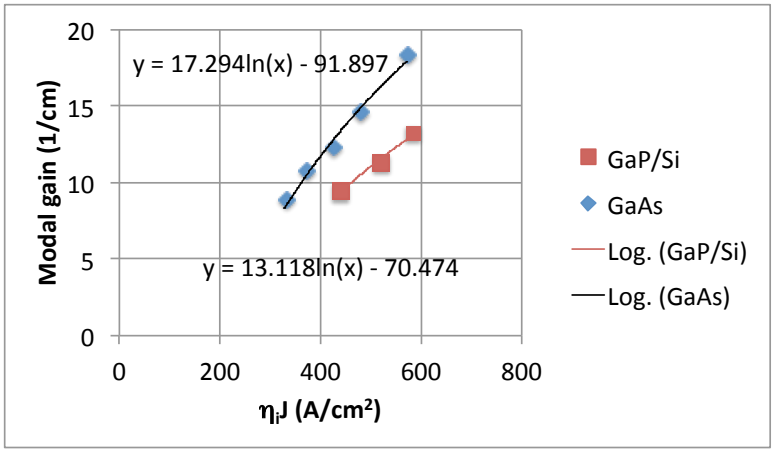

Figure 5.10: Threshold modal gain versus the fraction of injected current reaching the active region $\eta_i J$. The curves are fitted with a logarithmic fit to extract the gain coefficient Γg_{0J} and transparency current density J_{tr}: $\Gamma g = \Gamma g_{0J} \ln(J/J_{tr})$.

the same for the devices on the two substrates, we may then infer that any difference in Γ would come from a difference in dot density. Referring back to the AFMs shown in Figure 5.5, it was determined that the density of dots on silicon is slight less than those on GaAs (4.36 versus 4.66×10^10 cm^{-2}, respectively). This would account for roughly 6% of the 24% difference in the relative Γg_{0J} values. We attribute the remaining uncertain to fitting and experimental error. As is visible from Figure 5.9, the scatter in the data points is very large and inclusion or exclusion of certain points from the fitting would change the extracted values significantly. For example, in the case of the GaAs devices, the 750 and 1250 μm values were re-cleaved from material that was near the edge of the fabricated chip, and clearly do not fit with the rest of the data points. If we removed those from the plot, then the fit would yield an injection efficiency of 1.07, a cavity loss α_i of 5.07 cm^{-1}, and a modal gain curve that would almost exactly overlap with the GaP/Si devices. However we have included these data points for completeness, and also because an injection efficiency greater than unity is unphysical.

	GaAs	GaP/Si
η_i	0.87	0.52
α_i (cm^{-1})	3.16	5.63
J_{tr} (A/cm^2) per layer	29.01	30.76
Γg_{0J} (cm^{-1}) per layer	2.47	1.87

Table 5.1: Gain and loss values extracted from cutback mesurements shown in Figure 5.9 and Figure 5.10 for seven layer p-doped InAs/GaAs quantum dots lasers grown on either GaAs or GaP/Si substrates.

5.3.3 Ridge lasers

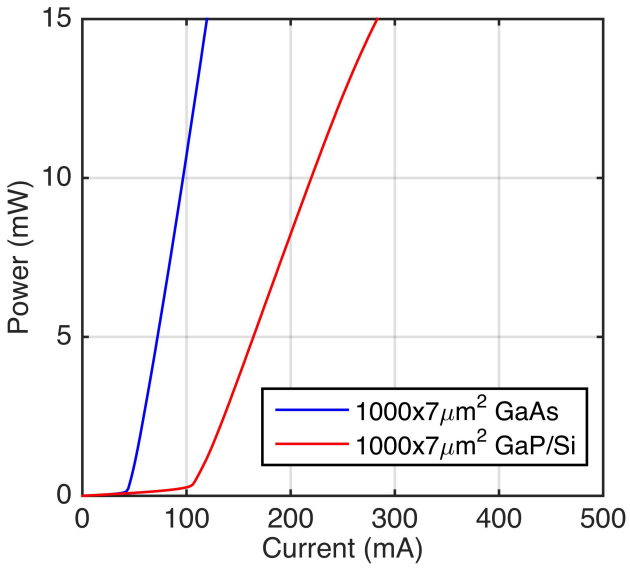

Figure 5.11: Room temperature continuous wave light-versus-current comparisons of 1 mm long by 7 μm wide ridge lasers on GaAs (I_{th}=44 mA) and on GaP/Si (I_{th}=105 mA), both with as-cleaved facets.

Figure 5.11 shows room temperature CW LI comparisons of 1 mm long by 7 μm wide ridge lasers on GaAs (I_{th}=44 mA) and on GaP/Si (I_{th}=105 mA), both with as-cleaved facets. Once again, the threshold current roughly a factor of two higher for the laser on GaP/Si. A separate batch of ridge lasers were made by facet polishing followed by high-reflection coating of the facets. Figure 5.12 shows room temperature light-current-

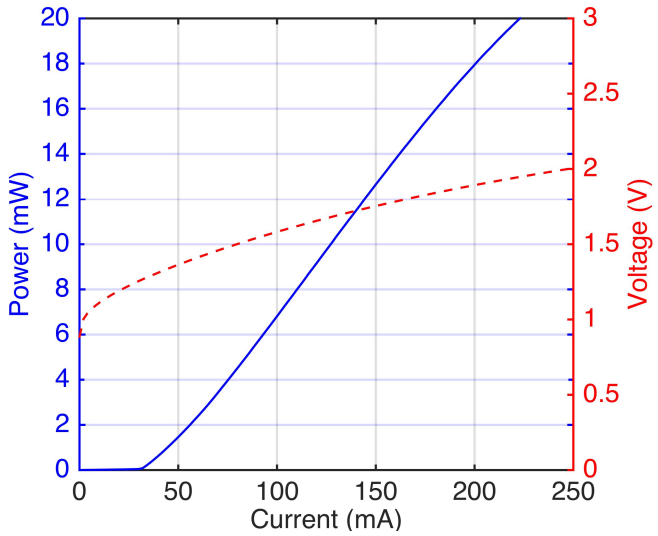

Figure 5.12: Room temperature continuous wave light-current-voltage curve for an HR/HR coated (95/55%) 750×4 μm^2 laser with a threshold of 32 mA.

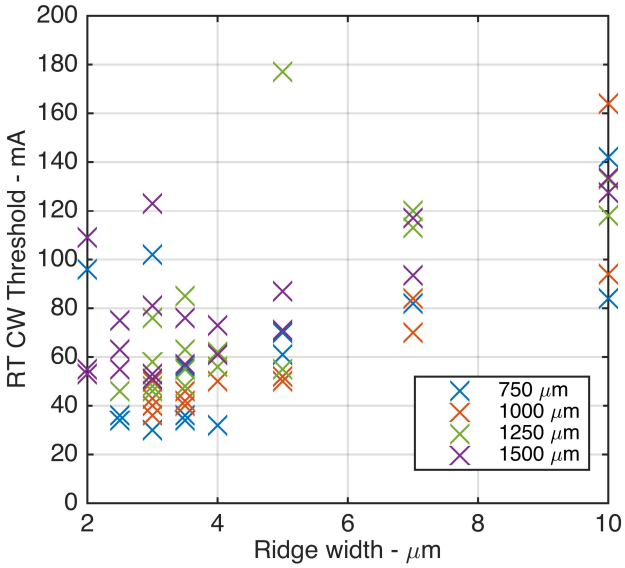

Figure 5.13: Room temperature continuous wave threshold currents for 68 different HR/HR coated (95/55%) ridge waveguide lasers of various cavity sizes.

voltage (LIV) measurements of a 750x4 μm^2 device with a 32 mA threshold and slope efficiency of 0.106 W/A. A plot of the threshold current versus ridge width for 68 different measured lasers with cavity lengths ranging from 750 to 1500 μm is shown in Figure 5.13. The threshold decreases as expected for smaller cavities, with the lowest threshold being 30 mA. We hypothesize that the statistical scatter is mostly due to chipping of facet material from the high aspect ratio waveguides during the polishing process, as confirmed by visual inspection. Figure 5.14 shows a typical room temperature lasing spectrum for a laser on GaP/Si. The lasing wavelength of 1280nm matches closely with the measured photoluminescence peak.

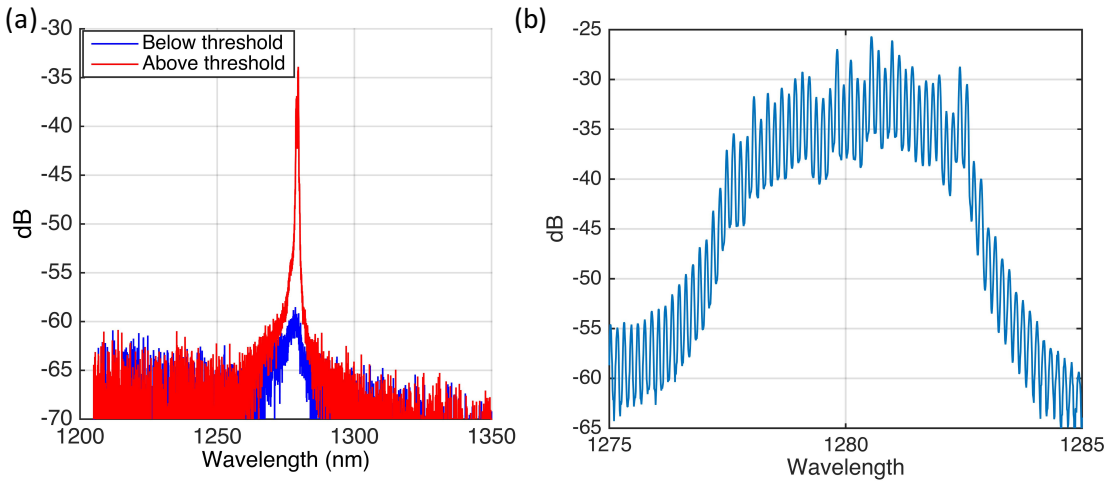

Figure 5.14: a) Coarse electroluminescence spectra below and above threshold at room temperature showing ground state lasing at 1280 nm. b) High resolution scan of the above threshold lasing spectrum showing the many Fabry-Perot longitudinal modes centered around 1280 nm.

Figure 5.15 demonstrates high temperature continuous wave operation of a longer device (1500x3.5 μm^2) up to 90°C. There is a discontinuously large increase in threshold between 80 − 90°C, which we think is due to the saturated ground state gain being unable to compensate for the cavity loss, resulting in lasing from the excited state. A plot of the CW threshold current versus stage temperature for the devices in 5.15 along with several other measured lasers is shown in Figure 5.16. The average characteristic temperature T_0

is ∼100K between $20-40$°C, and ∼40K between $40-80$°C. This behavior is roughly in line with what we have previously observed for similar lasers grown on Ge/Si substrates [14, 59].

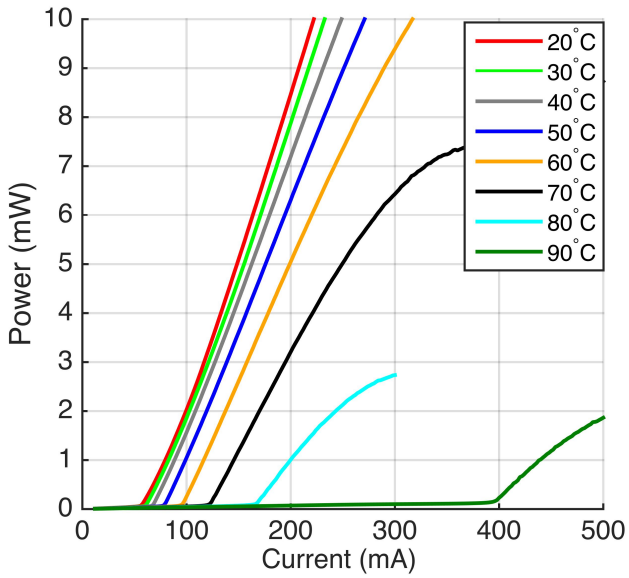

Figure 5.15: A $1500\times3.5\mu m^2$ device lasing in continuous wave mode up to 90°C.

We note that the sidewalls for the deeply etched mesa stripes defining the laser cavity showed significant roughness from the fabrication process (Figure 5.17). While not a serious issue for the broad area devices with wide stripe widths, the roughness likely limited the performance of the narrow ridge waveguide lasers where the mode sees a higher overlap with the sidewalls, resulting in increased sidewall scattering loss (and sidewall recombination current). We therefore expect further improvements in device performance from optimized processing.

5.4 Summary

The first electrically pumped continuous wave III-V quantum dot lasers epitaxially grown on on-axis (001) silicon without offcut or germanium layers have been presented.

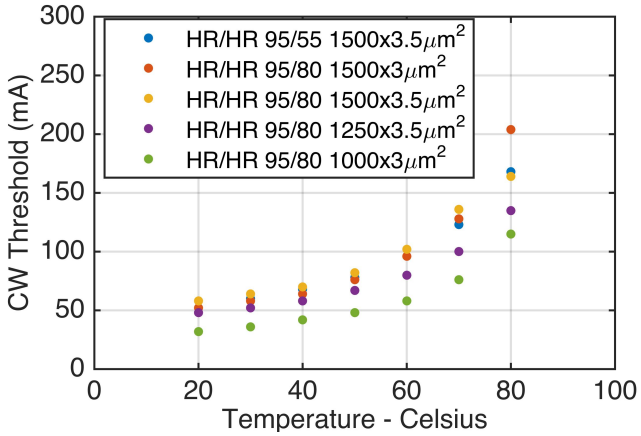

Figure 5.16: A plot of threshold current versus stage temperature for various different laser cavities. The average characteristic temperature T_0 is ∼100K between $20-40°$C, and ∼ 40K between $40-80°$C

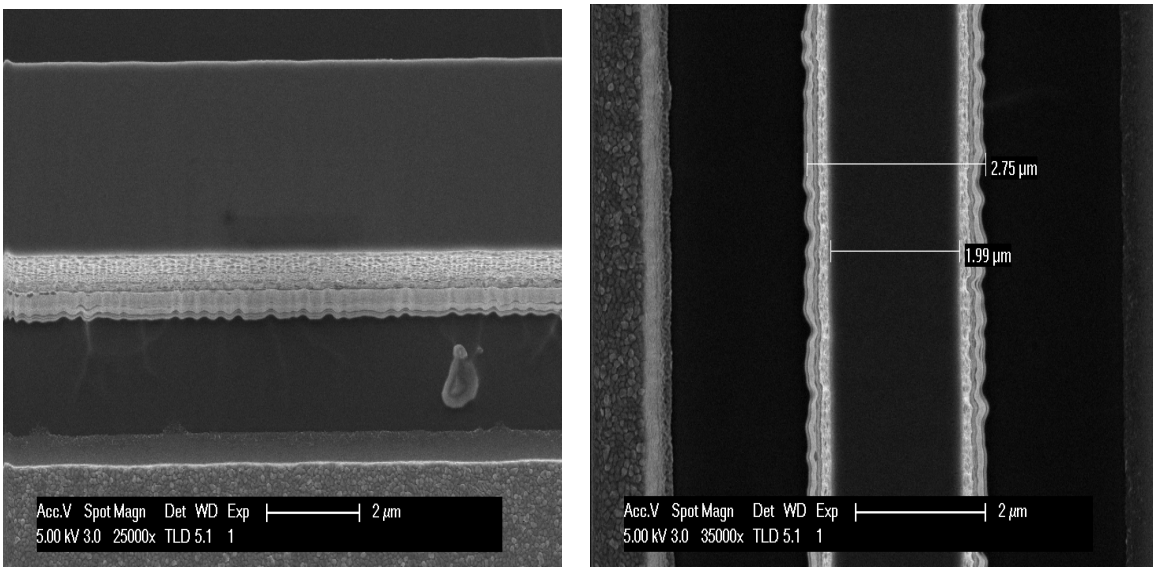

Figure 5.17: SEM images showing the sidewall roughness, which possibly developed during a n-metal rework.

Narrow ridge waveguide lasers show thresholds down to 30 mA and lasing to 90°C, while broad area lasers with threshold current densities of 862 A/cm^2 and output powers up to 110 mW have been demonstrated. This work demonstrates the compatibility of high performance monolithic III-V light sources with on-axis silicon substrates, and the their potential for foundry integration. A comparison of broad area laser characteristics between devices grown on GaAs to those grown on GaP/Si suggests that the majority of the degradation in performance for devices on GaP/Si is from the lower injection efficiency. This also suggests that future research should focus on methods to improve the injection efficiency for lasers epitaxially grown on silicon.

Chapter 6

Sensitivity to optical feedback

6.1 Introduction

In the previous sections we have demonstrated various kinds of quantum dot lasers epitaxially grown on silicon, to be used as an integrated light source in a silicon photonic integrated circuit. As an integrated component of a photonic integrated circuit and/or optical system, unintentional reflections from various possible interfaces such as active/passive transitions, waveguide crossings, regrowth interfaces, process imperfections, etc. can produce unwanted feedback to the laser. The behavior of quantum well lasers under optical feedback has been studied extensively, with a well known diagram classifying laser response under five distinct regimes of different feedback strengths and phases [104]. Outside of very narrow regimes where feedback is beneficial for inducing linewidth narrowing, the majority of feedback levels causes deleterious effects such as linewidth broadening, mode hopping, and/or increased amplitude noise [104, 105]. For data communication systems this would be undesirable as the increase in laser amplitude or phase noise would degrade the bit error rate. Lasers integrated with a silicon photonic chip are particularly susceptible to these effects, as the low loss waveguides and high in-

dex contrast inherent to the platform are particularly conducive to the creation of strong unintentional feedback. Isolators are typically used to limit unwanted feedback to the laser, and silicon based on-chip isolators have been recently demonstrated with maximum isolation ratios up to 32 dB [106]. However, the integration of an isolator increases cost, process complexity, chip area, and adds additional loss. Alternatively, the laser itself can be engineered to be more stable under feedback, eliminating the need for an integrated isolator altogether or at least relaxing the performance requirements for the isolator.

A common analytical expression for predicting the critical feedback level where the laser enters a coherence collapse regime is derived in [107]:

$$f_{crit} = \frac{\tau_L^2 (K f_r^2 + \gamma_0)^2}{16|C_e|^2} \left(\frac{1+\alpha^2}{\alpha^4} \right) \tag{6.1}$$

where τ_L is the roundtrip delay within the gain cavity, α the linewidth enhancement factor, $|C_e| = \frac{1-R}{2\sqrt{R}}$ the coupling strength from the laser cavity to the external cavity, $\gamma = (K f_r^2 + \gamma_0)$ is the damping rate of the relaxation oscillations with f_r being the resonance frequency, K the K-factor, and γ_0 is the damping factor offset. Feedback is defined as the ratio of the reflected power over the emitted power. This expression is derived assuming weak feedback and a long external cavity delay (such that the delay time $>> 1/f_r$, and is derived for the minimum linewidth external cavity mode. Although this expression calculates a feedback threshold above which the laser is stable, the absolute value of this threshold will obviously vary depending on measurement conditions and laser design, and thus this expression is better used as a qualitative guide for the relative feedback tolerance of a laser. The major dependencies in feedback sensitivity in (6.1) are as follows:

- the internal laser cavity roundtrip time τ_L

- the linewidth enhancement factor α
- the damping rate of the relaxation oscillation frequency $\Gamma_{RO} = Kf_r^2 + \gamma_0$ defined by the K-factor of the laser, the relaxation oscillation frequency f_r, an the offset damping frequency γ_0
- and the coupling efficiency back to the laser $C_e^2 = \frac{1-R}{2\sqrt{R}}$, where R is the facet reflectivity

Therefore, feedback tolerance increases for:

- longer cavity lengths
- higher facet reflectivities or cavity Q's
- higher driving currents/output powers (via increase in f_r), but not necessarily true for quantum dot lasers as will be detailed below
- higher K factors
- smaller α

6.2 Advantage of quantum dot lasers for feedback tolerance

Referring back to the expression in (6.1), two factors intrinsic to quantum dots should give them an advantage in feedback sensitivity. The first is the approximate inverse square dependence on the linewidth enhancement factor α, and the second is the dependence on the relaxation oscillation damping rate. It is well known that quantum dot lasers have much lower direct modulation bandwidths compared to quantum wells, typically

limited to 10-15 GHz for the 1.3 μm InAs/GaAs quantum dot system [108]. The primary reason for this is strong gain compression and low saturated gain in quantum dot active regions. Nonlinear gain compression is estimated to be 10 times higher in quantum dots than in quantum well lasers, and has been postulated to be due to unequal carrier scattering/capture rates of electrons and holes within quantum dot lasers [109]. This results in higher K-factors for quantum dot lasers compared to quantum wells, and therefore strong damping of the relaxation oscillation and limited small-signal bandwidths. An analytical expression for K factor was given in [108]:

$$K = \frac{4\pi^2}{\nu_{gr}} \left[\frac{1}{\alpha} + \frac{\epsilon}{a_{max}\left(1 - \frac{\alpha}{G_{sat}}\right)} \right] \tag{6.2}$$

where a_{max} is the largest value of differential gain, ϵ is the coefficient of nonlinear gain saturation, G_{sat} maximum saturated gain of the ground state, and v_{gr} is the group velocity. Efforts to increase the small signal modulation bandwidth have primarily been concentrated on increasing the maximum saturated ground state gain. However the high K-factor and damping of the relaxation does lend itself to a predicted lower sensitivity to reflections, as seen in the expression in (6.1). The predicted lower amplitude-phase coupling (α) factors of quantum dots relative to quantum wells [110, 111, 108, 112] would also lend itself to higher feedback tolerance, although this parameter is rather difficult to quantify and the same formalism used to define it for quantum wells may not apply to quantum dots [110, 113]. For a detailed dissection of feedback dynamics in quantum dot lasers the reader is referred to Christian Otto's excellent thesis [112].

A numerical evaluation of (6.1) is shown in Figure 6.1 for two different values of the K factor characteristic of either quantum dot lasers (K=1 ns) [108] or quantum well lasers (K=0.265 ns) [25], with everything else kept the same. As can be seen, the difference in the K factor alone is predicted to result in a 10 dB increase in f_{crit} for quantum dot

lasers relative to quantum wells, with any differences due to the α factor between dots and wells resulting in even larger increases to the critical feedback level for coherence collapse. Furthermore, the peak relative intensity noise (RIN) of semiconductor lasers under optical feedback is capped by the inverse of the damping rate of relaxation oscillations: $\text{RIN}_{peak} = \frac{1}{\gamma}$ [114]. Thus, feedback induced noise is expected to be highly suppressed in quantum dot lasers as well. In this work, we experimentally quantify these predictions for quantum dot lasers epitaxially grown on silicon by measuring their relative intensity noise (RIN) under different levels of feedback and comparing with heterogeneously integrated quantum well lasers on silicon.

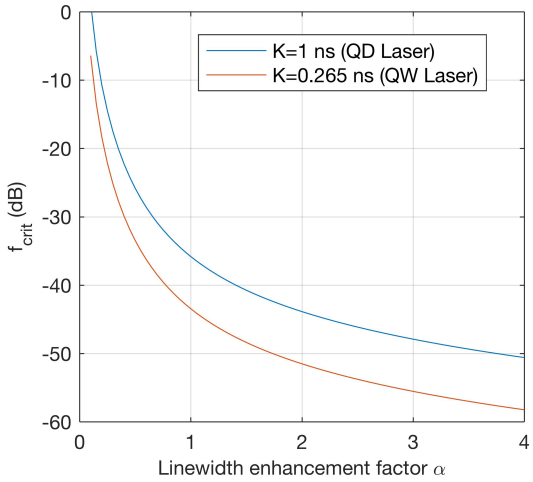

Figure 6.1: A numerical evaluation of (6.1) for two different values of the K factor characteristic of either quantum dot lasers (K=1 ns) [108] or quantum well lasers (K=0.265 ns) [25], with everything else kept the same (τ_L=4 ps, f_r=3 GHz, γ_0=0.65 GHz, R=0.3. The different K factors leads to a ∼10dB improvement in reflection sensitivity for quantum dot lasers, with additional improvements possible depending on the difference in α.

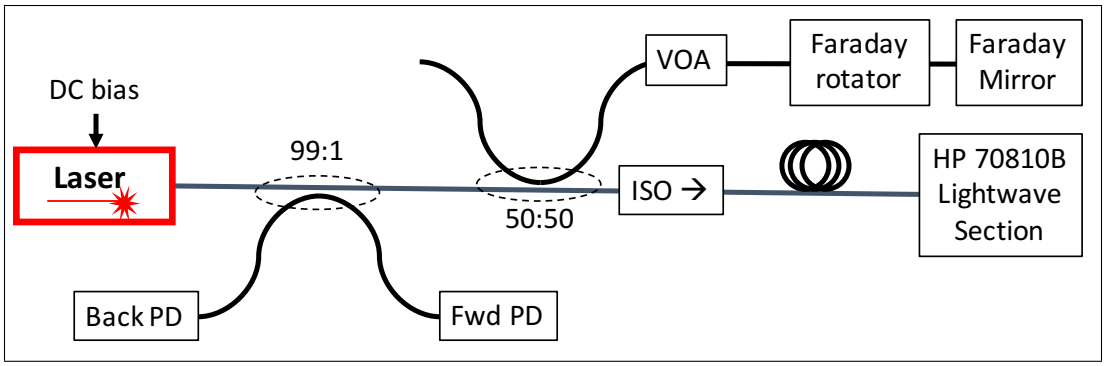

Figure 6.2: A schematic of the measurement setup used in this study.

6.3 Experimental methods

6.3.1 Measurement setup

The measurement setup used is shown in Figure 6.2. Light from the device under test (DUT) is first coupled to a lensed fiber and split by a 50:50 directional fiber coupler. The power in one arm is fed into a spectrum analyzer to monitor the relative intensity noise, and an optical isolator with 60 dB of isolation ratio isolates the DUT from uncontrolled reflections. Power in the other arm is reflected back to the DUT with a Faraday mirror, which along with an in-line Faraday rotator shifts the polarization of the reflected light by 180 degrees. This ensures that any changes to the original polarization state of the output light caused by fiber birefringence will be undone on the return trip, ensuring that the polarization of the feedback is nearly the same as the original output. The amplitude of the feedback is controlled with an in-line variable optical attenuator. A 1% fiber coupler tap right after the lensed fiber monitors the power levels in the forward and backward directions, and the feedback level is defined as the ratio of the backward to forward powers. The fiber couplers were dual-band couplers for operation at 1550 and 1310nm, while the other wavelength sensitive components (isolator, Faraday rotator, and Faraday mirror) were swapped out as needed for the wavelength of the DUT. With

the exception of the spectrum analyzer interface, all the fiber connections had angled connectors. The external cavity round trip path length is roughly 13 meters for the quantum well devices, and 15 meters for the quantum dot lasers, due to different fiber pigtail lengths of the components used. For this study, we examined the relative intensity noise (RIN) spectrum from 100 MHz to 10 GHz. This range of frequencies was chosen to be within the highest sensitivity range of the spectrum analyzer. Resolution bandwidth was 3 MHz for all measurements, with a video bandwidth of 100 kHz.

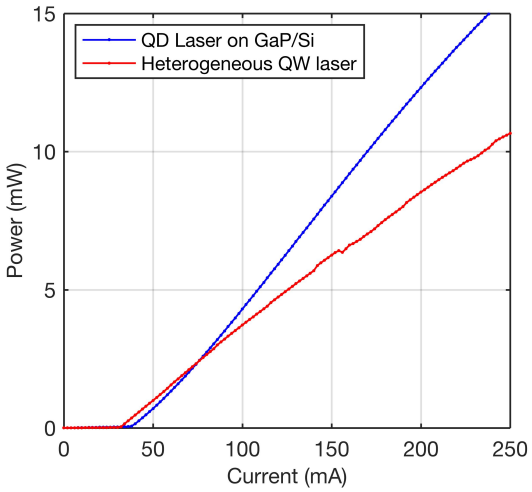

Figure 6.3: Typical light-current characteristics of the quantum dot lasers on GaP/Si and heterogeneously integrated quantum well lasers in this study.

6.3.2 Devices studied

To make the comparison as fair as possible, the quantum dot and quantum well devices used in this study were down-selected from available devices in our lab with the criteria that they both be of similar type (in this case Fabry-Perot), have similar cavity lengths (due to the implicit dependence of f_{crit} in (6.1) on the length of the gain section through τ_L), and operating in or close to single transverse mode. The heterogeneously integrated quantum well lasers studied have 7 compressively strained InAlGaAs quantum

wells as the active region, lasing around 1580 nm at room temperature (RT). These lasers are roughly 1560 μm in length with 1048μm long III-V gain sections (as measured from taper to taper) and the rest being purely passive silicon waveguide sections [115]. The III-V mesa widths are 26 μm wide with implant defined current channel width of 4 μm. The quantum dot lasers measured are deeply etched ridge waveguide lasers epitaxially grown on GaP/silicon substrates around 1 mm long in length and 3-3.5μm in width, with 7 layers of InAs/GaAs quantum dots as the active region, and lasing around 1280 nm at RT. The output facet for the quantum well lasers is an uncoated silicon waveguide facet with $\sim 30\%$ reflectivity, whereas for the quantum dot lasers it is a coated III-V facet with approximately $\sim 55\%$ reflectivity. Figure 6.3 shows typical measured light-versus-current plots for the two types of lasers. Because the external cavity delay time is much longer than the time scale of the relaxation oscillations ($L_{ext} > c/(2f_r)$), we expect the feedback behavior to be independent of the feedback phase, and the feedback is incoherent with the emitted radiation.

6.3.3 Short-term reliability of the GaP/Si QDLs

During the early trials of this experiment, it was quickly discovered that the data collection process was very time consuming, as will be detailed below. For each bias current of the laser, it can take up to 20 minutes to measure and collect the RIN data for the various feedback levels studied (approximately 20 different data points), even though the measurement has been automated to the maximum extent possible. To repeat the measurement for a single laser at 4-5 different bias points, and also allowing for down-time as well as time required for fiber alignment, means that full characterization of a single laser can take up to a few hours. One must consider the fact that the laser is under CW bias this entire time. In light of the reliability study conducted in Chapter 4, a quick stress

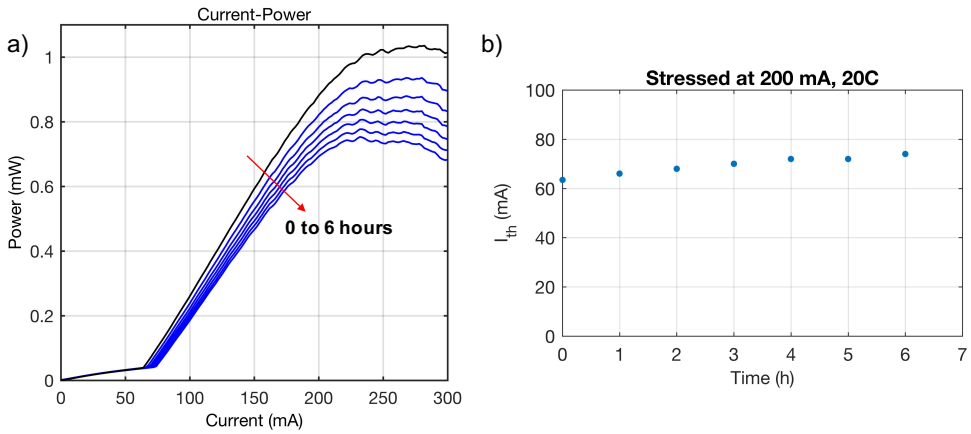

Figure 6.4: a) LI curve of a $1250\times2\mu m^2$ laser with 95/80% HR coatings, stressed at 200 mA (8 kA/cm^2) and at 20C. The black curve is the LI curve taken before the stress test. b) Threshold of the device in a) plotted as a function of aging time in hours.

test was conducted at UCSB to check that the devices are not rapidly degrading during the course of the measurement. For the study we chose a fairly small laser and biased at around the maximum current to be applied to the devices in this study ($\sim$ 200mA) to simulate the worst case scenario in terms of possible degradation over the course of the measurement. The stage temperature was held at 20C, and the corresponding applied current density is 8 kA/cm^2. Note that this is more than three times higher than the maximum applied current density for the devices studied in Chapter 4. The results of the study are shown in Figure 6.4. We do observe some degradation in the six hours that the device was stressed at, but determined that this rate of degradation was acceptable for the purposes of this measurement since the stress-test was created to simulate harsher conditions than would be encountered by devices used in this measurement (namely, smaller average applied current densities over the course of the measurement as well as shorter testing times).

6.3.4 Relative Intensity Noise measurements

Relative Intensity Noise (RIN) was measured using a HP70810B lightwave signal analyzer that can automatically correct for thermal and shot noise. Light from the laser is collected by a built-in InGaAs photo-diode (bandwidth between 1200-1600 nm), with the DC component of the photo-current used to calculate the average received optical power. The AC component of the photocurrent is amplified and beat with a local oscillator to determine the noise spectrum, from which the relative intensity noise is calculated after dividing by the average received optical power squared. This initial measured noise is the total noise present in the system and will be termed "System RIN". This measured quantity contains contributions from the laser, thermal noise from the built-in electronics, as well as the shot noise:

$$RIN_{system} = RIN_{laser} + RIN_{thermal} + RIN_{shot} \tag{6.3}$$

$$RIN_{system} = RIN_{laser} + \frac{N_{th}}{R_L(rP_{AVG(opt)})^2} + \frac{2q}{rP_{AVG(opt)}} \tag{6.4}$$

In (6.4), N_{th} is the spectral density of the thermal noise from the electronics (amplifier after the photodiode), R_L is the load resistance of the amplifier input, r is the responsivity of the photodiode, and $P_{AVG(opt)}$ is the average received optical power. After the first measurement of the system RIN, the laser input port is blanked off and the system then takes a "dark" measurement, from which it calibrates for the thermal noise due to the electronics. The shot noise can be calculated from the received optical power or the DC component of the photocurrent. The laser RIN can then be calculated by subtracting the thermal and shot noise contributions from the measured system RIN. Because both α and f_r have a dependance on the applied current density, we study the effect of feedback on the RIN at several different bias points above threshold. In particular, the α factor

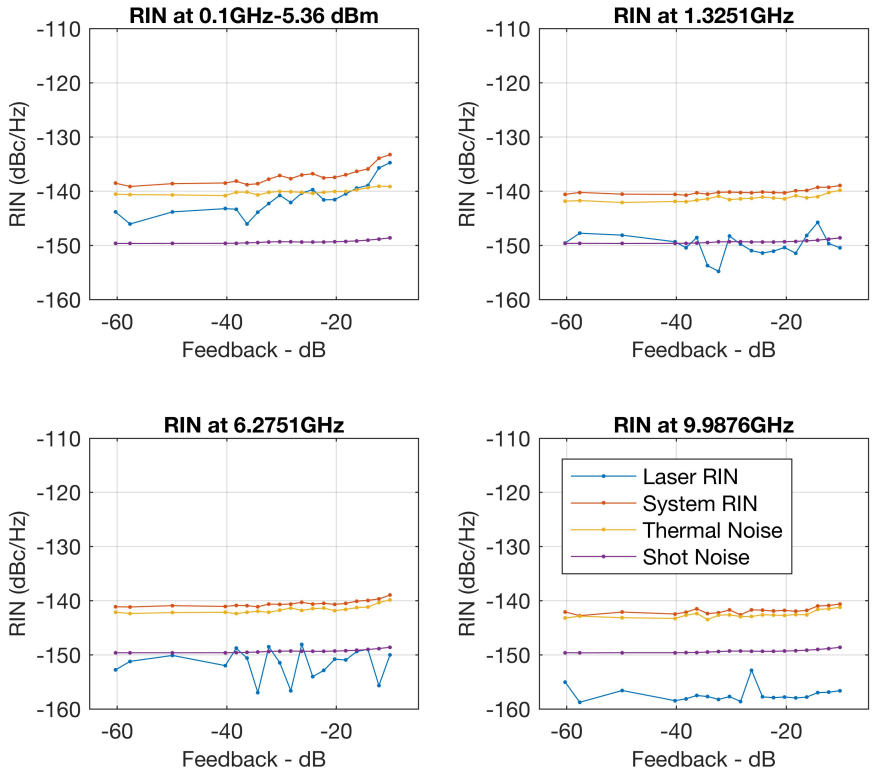

Figure 6.5: The various components of RIN versus feedback for a 1 mm×3 μm quantum dot laser on GaP/Si, measured at 2×I_{th} and at four different sampling frequencies.

of quantum dot lasers tend to have a strong dependance on current due to saturation effects [116, 110], and we provide evidence for this later.

To check that the spectrum analyzer was working correctly, we first used it to measure the RIN from the amplified spontaneous emission of an erbium doped fiber amplifier (EDFA). An unseeded EDFA can be approximated as a pseudo-thermal source whose power spectral density is roughly inversely proportional to the gain bandwidth, giving typical RIN values of around -124 dBc/Hz for common bandwidths of 2.5 THz [117]. Using our spectrum analyzer we measured relatively flat RIN values around ∼-122 and ∼-123 dBc/Hz for 40 and 80 mW of output power, respectively. This confirms that our measured RIN values are reasonably accurate.

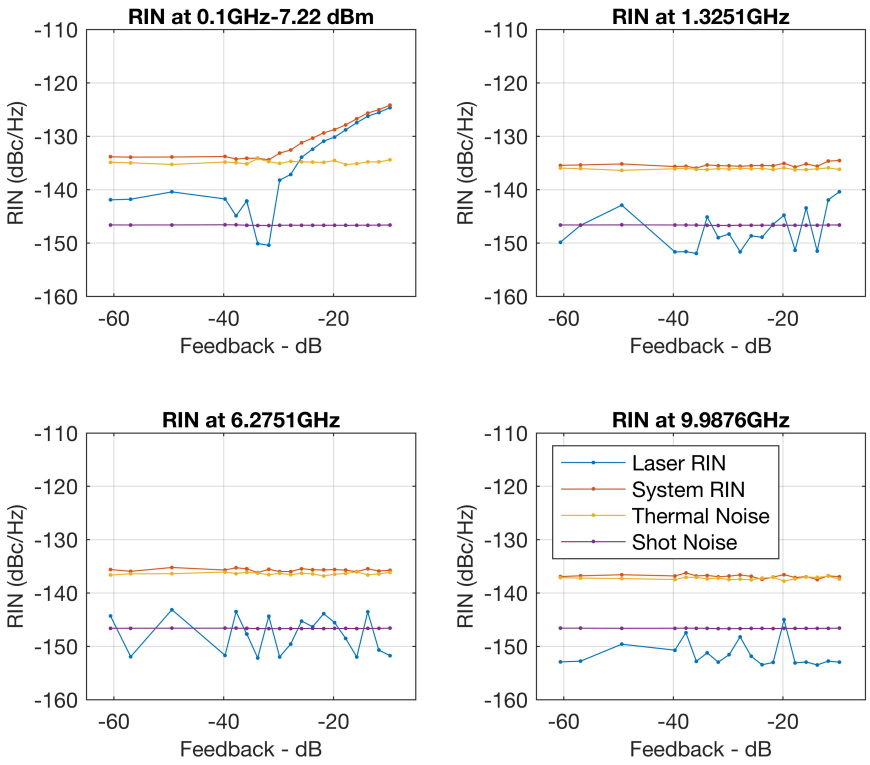

Figure 6.6: The various components of RIN versus feedback for a heterogeneously integrated quantum well laser on silicon, measured at $2\times I_{th}$ and at four different sampling frequencies.

Unfortunately due to the archaic nature of the HP70810B lightwave signal analyzer, there is no efficient way to download the calculated laser RIN data without the system repeating the dark measurement to re-calibrate the thermal noise at each discrete data-point. Thus it becomes very time consuming to obtain the various different components of RIN for the entire frequency range which is defined by 800 different sampling points. This can be an issue for the accuracy of the measurement because the alignment of the lensed fiber to the laser will drift over time, which could lead to false readings of the RIN. For this study, we sampled four different frequency points across the 100 MHz to 10 GHz frequency range chosen for the RIN study to obtain the true laser RIN. Figure 6.5

and Figure 6.6 shows the evolution of the total measured system RIN versus feedback at four different frequencies in the total RIN spectrum for a quantum dot laser and a heterogeneously integrated quantum well laser, each biased at $2 \times I_{th}$, respectively. Also plotted are the various contributions to the total system RIN, broken down into the laser noise, thermal noise, and shot noise. The thermal and shot noise components remain fairly constant across the different feedback levels, as would be expected since the feedback has no impact on the built in electronics and at these levels a minimal impact on the output power. We see that for both the quantum dot and the quantum well case the low frequency noise is the most sensitive to optical feedback, which we will focus on in the subsequent sections.

6.4 Results and discussion

6.4.1 Comparison of low frequency RIN versus feedback

Figure 6.7 shows the low frequency laser RIN at 100 MHz (with thermal and shot noise subtracted out) for two different heterogeneously integrated quantum well lasers compared to two different quantum dot lasers on silicon, each subjected feedback levels varying approximately from -60 to -10 dB. For each laser, RIN was measured for five different bias currents (and corresponding output powers). Of note is the observation that the low frequency RIN at 100 MHz for the quantum well lasers show a sharp increase with increasing feedback for each bias current, up to 30 dB. On the other hand, RIN for the quantum dot lasers show a much smaller increase with increasing feedback, with the largest increase for each bias current being roughly 10 dB within the same measurement range. The RIN values of the quantum dot lasers at the highest level of feedback (-10 dB) are matched by the quantum well lasers at nearly 20 dB weaker feedback levels (-30

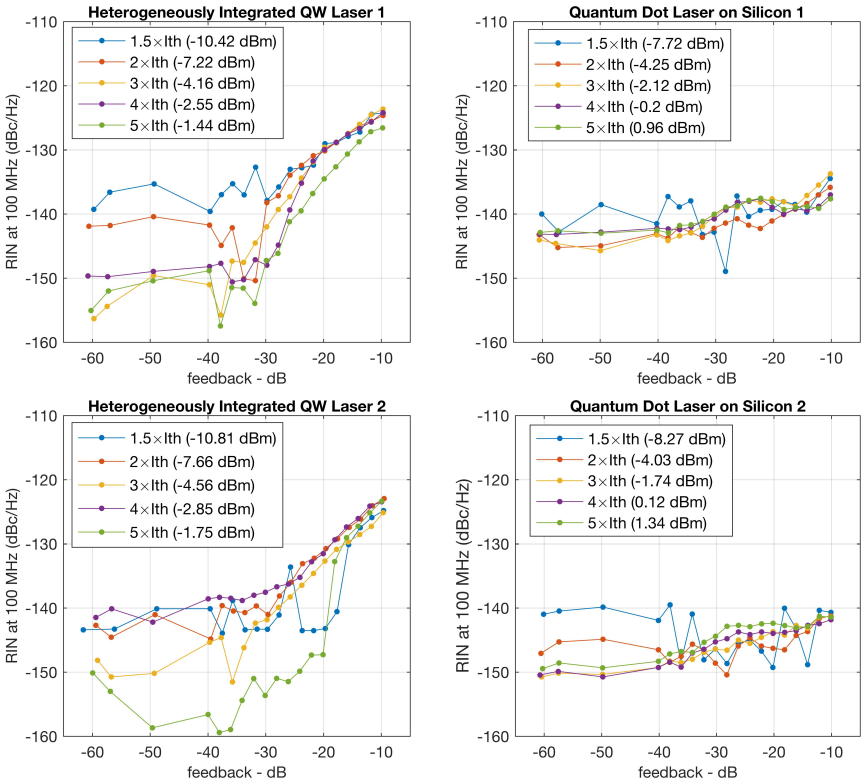

Figure 6.7: Laser RIN at 100 MHz with thermal and shot noise subtracted out versus various levels of optical feedback for two different heterogeneously integrated quantum well lasers (left) and two different quantum dot lasers on silicon (right). The legend indicates the bias current applied to the laser as well as the optical power received at the spectrometer. While the quantum well lasers sometimes exhibit increases in RIN up to 30 dB over the range of feedback values, the variation in RIN for the quantum dot lasers is limited to within 10 dB of the measured bias currents.

dB).

6.4.2 Comparison of noise spectrum at weak and strong feedback limits

The coherence collapse regime is characterised by the appearance of satellite modes appearing at roughly multiples of the relaxation oscillation frequency away from the main lasing mode [104]. Figure 6.8 shows the measured system RIN - the sum of laser, thermal, and shot noise - of a heterogeneously integrated quantum well laser as well as a quantum

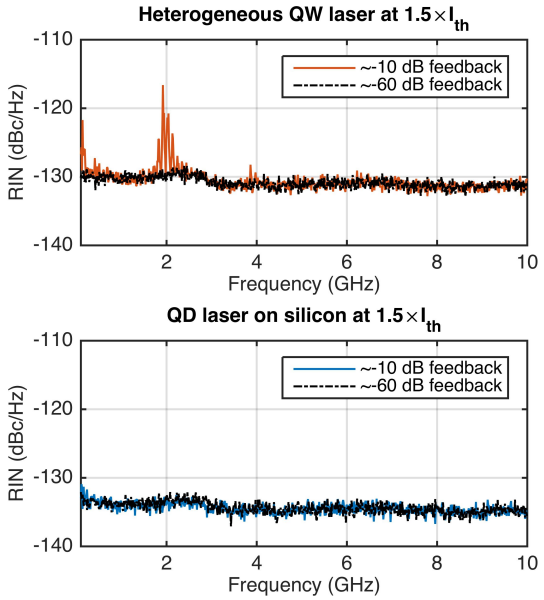

Figure 6.8: Total system RIN from 100 MHz to 10 GHz, for quantum well and quantum dot lasers biased at $1.5\times I_{th}$. The measured quantum well lasers exhibited signatures of coherence collapse, while this is not observed in the quantum dot lasers.

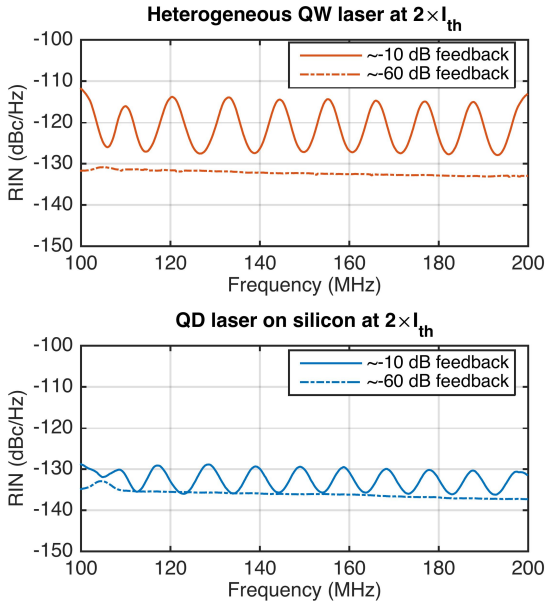

Figure 6.9: Measured low frequency system RIN at weak and strong feedback levels at $2\times I_{th}$. Enhanced RIN peaks are visible under strong feedback for both types of lasers at frequencies separated by the external cavity roundtrip frequency. However the increase under strong feedback is much less for the quantum dot laser.

dot laser, both biased at 1.5×I_{th}. In each case, RIN was measured at the maximum and minimum attainable values of feedback with our testing setup. In the weak feedback limit (∼-60 dB), the laser RIN of both lasers is below the thermal noise floor and the spectrum - essentially the thermal noise - is fairly flat. In the strong feedback limit (∼ -10 dB), the RIN spectrum for the quantum well laser exhibits signatures of coherence collapse, with groups of large spikes in the RIN spectrum separated by presumably the relaxation oscillation frequency of roughly 2 GHz, which has been previously measured for other heterogeneously integrated quantum well lasers [105]. The RIN spectrum for the quantum dot lasers is almost unchanged, with only a small increase in the low frequency RIN. This corroborates the predicted higher threshold of coherence collapse for quantum dot lasers compared to quantum wells. Figure 6.9 shows the low frequency RIN for both lasers at 2×I_{th} from 100 to 200 MHz, averaged over 10 scans to better resolve the spectral features. Under strong feedback, enhanced RIN peaks separated by ostensibly the external cavity roundtrip frequency are visible for both types of lasers, with a slightly smaller spacing for the quantum dot laser due to the longer external cavity length. In agreement with the data shown in Figure 6.7, the overall increase in RIN is lower for the quantum dot laser over the frequency range measured. Along with the data presented in Figure 6.8, we can conclude that the increase in total integrated RIN will also be larger for the quantum well lasers relative to the quantum dots.

6.5 Saturation effects in quantum dot lasers

The quantum dot lasers studied in the above section were devices that conformed with the average yield and lased (predominantly) from the ground state. One feature of quantum dots is that because the number of dots per sheet is finite, their density of states and thus maximum gain is also finite and can be saturated. This is unlike the

case in quantum well lasers where for all intents and purposes the density of states is infinite. In certain cases, quantum dots are known to lase from the first excited state if the ground state gain is insufficient to overcome cavity losses, or exhibit dual-state lasing behavior once the ground state gain has been saturated. We have speculated in Chapter 4 that these saturation effects may be important from a lifetime perspective, since the likelihood of carriers outside of the dots increases as the ground state gain is saturated, where they are free to recombine non-radiatively. In addition, the α factor of quantum dot lasers is highly dependent on the presence of saturation effects as well, often manifesting as a strong dependance on the applied current [116, 110].

Previous studies - both experimental and theoretical - have shown that the α factor can diverge to large values (> 10) for quantum dot lasers operated near full inversion of the ground state. In accordance with (6.1), this would then translate to a smaller coherence collapse threshold. In the course of this study we identified a few quantum dot lasers with yield defects which were quite noisy, especially under strong feedback. Figure 6.10 shows the measured RIN data for one such device - labeled B13. We observe a higher than average increase in the low frequency RIN versus feedback. Furthermore we see signatures of coherence collapse in the full RIN spectrum under strong feedback, while biased at $4 \times I_{th}$ (200 mA). We were able to correlate this increased sensitivity to feedback with the presence of excited state lasing, which is an indication of saturated ground state gain. Figure 6.11 shows signatures of gain saturation and excited state lasing in this device. Of note is the fact that in the LI curve comparison, the two devices are nominally made from the same material and with the same cavity size. However, the larger threshold and lower slope efficiency suggests that the cavity of B13 is lossier, meaning that the laser is operating closer to gain saturation. A closer examination reveals a kink in the LI curve at around 180 mA, typically an indication of the onset of excited state lasing. The optical spectra of B13 biased at 200 mA confirms this, as a lasing peak

near 1220 nm is clearly visible in addition to the ground state lasing peaks near 1280 nm.

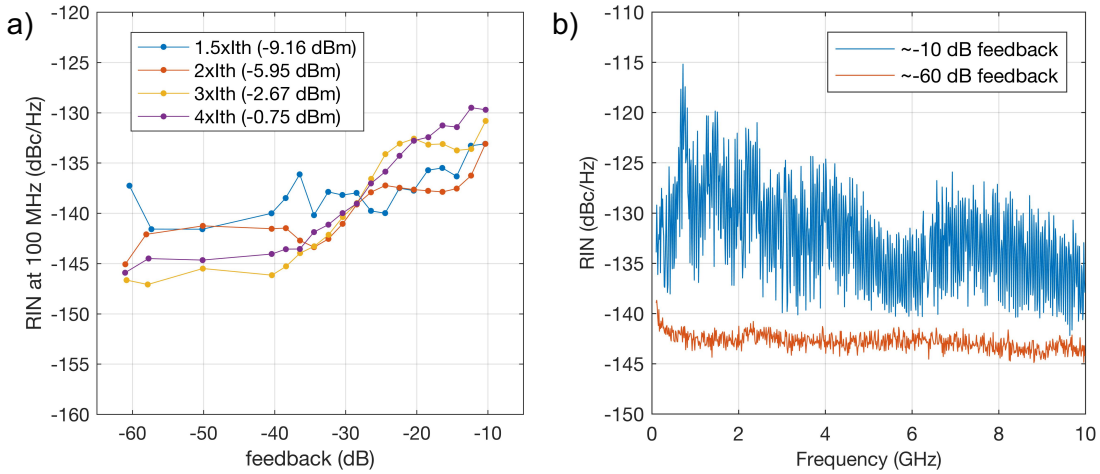

Figure 6.10: a) The low frequency RIN versus feedback of a 1 mm×3μm QDL on Si, showing higher than average increase in RIN versus feedback. b) The entire RIN spectrum of the same device at 4 × I_{th} (200 mA) showing signatures of coherence collapse.

6.6 Summary

The reflection sensitivity of quantum dot lasers epitaxially grown on silicon was studied for the first time. Compared to heterogeneously integrated quantum wells, the quantum dot lasers show nearly 20 dB reduced sensitivity to feedback while maintaining low levels of RIN over the entire feedback range. These results demonstrate their potential for isolator free operation, an important differentiation over quantum well lasers for achieving low system cost, size, weight, and power. We further demonstrated the importance of saturation effects in quantum dot lasers as related to their RIN and feedback tolerance properties, highlighting the importance of designing quantum dot lasers to operate far away from gain saturation.

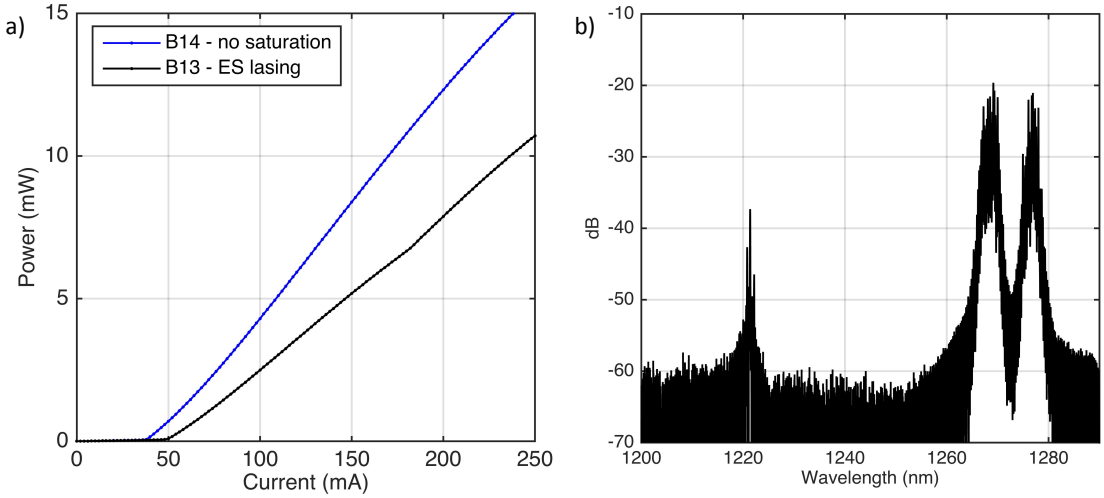

Figure 6.11: a) Comparison of the LI curves between two devices with the same nominal material and cavity size. B13 is the device with high RIN, and B14 is the quantum dot laser in Figure 6.8, Figure 6.9, and 'QD Laser 1' in Figure 6.7. For B13 a kink in the LI curve at around 180 mA is visible, which is typically an indication of the onset of excited state lasing. b) The corresponding optical spectrum of B13 at $4 \times I_{th}$ (200 mA) showing a lasing peak at 1220nm, confirming lasing from an excited state.

Chapter 7

Conclusions and Future Work

7.1 Summary

Several advances of quantum dot lasers for silicon photonics focusing on direct epitaxial growth onto silicon (both offcut and on-axis) have been reported in this thesis. In Chapter 3 we reported 1.3 μm InAs/GaAs quantum dot lasers grown on offcut Ge/Si substrates demonstrating continuous wave lasing up to 119°C, 176 mW of output power, and thresholds down to 16 mA. A comparison with $In_{0.2}Ga_{0.8}As$ quantum well lasers grown on the same Ge/Si substrates which failed to lase demonstrated the reduced sensitivity to dislocations of quantum dot lasers. Reliability of the aforementioned devices was reported in Chapter 4. A mean time to failure of 4700 hours has been achieved, which is more than 23x longer over the previously best reported lifetime for GaAs based lasers on silicon. The same quantum dot material was used to fabricate lasers on on-axis GaP/Si (001) substrates as reported in Chapter 5, an important consideration for integration with a traditional silicon CMOS foundry. Finally, measurements of the reflection sensitivity of quantum dot lasers on GaP/Si were presented and systematically compared to heterogeneously integrated quantum well lasers in Chapter 6. The quantum dot lasers

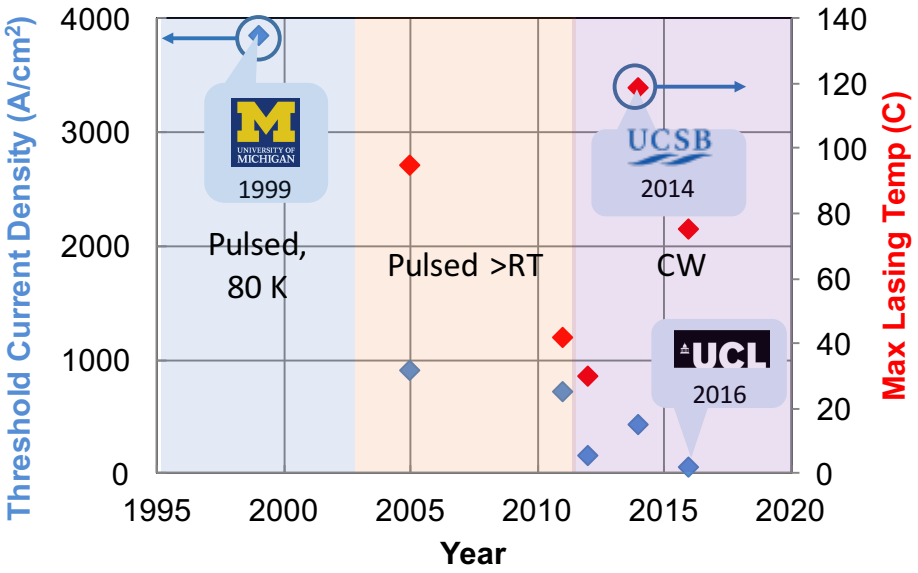

Figure 7.1: A graphical representation of the data presented in Table 1.3, illustrating the progress made with quantum dot lasers epitaxially grown on silicon thus far.

showed 20 dB suppression in feedback induced RIN, which suggests their potential for isolator free integration. A summary of the historical progress made in this field with recent results from this thesis included is shown in Figure 7.1, highlighting the rapid progress in recent years. In the sections below we briefly outline some possible avenues of future research to further advance the field.

7.2 General improvements to quantum dots

Continued improvement of the quantum dot active region is the one common factor that will lead to improvements in all aspects of device performance (including static performance, reliability, and reflection sensitivity). A blueprint was provided in Chapter 2 towards this end. Figure 7.2 shows how changes in the most important parameters will qualitatively affect the modal gain versus current density characteristics benchmarked

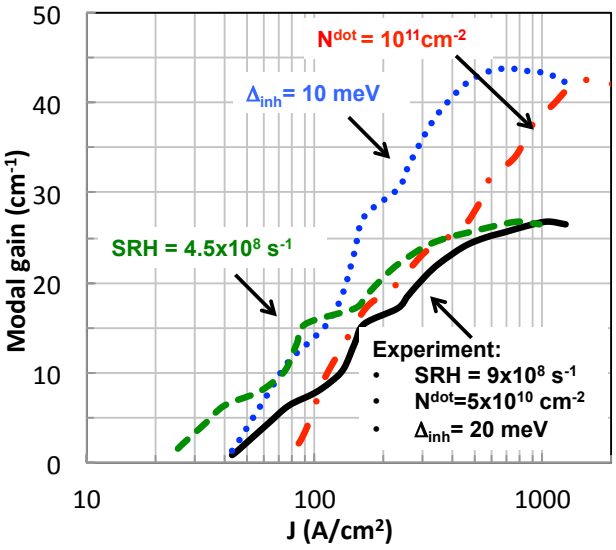

Figure 7.2: Predicted change in the modal gain versus current density against measured experimental results (black) for: doubling of the dot density (red), halving of the Shockley-Read-Hall recombination rate (green), or halving of the inhomogeneous broadening (blue), with everything else kept the same in each case [40, 56].

against the experimental results of this thesis. Significant improvements can be made to the currently still modest gain characteristics of our quantum dot lasers via increasing the dot density (to increase the maximum saturated gain at the expense of increased transparency current density), and decreasing the inhomogeneous broadening (to increase the maximum saturated gain by a factor of two without any trade-off in transparency current density) [40, 56].

The sheet density of any quantum dot layer is limited for a given wavelength by the minimum size needed to achieve said wavelength from confinement energies. For typical 1.3μm DWELL InAs quantum dots with an average diameter of 30nm, the maximum achievable density is $\sim 10^{11}$ cm^{-2} assuming near perfect packing (6×10^{10}cm^{-2} is the highest that has been achieved practically) [118]. The workaround to this limit would be to decrease the size of the quantum dots (e.g. by growing colder or faster) while increasing the indium content of the parent well such that the emission wavelength is preserved while

a higher density of quantum dots may be achieved. 15% InGaAs wells are currently being used, the indium content may possibly be increased up to around 20% without incurring additional dislocations from strain relaxation [48]. Antimony (Sb) assisted quantum dot growth may also provide an interesting pathway towards higher dot densities and/or improved uniformity. In this process the QD growth surface is irradiated with Sb to form a Sb-terminated surface prior to commencing growth, and/or a constant Sb flux is supplied throughout the QD growth process [119, 118]. Sb is known to have surfactant like properties and InAs deposited on a Sb terminated surface has been observed to form a high density of one dimensional wires prior to QD formation, which could provide an increased number of QD nucleation sites [118].

Increasing the localizing potential is necessary to decrease carrier escape out of quantum dots. This requires increasing the conduction band offset between the InAs quantum dot and its matrix material, and more importantly increasing the intersubband separation between the ground state and excited state within a quantum dot. Lasing at a record temperature of 220°C has been achieved with a high intersubband separation of 80 meV [31], while our current structures have only 70 meV separation. The quantization energy levels are predominantly determined by the z-confinement, but the in-plane confinement between the quantum dots provides another tuning parameter. For typical DWELL structures the in-plane and z confinement are controlled by the same capping/matrix material, which is typically some sort of $In_xGa_{1-x}As$ alloy. However it is well known that during deposition, the capping material tends to grow around the quantum dots first because the top of the quantum dots are strain relaxed and thus pose the largest lattice mismatch to the host/cap material [52]. By first depositing a GaAs layer that fills in the spacing between the quantum dots and finishing with a normal InGaAs cap the in-plane confinement may be increased due to the (slightly) larger band offset obtained with GaAs. However it remains to be seen whether this would lead to other issues with

In-Ga interdiffusion during higher temperature overgrowth steps. We note that this technique has been applied with AlAs for increasing the confinement potential of quantum dot micropillars [120].

An alternative method to increase the effective confinement potential and intersubband spacings is shown in Figure 7.3. In a typical DWELL structure such as the one we currently use, a thin (2 nm) InGaAs buffer is first grown prior to the deposition of InAs quantum dots, and is a well established method to enhance the dot density [48]. We may instead directly nucleate on GaAs and cap with a two step GaAs/InGaAs cap with a relatively higher Indium content to maintain the same emission wavelength. In this manner the effective confinement is increased for the quantum dots (by virtue of the slightly larger band offsets with InAs/GaAs vs InAs/InGaAs), the intersubband spacing within a quantum dot is increased (dots are smaller so the energy separation is greater). There may be a trade-off in the dot density, which may need to be compensated for. Of course, each of these different growth details must be optimized separately. It is also unclear the extent to which the laser injection efficiency will suffer from this new scheme, as the DWELL scheme is beneficial for increasing injection efficiency by funneling carriers into the quantum dots.

7.3 Prospects for improving reliability

At present, the typical reliability requirement for optical transmission systems is 100 FIT (100 failures in 10^9 device hours) or a median time to failure (MTTF) in excess of 10000000 h under full rated power [73]. Longer lifetimes are to be expected by increasing the ratio of lasing quantum dots to dislocations. The latest advances in self-assembled 1.3 μm InAs quantum dot growth indicates that it is possible to achieve at least a 50% increase in dot density and improved dot uniformity from the present work [121]. Further,

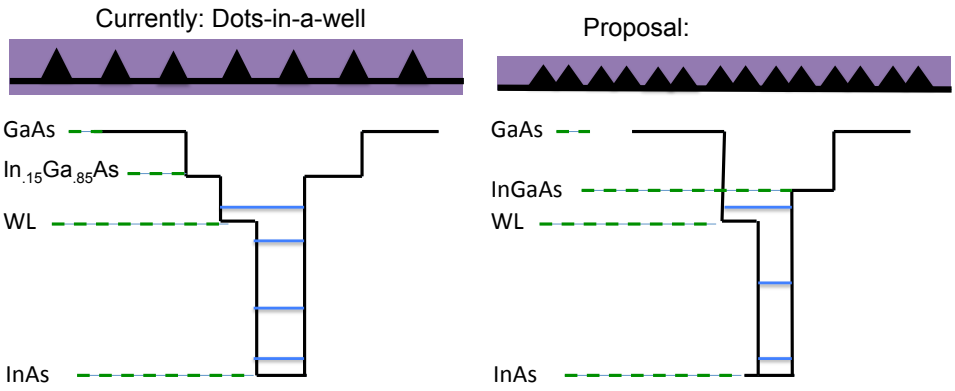

Figure 7.3: Increasing the intersubband level separation by removing the underlying InGaAs buffer, growing a high density of smaller dots, and capping with a higher indium content well to maintain the lasing wavelength.

it is reasonable to expect at least one or two orders of magnitude decrease in defect density from optimized Ge buffers or strained layer superlattices [80, 122]. Combining such improvements of the quantum dot gain region with reductions in defect density is expected to produce reliable and efficient laser operation in future devices.

An in-depth discussion on the various factors affecting the lifetimes of quantum dot lasers on silicon was given in Chapter 4. To summarize, we can assume that the degradation is predominantly caused by defect growth driven by non-radiative recombination current, which is determined by both % of injected carriers captured by QDs (i.e. dependent on dislocation density and dot density), and current density in active region (i.e. threshold current density, which somewhat clamps at threshold). The data in Chapter 5 also revealed that the majority of the reduction in performance between quantum dot lasers on native GaAs substrates to those grown on silicon is accounted for through a reduction in the injection efficiency. So to first order, the quickest route to improving lifetime is through the following factors:

1. reducing initial dislocation density, which seeds the degradation through dislocation climb

2. improving quantum dot density/uniformity which competes with dislocations for carriers, as well as determining what the gain curve looks like (and subsequently threshold)

3. device design to minimize the threshold current density, which reduces carrier heating effects

4. minimizing quantum dot saturation effects through quantum dot growth optimization or stacking, and minimizing cavity loss

We further point out two cases in literature that are worth studying. The first is the success of GaN for both LEDs and lasers despite the lack of high-quality, low dislocation density free-standing substrates. In the case of GaN, high efficiency LEDs have been made despite the prescence of large dislocation densities $10^{10} - 10^{12}$ cm^{-2} [123]. This has been postulated to be due to very short minority carrier diffusion lengths in the active region material (i.e. as long as the minority carrier diffusion length is less than the spacing of dislocations, high efficiency LEDs can be made). InGaN UV laser diodes with lifetimes in excess of 10000 hours have been demonstrated [123].

The second case is the fact that InP/InGaAsP laser diodes seem to be in general more reliable than GaAs/AlGaAs based laser diodes, and do not suffer from rapid degradation phenomena caused by recombination enhanced dislocation climb [11]. Mechanical properties aside, the major reasons are theorized to be that the bandgap of InP compounds are lower and thus maximum energy supplied by non-radiative recombination is less. Furthermore, trap states related to intrinsic vacancies in InP/InGaAsP are hypothesized to be above the conduction band, i.e. no mid-gap states which significantly reduces the likelihood of non-radiative recombination. As a result, dislocation induced climb (a major cause of failure in GaAs based laser diodes) is much less of an issue in InP/InGaAsP based laser diodes.

7.4 Quantum dot nanolasers on silicon

Significant reductions in size, cost, and power consumption of optical interconnects are desirable to facilitate their implementation in high volume short-reach communication links (i.e. chip to chip or shorter) [124]. Here we consider the possibility of quantum dot enabled nanolasers epitaxially grown on silicon as a low cost, low SWaP (size, weight, and power) light source in silicon photonic integrated circuits to meet these requirements. Such nanolasers would contain one (or multiple) layers of a high uniformity ensemble of III-V quantum dots embedded in a low loss cavity a few tens of square microns in area grown on silicon. A quantum dot based nanolaser configuration on silicon presents several advantages:

- The combination of a low transparency current density quantum dot active region with a miniaturized low loss cavity can produce the very low lasing thresholds necessary for low power consumption optical links (see Figure 7.4).

- By limiting the total device area to tens of square microns or less, epitaxial necking and dislocation image forces can facilitate dislocation glide out of the crystal sidewalls, and the total dislocation count within the active layers can be very low [125, 126]. The use of a quantum dot active region is expected to further mitigate any negative effects from residual dislocations, as was demonstrated above in section 2.

- The small form factors of these devices also lends itself to higher on-chip integration densities, favorable from an energy efficiency perspective to minimize interfacial coupling losses and signal attenuation, and necessary to achieve high interconnect bandwidth density [124, 127].

- Epitaxial growth will allow this technology to scale with the largest available silicon

wafer size, taking advantage of economies of scale not available for III-V substrates. Changing from a continuous planar epi coverage to limited area epitaxy in this case reduces the total amount of accumulated thermal stress in accordance with the reduced epi filling factor, which can mitigate wafer yield issues due to thermal stress induced cracking [128].

Figure 7.5 shows the computed thresholds (dashed) and current required for 0.5 mW of output power (solid) of InAs/GaAs quantum dot lasers of various different cavity lengths. Reducing the launch power of the laser may be beneficial for energy efficiency depending on the link design and utilization percentage. For any given link budget, it is desirable to minimize the current required to drive the laser to generate the required output power to overcome link losses. Thus we can imagine that for short-reach links where the output power requirement, Figure 7.5 indicates that the least power-hungry solution is to use smaller lasers which require less input current for the same amount of output power. In the sections below we examine various technical aspects of the proposed structure in detail.

7.4.1 Waveguide coupling

Figure 7.6 shows one approach to achieve waveguide coupling where the optical mode is butt-coupled to a silicon rib waveguide. In this embodiment, the III-V cavity is selectively grown onto the handle wafer of a SOI substrate and the height of the active region is aligned with the silicon waveguide layer to maximize optical coupling. The handle wafer can serve as a contact layer as well as an excellent heat sink for the III-V layers. Fig. 7.7 shows the calculated profile of the fundamental transverse electric (TE) mode for an InAs/InP quantum dot nanolaser stack side by side with a silicon rib waveguide with a partial etch depth of 250 nm and a total waveguide height of 500 nm. In this

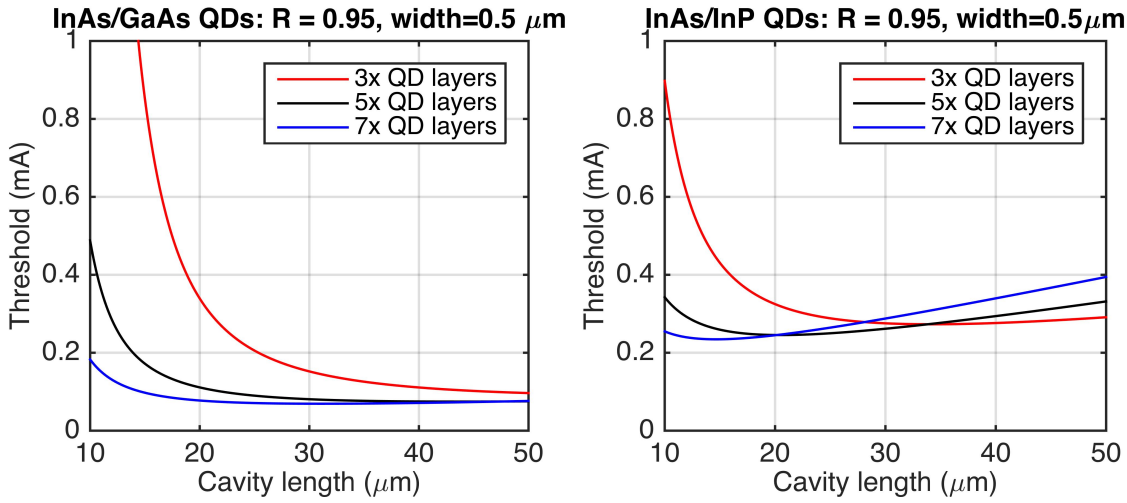

Figure 7.4: Scaled broad-area laser threshold currents versus cavity length for both GaAs and InP based quantum dots. A facet reflectivity R=95% was assumed for both cases. Gain parameters used are listed in Table 7.1. From [35], © 2015 Chinese Laser Press.

case, the maximum mode overlap is computed to be 92.35% (∼0.35 dB coupling loss, not accounting for reflections which will increase this figure). The etch depth of the partially etched silicon layers may be varied to tailor the transverse mode profile of both the III-V and silicon waveguide sections to further optimize the coupling efficiency.

7.4.2 High reflectivity mirrors

High mirror reflectivity is crucial in reducing mirror loss of short cavity lasers. Quantum dot lasers will also have a distinct advantage over quantum well lasers in terms of energy efficiency if the total cavity loss is low enough to allow for operation near the transparency current density, which will be inherently lower in quantum dot systems compared to quantum wells (see Figure 3.27). Possible approaches to reduce mirror loss include: high quality factor (Q) ring cavities, Bragg reflectors (distributed feedback or distributed Bragg reflectors), dielectric mirrors, and metallic mirrors. Figure 7.8 shows a schematic for the various types of mirrors.

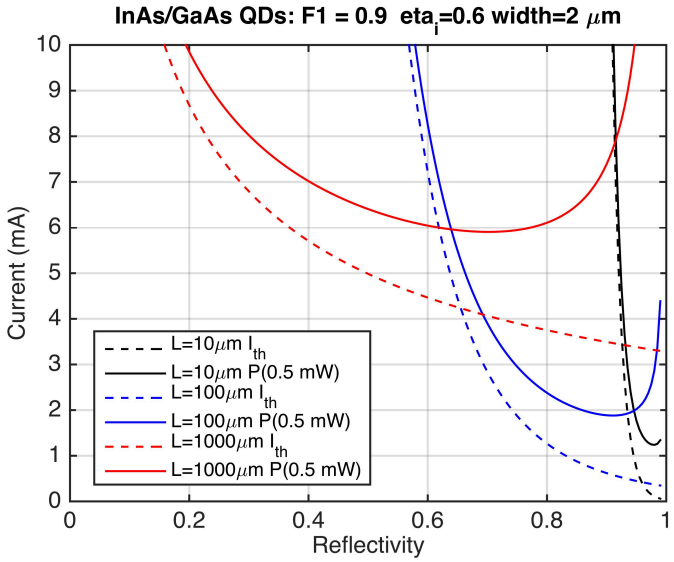

Figure 7.5: Computed thresholds (dashed) and current (solid) required for 0.5 mW of output power (solid) of InAs/GaAs quantum dot lasers of various different cavity lengths. Gain parameters are listed in Table 7.1.

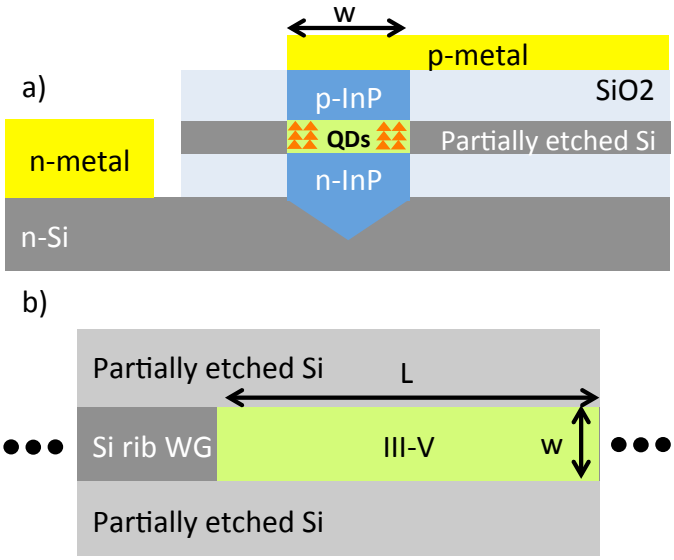

Figure 7.6: (a) A transverse cross-sectional schematic of the proposed quantum dot nano-laser where the output is butt coupled to a Si rib waveguide (WG); (b) a top–down view of the active region plane. The active region is aligned to the thicker Si rib waveguide to maximize coupling while the partial etch depth can be varied to tailor the transverse index profile. A calculated mode profile is shown in Fig 7.7. From [35], © 2015 Chinese Laser Press.

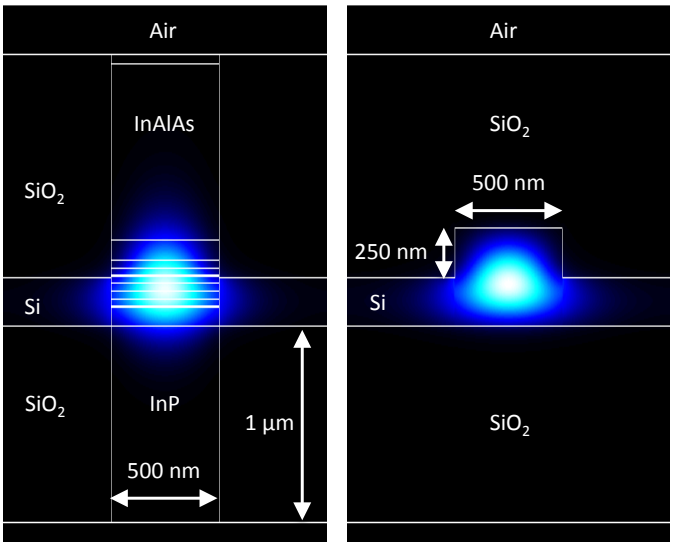

Figure 7.7: Calculated fundamental TE mode profiles of an InAs/InP quantum dot nanolaser on SOI with seven quantum dot layers (left) and a half etched Si rib waveguide to which the laser may be butt coupled to (right). The estimated coupling loss due to mode overlap is $\sim$ 0.35 dB. The confinement factor for the quantum dot layers is $\sim$1.95%. The depth of the partially etched Si layers may be varied to tailor the transverse index/mode profile to maximize coupling. From [35], © 2015 Chinese Laser Press.

Bragg reflectors are a preferable choice for obtaining high reflectivity with low loss, where the reflection strength can be tailored by the etch depth and number of grating periods. In our proposed structure the Bragg reflectors can be realized by etching gratings in the silicon waveguide or as distributed feedback gratings in the upper cladding layer (see Figure 7.8 a&b). First order Bragg gratings require high precision lithography and etching. Higher order gratings may simplify fabrication but at the expense of some excess mirror loss due to variations in duty cycle.

Metallic mirrors can provide polarization and wavelength independent reflection with relatively simple fabrication. However, the material loss limits the reflection to $\sim$97.5% [129]. Two metal plugs deposited on either side of the laser can form a high quality factor (Q) resonator (Figure 7.8 c), and the light can be coupled out using a directional coupler parallel to the active region as described in [129]. A combination of metal mirror on one

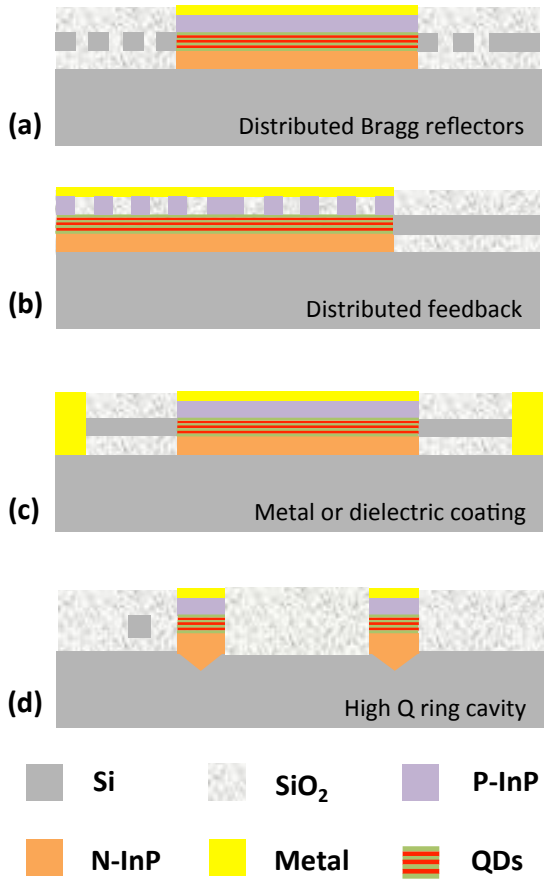

Figure 7.8: Schematic of the longitudinal cross-section for an InAs/InP quantum dot nano-laser showing different possible mirror designs: (a) distributed Bragg reflector mirrors in silicon, (b) distributed feedback gratings, (c) metal or dielectric high reflection coatings, (d) high Q ring cavity coupled to an output waveguide (shown on the left traveling perpendicular to the page). From [35], © 2015 Chinese Laser Press.

side and a Bragg mirror on the other can also be used for a uni-directional output. High reflection metal or dielectric facet coatings are also an option, but would have limited applicability for on-chip light sources.

High Q ring cavities may be used to achieve low cavity loss in place of conventional Fabry-Perot cavities. In this configuration, light from a whispering gallery mode circulating inside the ring cavity can be coupled to a nearby silicon waveguide, shown in Figure 7.8 (d). Additional reflectors can be defined on one end of the silicon waveguide to achieve unidirectional lasing, as described in [130].

7.4.3 Surface recombination

Surface recombination can be a dominant factor in determining device performance and reliability of small devices. Improved lateral carrier confinement in quantum dots with respect to quantum wells is yet another compelling reason to employ quantum dots for nanolasers, which can significantly reduce the surface recombination current compared to quantum wells [39, 41]. The impact of surface recombination on the scaling of the broad-area threshold current for both InAs/GaAs quantum dots and InAs/InP quantum dots is quantified here by following the approach outlined in [41], where it was shown that InAs/GaAs quantum dot lasers have an order of magnitude lower surface recombination velocities and ∼5x shorter mean ambipolar diffusion lengths compared to InGaAs/GaAs quantum well lasers. In these calculations a simple rectangular fully etched mesa was assumed. From simulations of various waveguide geometries, the lateral TE mode cutoff is around 0.5 μm, which we took for a lower bound ridge width in the calculations. Changes in lateral confinement versus ridge width was accounted for via the effective index method, although the magnitude of the variation versus width was not large ($\sim$ 5% reduction at a width of 0.5 μm).

The different parameters and assumptions used are listed in Table 7.1. The results are shown in Figure 7.9 and Figure 7.10. Although the overall threshold of GaAs based quantum dots are lower, the threshold at a ridge width of 0.5 μm and assuming an ambipolar diffusion length of 1 μm is 5.88x the scaled broad-area laser threshold, whereas InP based quantum dots show a 2.6x increase due to the lower surface recombination velocity. Despite the high surface recombination current at sub-micron scales, very low thresholds are still achievable. If the optical properties of InAs/InP quantum dots can be improved to the level of InAs/GaAs quantum dots, they may be a superior material system for nanolasers due to the reduced recombination velocity. Various surface treatments and

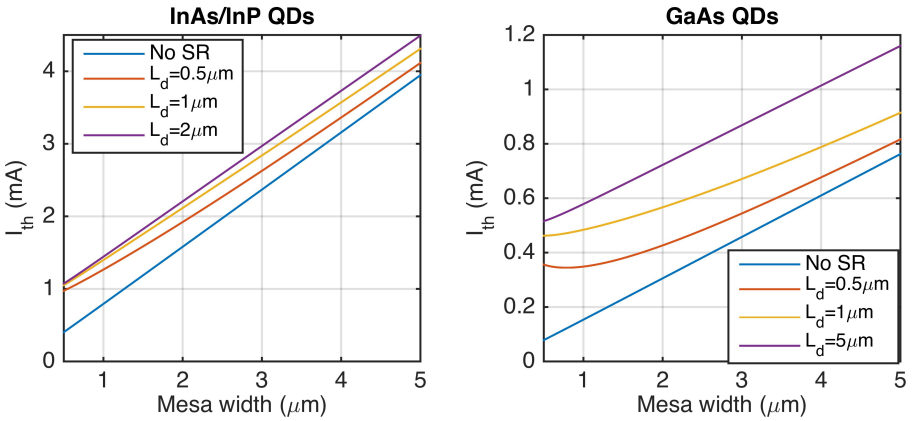

Figure 7.9: Calculated threshold currents versus ridge width for both GaAs ($v_s = 5 \times 10^4$ cm/s) and InP ($v_s = 1 \times 10^4$ cm/s) quantum dots and various diffusion lengths. A mean diffusion length of 1 μm was reported in [41]. A cavity length of 50 μm, R=95%, and 7 quantum dot layers were assumed for both cases (see Table 7.1). From [35], © 2015 Chinese Laser Press.

passivation techniques may be used to further reduce the surface trap density and the surface recombination velocity [131, 132, 133].

7.5 Conclusion and Outlook

In the last few years, incredible progress has been made in the development of 1.3 μm InAs/GaAs quantum dot lasers epitaxially grown on silicon. Work remains to elevate the performance of these devices towards native substrate levels, and to solve the remaining lifetime issues. An outline towards achieving these goals was provided in this thesis. Various avenues of research rich in physics a well as device applications lie ahead, enabled by quantum dot active regions. I look forward to continuing to assist in and witnessing the further growth of this field.

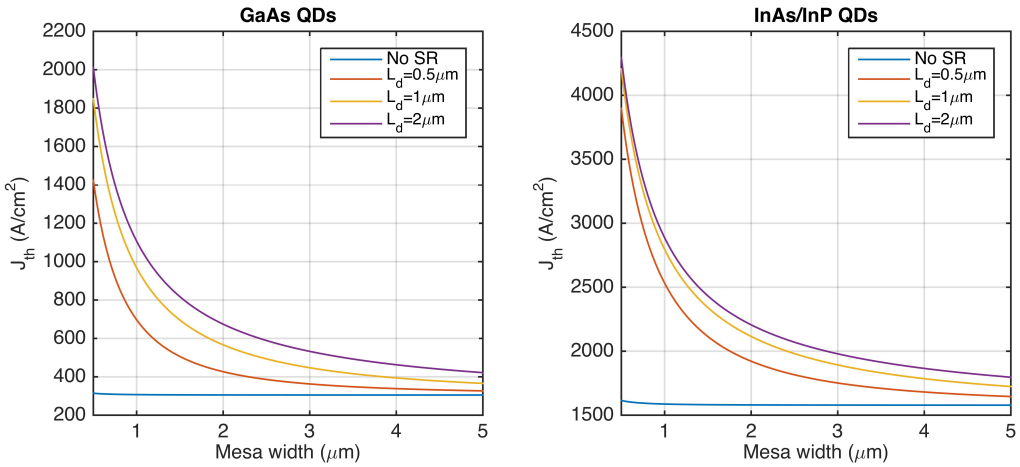

Figure 7.10: Corresponding threshold current densities for the devices shown in Figure 7.9.

	InAs/GaAs	InAs/InP
v_s (cm/s)	5×10^4	1×10^4
τ (ns)	2.8	2.8
α_i (cm^{-1})	3.16	4
J_{tr} (A/cm^2)	11.6	39
η_i	0.6	0.26
Γg_{0J} (cm^{-1} per layer)	2.36	5
R	0.95	0.95

Table 7.1: Parameters used for the calculations in Figures 7.4 and 7.9. Gain and loss values are from Fig Figure 7.2 for InAs/GaAs quantum dots and [33] for InAs/InP quantum dots. Recombination velocities and carrier lifetimes are from [132, 41].

Appendix A

Growth rate calibrations in MBE

A.1 GaAs/AlAs growth rate cals

Growth rate calibrations for GaAs and AlAs on GaAs substrates are determined by fitting a theoretical reflection spectrum to the real measured spectrum of a pair of microcavity samples (one where the λ cavity is made of GaAs, and another where it is AlAs) sandwiched by GaAs/AlAs DBR pairs. This method is detailed in Daniel Lofgreen's thesis (Chapter III page 38). In this thesis the cavity wavelength was set to 980nm (i.e. the nominal microcavity thickness is 980nm divided by $n(\lambda)$ - the refractive index of GaAs or AlAs at 980nm - and the thickness of the DBR stacks are quarter wavelength variations thereof - 980nm/(4*$n_{GaAs/AlAs}$). The structures grown are shown in Figure A.1. The actual resonant wavelength of this microcavity is theoretically determined by the thickness of the cavity layer plus the thickness and number of the individual DBR pairs (which affects the effective mirror length of the DBRs, and thus the total cavity length), and can be fitted to the measured spectrum (measured using the Cary 500 Spectrometer). An optimization scheme is used for the fitting which searches for the minimum of the inverse of the overlap integral between experimentally measured and theoretically calcu-

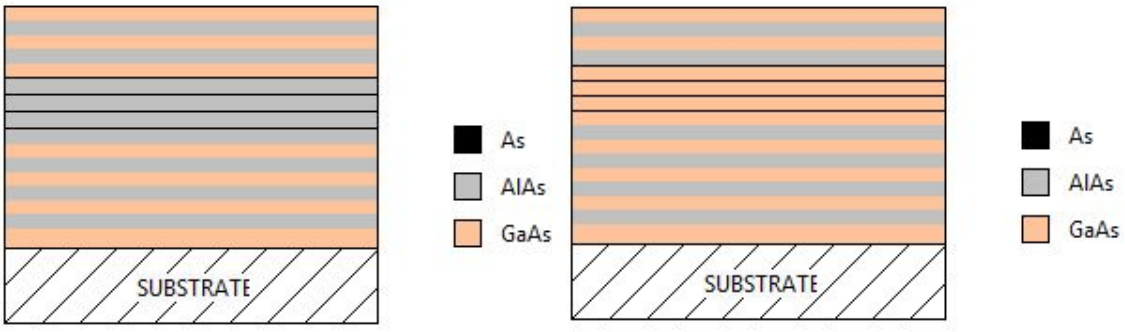

Figure A.1: The DBR microcavity samples used to calibrate GaAs and AlAs growth rates in this thesis. Using these two samples, the two unknowns (GaAs and AlAs growth rates) can be calculated by fitting the measured reflection spectrum of the microcavity samples with a theoretical curve.

lated reflection spectra, with the thickness of the DBR and microcavity layers varied to obtain the best fit. From the best fit, the actual layer thicknesses are extracted, and the actual growth rate calculated by multiplying the assumed growth rate with the ratio of (actual thickness/nominal thickness).

A.2 InAs growth rate cals

For QD growth on GaAs, we first obtain an estimate of the InAs growth rate using RHEED oscillations of InAs deposited on a native InAs substrate. RHEED oscillations are typically 1-5% off from the true growth rate due to the presence of flux transients immediately after the shutter opening. For QD growth, a second round of optimizations is usually done to optimize the amount of material deposited versus PL intensity and linewidth, so the small deviation from the true growth rate is not critical. A rapid check of growth rate accuracy can be done by by growing 8 nm $In_{0.2}Ga_{0.8}As$/GaAs PL cals, where the emission wavelength should be roughly around 980nm if the growth rates are accurate. These PL cals are usually grown as reference samples to ascertain

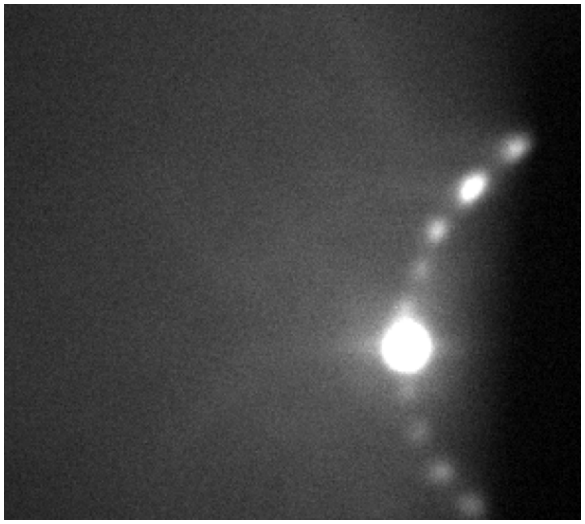

Figure A.2: RHEED of the InAs surface at 500°C after oxide desorption

system health throughout the growth campaign, and so large deviations in wavelength can indicate that the growth rates (or temperature) is off and needs to be recalibrated. The procedure for RHEED oscillations for InAs is as follows: four or more cell temperatures with corresponding fluxes roughly spanning the desired growth rates of interest are first measured in the morning of the calibration, to guarantee an accurate fit. A quarter of a 2" InAs wafer is loaded into the growth chamber, with the oxide desorbed by holding the wafer at 500°C for 10 minutes as read by an optical pyrometer, after which it should show a 4x reconstruction in one of the crystallographic directions (see Figure A.2). After oxide desorption, the Indium shutter is opened and InAs is grown at the highest cell temperature/growth rate of the series for enough time until a sufficiently thick ($\geq$ 200 nm) InAs homoepitaxial buffer layer has been deposited to smooth out the surface. After this is done, the shutter is closed, substrate temperature set to 470-480°C (no oscillations are observed at higher temperatures), the V/III ratio adjusted to between 10-20, RHEED beam blanked, the surface is given a few minutes to smooth out, then the calibrations begin. Using a specular spot in the RHEED, intensity oscillations are tracked using a software as the shutter is opened, with the shutter being closed once the oscillations are

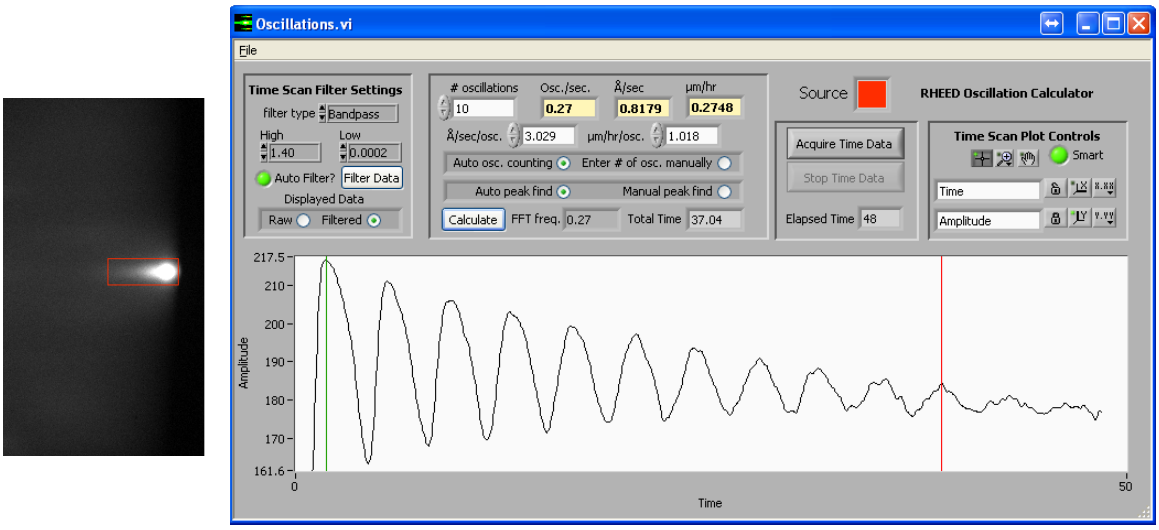

Figure A.3: Intensity oscillations (right) of the specular spot enclosed by the red box in the RHEED pattern shown on the left.

damped out and the RHEED beam blanked for 2-3 minutes to allow the surface time to smooth out before the next measurement. One oscillation is typically understood to be equal to the growth of one monolayer, and thus the average growth rate can be calculated by counting oscillations and converting to ML/s or A/s. Usually it is desirable to have many oscillations over a long deposition time to average out shutter transient effects, but because the InAs QD deposition time is very short, a smaller number of oscillations are ok and may actually better represent the real growth rates during deposition if oscillation observation time is close to the actual deposition time. In this thesis, typically 8-10 oscillations were used to compute the average growth rate from a single measurement.

This process is repeated to obtain at least five measurements per cell temperature, with the average value taken between the five. If the process is done correctly a standard deviation of less than 1% relative to the average among the measured growth rates should be possible for a given cell temperature/flux. After average growth rates for all the cell temperatures have been obtained, the average growth rate versus average cell flux can be plotted to generate a curve, and the growth rate should be roughly linear with cell flux.

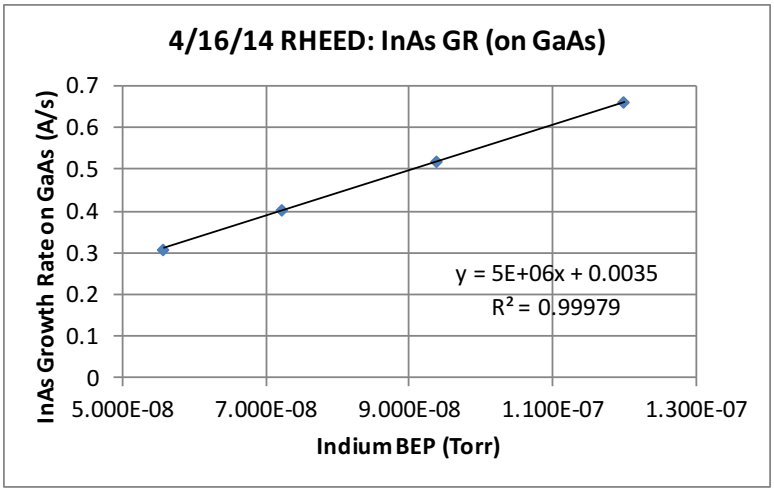

Figure A.4: Average growth rate versus indium flux determined from RHEED oscillations

The R^2 value from the fit should be $\geq$0.99 if the calibrations were done well. An example is shown in Figure A.4. Note that the measured growth rates are for growth on InAs. For QD growth on GaAs or InP where there is a difference in lattice constant with InAs, the growth rate will be slightly different if the material is pseudomorphically strained. The conversion factor is simply the ratio of the lattice constants cubed if growth rate is defined in A/s, or squared if defined as ML/s (i.e. $GR^{A/s}_{GaAs} = GR^{A/s}_{InAs} * (\frac{a_{GaAs}}{a_{InAs}})^3$).

A.3 InGaAs/InAlAs/InP lattice matching and growth rate cals

Unlike GaAs/AlAs which are naturally lattice matched binaries to GaAs substrates, growth of InP related compounds in Arsenic MBE without a phosphorous source requires the ternary system InGaAs/InAlAs or InAlGaAs to achieve lattice matching to InP. Thus, lattice matching conditions must be determined before doing growth rate calibrations. The nominal lattice matching compositions to InP are $In_{0.532}Ga_{0.468}As$ and $In_{0.523}Al_{0.477}As$, respectively. Lattice matching conditions for $In_{0.532}Ga_{0.468}As$ and

$In_{0.523}Al_{0.477}As$ were performed in System C as follows: with the indium flux held constant, a corresponding flux for either Ga or Al that yields the lattice matching composition is guessed from a previous growth. The Ga or Al cell temp is then varied to yield roughly plus and minus 5-10% of the nominal lattice matching flux (for 10% difference it is usually $\pm$ 5 degrees at the typical cell temperatures for 0.8 μm/hr growth rates). Then the following three-layer stack is grown on a semi-insulating InP substrate: nominally lattice matched InGaAs or InAlAs, InGaAs or InAlAs with 10% less Ga/Al, InGaAs or InAlAs with 10% higher Ga/Al. The layer thickness should be sufficiently thick to force metamorphic strain relaxation for accurate determination of the lattice constants, typically each layer was grown to be 500-750 nms. The samples are then measured in X-ray which should yield three distinct peaks and the substrate peak, each of the layer peaks corresponding to one of the three separate layers with its own corresponding average lattice constant. Plotting the lattice constants of the three layers versus the different Ga/Al fluxes, and finding the intercept point of the best fit line with the substrate lattice constant value should then yield the lattice matching flux of Ga/Al for the corresponding Indium flux used, see for example Figure A.5.

After the lattice matching conditions are determined, a pair of samples with superlattices are grown, where the nominal superlattice period (e.g. total InGaAs+InAlAs thickness) remains constant between the two samples but individual InGaAs and InAlAs cell thicknesses switched among the two. XRD is once again used to measure the fringe spacing in the samples due to the superlattice, from which the actual superlattice period is extracted (see Figure A.6). Two equations relating the measured superlattice thickness from the two separate samples can be written with the two unknown growth rates as the variables, solving the equations then yields the actual growth rates.

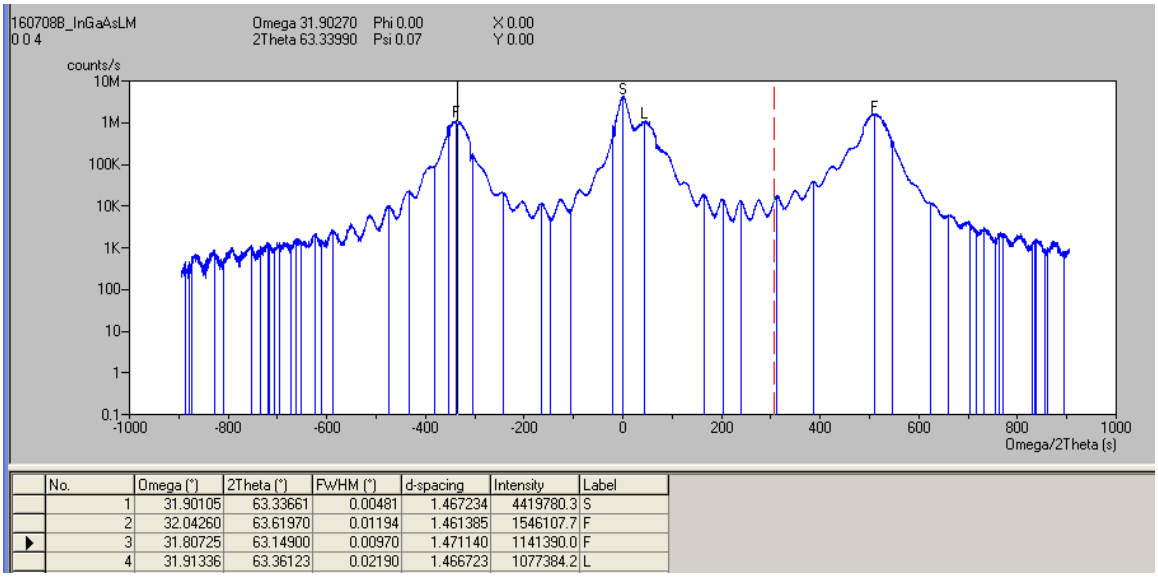

Figure A.5: XRD measurements of an InGaAs lattice matching calibration sample

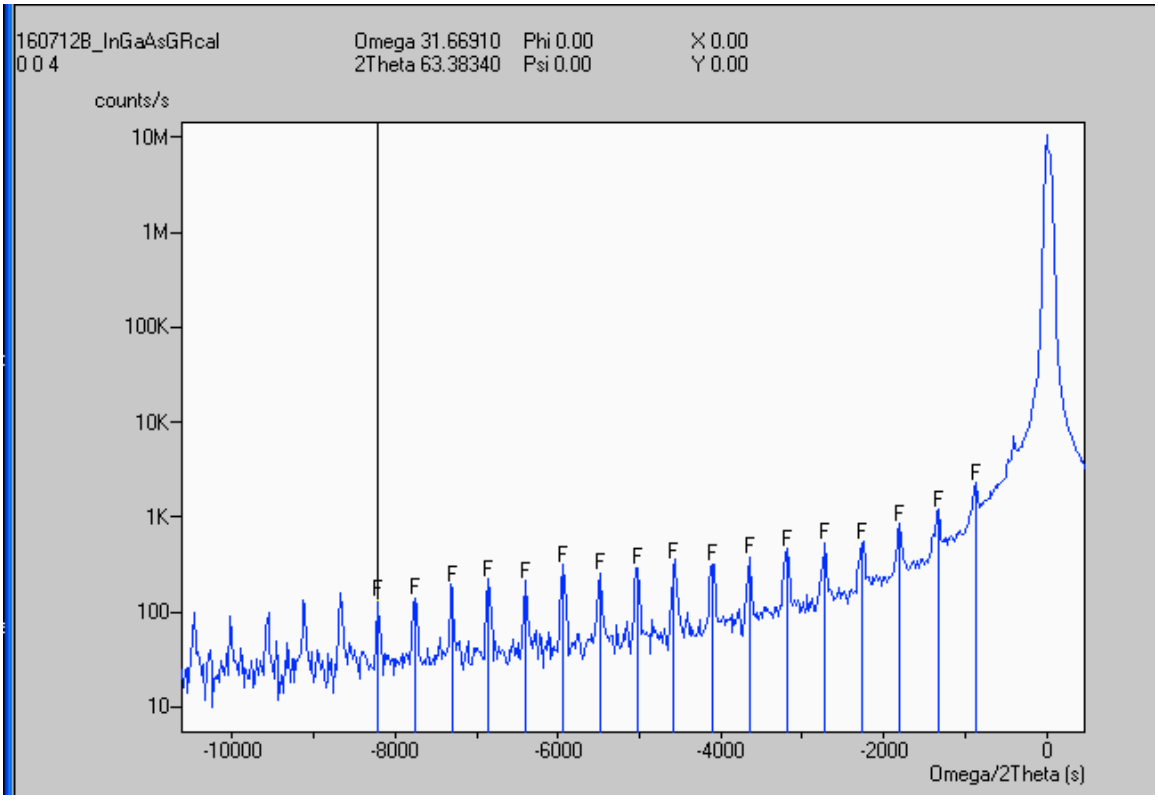

Figure A.6: XRD measurements of an InGaAs growth rate calibration sample

Appendix B

Facet polishing

In this thesis, most of the facets for the lasers on silicon were created by dicing and polishing (with some facets receiving high-reflection coatings). Facet polishing is hypothesized to be the biggest yield limiting step - as the facets are easy to damage and the polish quality can widely vary. This appendix shows the varying degrees of facet quality and some common mishaps encountered during polishing.

B.1 Polished facets

Typically, a well polished facet will look clean and fairly smooth under both optical and Nomarski microscope.

B.2 Scratched or dirty facets

When polishing hybrid facets, metal from the contacts can easily peel off and scratch the facet. Below is an example where the facet is severely scratched by the small pieces chipped off from the probe metal.

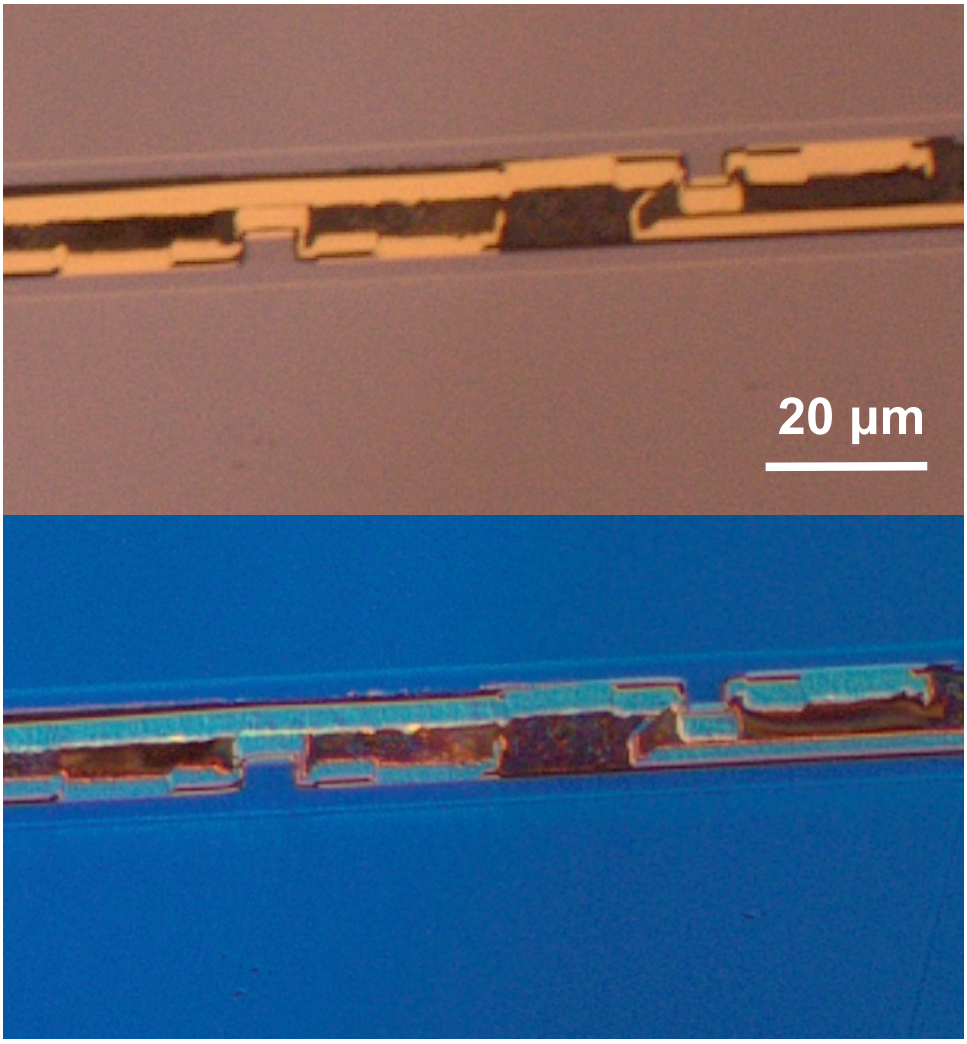

Figure B.1: Optical (top) and differential interference contrast (bottom) microscope images of polished facets.

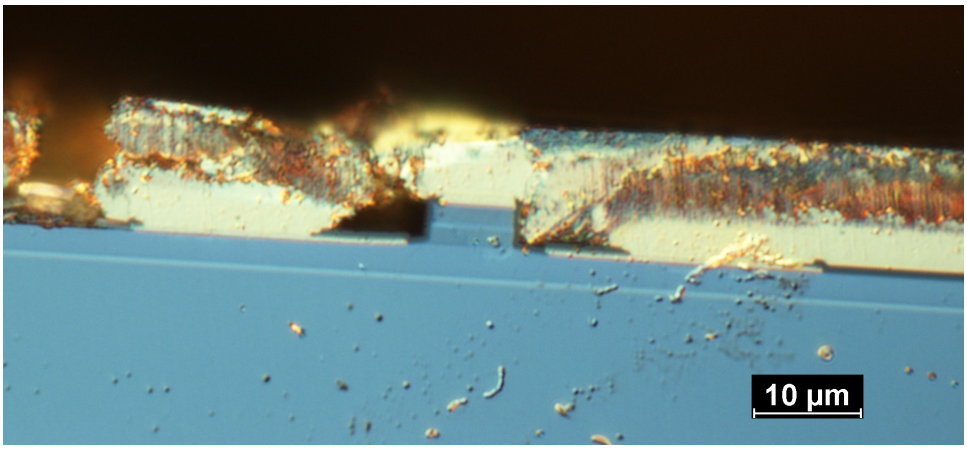

Figure B.2: Excessive chipping from the metal probe layers which subsequently compromises facet quality.

B.3 Cracked facets

Facet material can also easily chip off if not supported properly. Below is an example where this has happened.

B.4 HR coated facets

Sometimes the polished facets are coated with a layer of dielectric for either passivation or to increase the reflectivity. Adhesion problems can arise due to cleanliness of the facet or stress between the film and facet. Below is an example where a thin SiN layer is observed to have spalled.

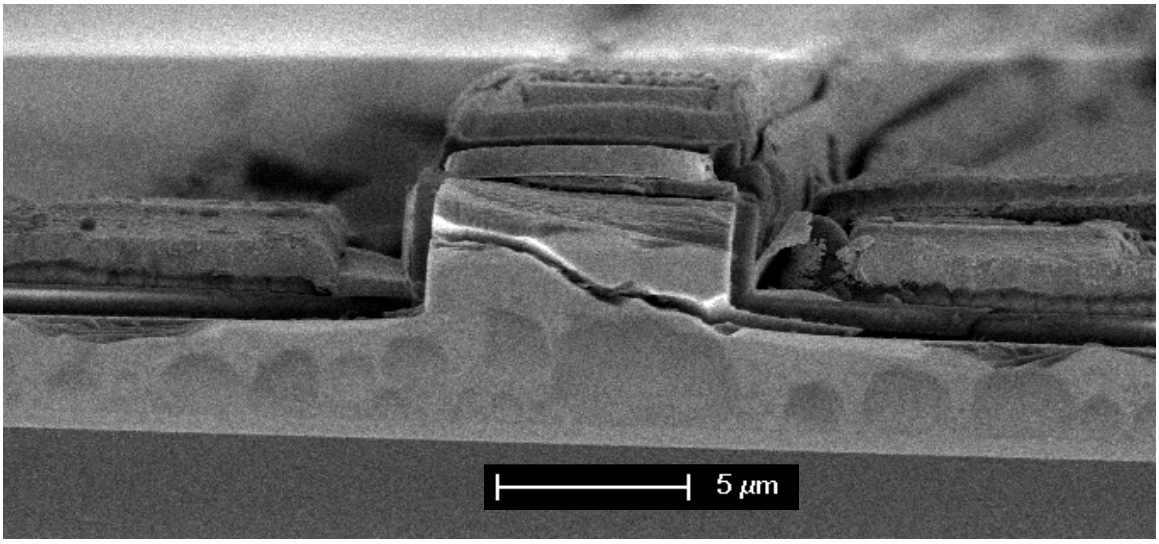

Figure B.3: A cracked facet from polishing.

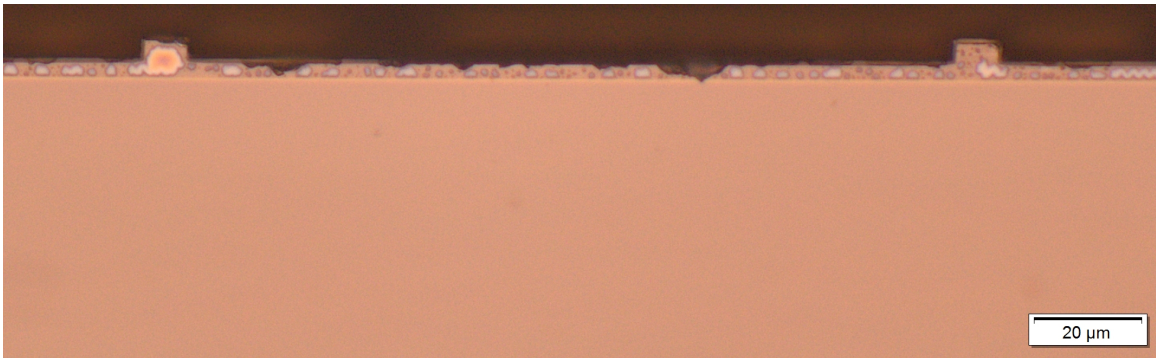

Figure B.4: Optical micrograph of facets with spalled SiN coating.

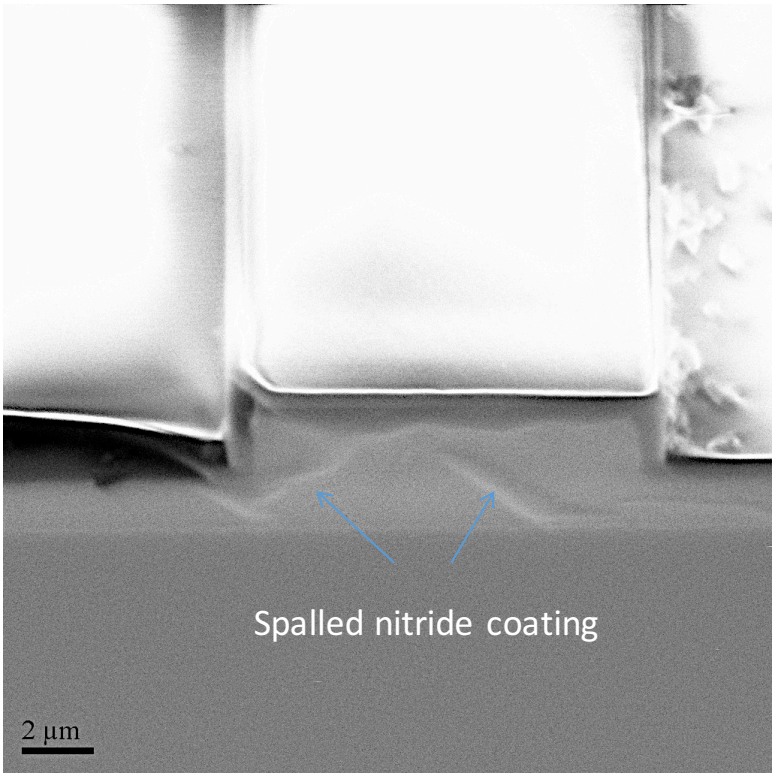

Figure B.5: SEM of a facet with spalled SiN coating.

Bibliography

[1] D. Thomson, A. Zilkie, J. E. Bowers, T. Komljenovic, G. T. Reed, L. Vivien, D. Marris-Morini, E. Cassan, L. Virot, J.-M. Fdli, J.-M. Hartmann, J. H. Schmid, D.-X. Xu, F. Boeuf, P. OBrien, G. Z. Mashanovich, and M. Nedeljkovic, "Roadmap on silicon photonics," *Journal of Optics*, vol. 18, no. 7, p. 073003, 2016.

[2] A. E. Willner, R. L. Byer, C. J. Chang-Hasnain, S. R. Forrest, H. Kressel, H. Kogelnik, G. J. Tearney, C. H. Townes, and M. N. Zervas, "Optics and photonics: Key enabling technologies.," *Proceedings of the IEEE*, vol. 100, no. Centennial-Issue, pp. 1604–1643, 2012.

[3] Z. Zhou, B. Yin, and J. Michel, "On-chip light sources for silicon photonics," *Light: Science & Applications*, vol. 4, no. 11, p. e358, 2015.

[4] D. Liang and J. E. Bowers, "Recent progress in lasers on silicon," *Nature Photonics*, vol. 4, no. 8, pp. 511–517, 2010.

[5] D. Liang, G. Roelkens, R. Baets, and J. E. Bowers, "Hybrid integrated platforms for silicon photonics," *Materials*, vol. 3, no. 3, pp. 1782–1802, 2010.

[6] T. Komljenovic, M. Davenport, J. Hulme, A. Y. Liu, C. T. Santis, A. Spott, S. Srinivasan, E. J. Stanton, C. Zhang, and J. E. Bowers, "Heterogeneous silicon photonic integrated circuits," *Journal of Lightwave Technology*, vol. 34, no. 1, pp. 20–35, 2016.

[7] S. Adachi, *Handbook of physical properties of semiconductors*, vol. 2. Kluwer Academic Pub, 2004.

[8] J. Yun, *High-Performance Quantum Dot Lasers and Integrated Guided-Wave Devices on Silicon*. PhD thesis, University of Michigan, 2008.

[9] H. Kroemer, "MBE growth of GaAs on Si: problems and progress," in *MRS Proceedings*, vol. 67, p. 3, Cambridge Univ Press, 1986.

[10] T. Egawa, Y. Hasegawa, T. Jimbo, and M. Umeno, "Effects of dislocation and stress on characteristics of gaas-based laser grown on si by metalorganic chemical vapor deposition," *Japanese journal of applied physics*, vol. 31, no. 3R, p. 791, 1992.

[11] O. Ueda and S. J. Pearton, *Materials and Reliability Handbook for Semiconductor Optical and Electron Devices*. Springer, 2013.

[12] Z. Mi, J. Yang, P. Bhattacharya, G. Qin, and Z. Ma, "High-Performance Quantum Dot Lasers and Integrated Optoelectronics on Si," *Proceedings of the IEEE*, vol. 97, no. 7, pp. 1239–1249, 2009.

[13] A. D. Lee, Q. Jiang, M. Tang, Y. Zhang, A. J. Seeds, and H. Liu, "InAs/GaAs Quantum-Dot Lasers Monolithically Grown on Si, Ge, and Ge-on-Si Substrates," *IEEE Journal of Selected Topics in Quantum Electronics*, vol. 19, no. 4, p. 1901107, 2013.

[14] A. Y. Liu, C. Zhang, J. Norman, A. Snyder, D. Lubyshev, J. M. Fastenau, A. W. Liu, A. C. Gossard, and J. E. Bowers, "High performance continuous wave 1.3 μm quantum dot lasers on silicon," *Applied Physics Letters*, vol. 104, no. 4, p. 041104, 2014.

[15] T. Liu, P. Petroff, H. Kroemer, and A. Gossard, "Electronic Properties of Dislocations in Heavily Dislocated Quantum Well Structures: Doping Effects," *Materials Research Society, San Diego, CA*, pp. 393–398, 1989.

[16] J.-M. Gerard and C. Weisbuch, "Semiconductor structure for optoelectronic components with inclusions," Dec. 24 1991. US Patent 5,075,742.

[17] K. Linder, J. Phillips, O. Qasaimeh, X. Liu, S. Krishna, P. Bhattacharya, and J. Jiang, "Self-organized $In_{0.4}Ga_{0.6}As$ quantum-dot lasers grown on Si substrates," *Appl. Phys. Lett*, vol. 74, no. 10, pp. 1355–1357, 1999.

[18] Z. Mi, P. Bhattacharya, J. Yang, and K. Pipe, "Room-temperature self-organised $In_{0.5}Ga_{0.5}As$ quantum dot laser on silicon," *Electronics letters*, vol. 41, no. 13, pp. 742–744, 2005.

[19] J. Yang, P. Bhattacharya, and Z. Mi, "High-performance in 0.5 ga 0.5 as/gaas quantum-dot lasers on silicon with multiple-layer quantum-dot dislocation filters," *Electron Devices, IEEE Transactions on*, vol. 54, no. 11, pp. 2849–2855, 2007.

[20] T. Wang, H. Liu, A. Lee, F. Pozzi, and A. Seeds, "1.3-μm InAs/GaAs quantum-dot lasers monolithically grown on Si substrates," *Optics Express*, vol. 19, no. 12, pp. 11381–11386, 2011.

[21] A. Lee, Q. Jiang, M. Tang, A. Seeds, and H. Liu, "Continuous-wave InAs/GaAs quantum-dot laser diodes monolithically grown on Si substrate with low threshold current densities," *Optics Express*, vol. 20, no. 20, pp. 22181–22187, 2012.

[22] S. Chen, M. Tang, J. Wu, Q. Jiang, V. Dorogan, M. Benamara, Y. Mazur, G. Salamo, A. Seeds, and H. Liu, "1.3 μm InAs/GaAs quantum-dot laser monolithically grown on Si substrates operating over 100 C," *Electronics Letters*, vol. 50, no. 20, pp. 1467–1468, 2014.

[23] A. Y. Liu, R. W. Herrick, O. Ueda, P. M. Petroff, A. C. Gossard, and J. E. Bowers, "Reliability of inas/gaas quantum dot lasers epitaxially grown on silicon," *IEEE Journal on Selected Topics in Quantum Electronics*, vol. 21, no. 6, 2015.

[24] S. Chen, W. Li, J. Wu, Q. Jiang, M. Tang, S. Shutts, S. N. Elliott, A. Sobiesierski, A. J. Seeds, I. Ross, P. M. Smowton, and H. Liu, "Electrically pumped continuous-wave iii–v quantum dot lasers on silicon," *Nature Photonics*, 2016.

[25] L. A. Coldren, S. W. Corzine, and M. L. Mashanovitch, *Diode lasers and photonic integrated circuits*, vol. 218. John Wiley & Sons, 2012.

[26] H. Kroemer, "Nobel lecture: quasielectric fields and band offsets: teaching electrons new tricks," *Reviews of modern physics*, vol. 73, no. 3, p. 783, 2001.

[27] Y. Arakawa and H. Sakaki, "Multidimensional quantum well laser and temperature dependence of its threshold current," *Applied Physics Letters*, vol. 40, p. 939, 1982.

[28] M. Sugawara and M. Usami, "Quantum dot devices: Handling the heat," *Nature Photonics*, vol. 3, no. 1, pp. 30–31, 2009.

[29] `http://www.innolume.com/index.htm`.

[30] D. Bimberg and U. W. Pohl, "Quantum dots: promises and accomplishments," *Materials Today*, vol. 14, no. 9, pp. 388–397, 2011.

[31] T. Kageyama, K. Nishi, M. Yamaguchi, R. Mochida, Y. Maeda, K. Takemasa, Y. Tanaka, T. Yamamoto, M. Sugawara, and Y. Arakawa, "Extremely high temperature (220 C) continuous-wave operation of 1300-nm-range quantum-dot lasers," in *The European Conference on Lasers and Electro-Optics*, Optical Society of America, 2011.

[32] J. J. Coleman, J. D. Young, and A. Garg, "Semiconductor quantum dot lasers: a tutorial," *Journal of Lightwave Technology*, vol. 29, no. 4, pp. 499–510, 2011.

[33] C. Gilfert, V. Ivanov, N. Oehl, M. Yacob, and J. Reithmaier, "High gain 1.55 μm diode lasers based on inas quantum dot like active regions," *Applied Physics Letters*, vol. 98, no. 20, pp. 201102–201102, 2011.

[34] J. Gérard, O. Cabrol, and B. Sermage, "Inas quantum boxes: Highly efficient radiative traps for light emitting devices on si," *Applied physics letters*, vol. 68, no. 22, pp. 3123–3125, 1996.

[35] A. Y. Liu, S. Srinivasan, J. Norman, A. C. Gossard, and J. E. Bowers, "Quantum dot lasers for silicon photonics [invited]," *Photonics Research*, vol. 3, no. 5, pp. B1–B9, 2015.

[36] H. Liu, T. Wang, Q. Jiang, R. Hogg, F. Tutu, F. Pozzi, and A. Seeds, "Long-wavelength InAs/GaAs quantum-dot laser diode monolithically grown on Ge substrate," *Nature Photonics*, vol. 5, no. 7, pp. 416–419, 2011.

[37] M. Yamaguchi and C. Amano, "Efficiency calculations of thin-film gaas solar cells on si substrates," *Journal of applied physics*, vol. 58, no. 9, pp. 3601–3606, 1985.

[38] S. Hu, S. Corzine, K.-K. Law, D. Young, A. Gossard, L. Coldren, and J. Merz, "Lateral carrier diffusion and surface recombination in ingaas/algaas quantum-well ridge-waveguide lasers," *Journal of applied physics*, vol. 76, no. 8, pp. 4479–4487, 1994.

[39] J. K. Kim, R. L. Naone, and L. A. Coldren, "Lateral carrier confinement in miniature lasers using quantum dots," *IEEE Journal of Selected Topics in Quantum Electronics*, vol. 6, no. 3, pp. 504–510, 2000.

[40] W. W. Chow, A. Y. Liu, A. C. Gossard, and J. E. Bowers, "Extraction of inhomogeneous broadening and nonradiative losses in inas quantum-dot lasers," *Applied Physics Letters*, vol. 107, no. 17, p. 171106, 2015.

[41] S. A. Moore, L. O'Faolain, M. A. Cataluna, M. B. Flynn, M. V. Kotlyar, and T. F. Krauss, "Reduced surface sidewall recombination and diffusion in quantum-dot lasers," *Photonics Technology Letters, IEEE*, vol. 18, no. 17, pp. 1861–1863, 2006.

[42] N. Kumagai, K. Watanabe, M. Ishida, Y. Nakata, N. Hatori, H. Sudo, T. Yamamoto, M. Sugawara, and Y. Arakawa, "Process-free estimation of threshold current density of inas quantum dot laser," *physica status solidi (c)*, vol. 5, no. 9, pp. 2935–2937, 2008.

[43] Y. Li, Y. Xin, H. Su, L. F. Lester, A. L. Gray, S. Luong, K. Sun, Z. Zou, and J. Zilko, "Photoluminescence characterization of quantum dot laser epitaxy," in *Integrated Optoelectronic Devices 2005*, pp. 138–145, International Society for Optics and Photonics, 2005.

[44] K. Eberl, M. Lipinski, Y. Manz, W. Winter, N. Jin-Phillipp, and O. Schmidt, "Self-assembling quantum dots for optoelectronic devices on si and gaas," *Physica E: Low-dimensional Systems and Nanostructures*, vol. 9, no. 1, pp. 164–174, 2001.

[45] P. M. Petroff, "Epitaxial growth and electronic structure of self-assembled quantum dots," in *Single Quantum Dots*, pp. 1–24, Springer, 2003.

[46] A. V. Barve and S. Krishna, "Chapter 3 - quantum dot infrared photodetectors," in *Advances in Infrared Photodetectors* (D. R. R. Sarath D. Gunapala and C. Jagadish, eds.), vol. 84 of *Semiconductors and Semimetals*, pp. 153 – 193, Elsevier, 2011.

[47] K. Radhakrishnan, S. Yoon, R. Gopalakrishnan, and K. Tan, "Indium desorption from strained ingaas/gaas quantum wells grown by molecular beam epitaxy," *Journal of Vacuum Science & Technology A*, vol. 12, no. 4, pp. 1124–1128, 1994.

[48] H. Liu, M. Hopkinson, C. Harrison, M. Steer, R. Frith, I. Sellers, D. Mowbray, and M. Skolnick, "Optimizing the growth of 1.3 μm InAs/InGaAs dots-in-a-well structure," *Journal of applied physics*, vol. 93, no. 5, pp. 2931–2936, 2003.

[49] M. Ohta, T. Kanto, and K. Yamaguchi, "Self-formation of high-density and high-uniformity inas quantum dots on sb/gaas layers by molecular beam epitaxy," *Japanese journal of applied physics*, vol. 45, no. 4S, p. 3427, 2006.

[50] K. J. Vahala, "Quantum box fabrication tolerance and size limits in semiconductors and their effect on optical gain," *IEEE journal of quantum electronics*, vol. 24, no. 3, pp. 523–530, 1988.

[51] A. Hospodková, "Capping of inas/gaas quantum dots for gaas based lasers,"

[52] A. Lenz, H. Eisele, R. Timm, L. Ivanova, H.-Y. Liu, M. Hopkinson, U. Pohl, and M. Dähne, "Structure of inas quantum dots-in-a-well nanostructures," *Physica E: Low-dimensional Systems and Nanostructures*, vol. 40, no. 6, pp. 1988–1990, 2008.

[53] H. Tanoto, S. Yoon, T. Ng, C. Ngo, C. Dohrman, E. Fitzgerald, L. Tan, and C. Tung, "Origin and suppression of v-shaped defects in the capping of self-assembled inas quantum dots on graded si1-xgex/si substrate," *Applied physics letters*, vol. 95, no. 5, p. 2111, 2009.

[54] H. Sasakura, S. Kayamori, S. Adachi, and S. Muto, "Effect of indium-flush method on the control of photoluminescence energy of highly uniform self-assembled InAs quantum dots by slow molecular beam epitaxy growth," *Journal of applied physics*, vol. 102, no. 1, pp. 013515–013515, 2007.

[55] D. Sizov, M. Maksimov, A. Tsatsulnikov, N. Cherkashin, N. Kryzhanovskaya, A. Zhukov, N. Maleev, S. Mikhrin, A. Vasilev, R. Selin, *et al.*, "The influence of heat treatment conditions on the evaporation of defect regions in structures with ingaas quantum dots in the gaas matrix," *Semiconductors*, vol. 36, no. 9, pp. 1020–1026, 2002.

[56] W. W. Chow, A. Y. Liu, A. C. Gossard, J. E. Bowers, and F. Jahnke, "Gain-current relationships in quantum-dot and quantum-well lasers: theory and experiment," in *2015 IEEE Photonics Conference (IPC)*, pp. 569–570, Oct 2015.

[57] D. Lubyshev, J. Fastenau, Y. Wu, W. Liu, M. Bulsara, E. Fitzgerald, and W. Hoke, "Molecular beam epitaxy growth of metamorphic high electron mobility transistors and metamorphic heterojunction bipolar transistors on ge and ge-on-insulator/si substrates," *Journal of Vacuum Science & Technology B*, vol. 26, no. 3, pp. 1115–1119, 2008.

[58] C. Walker, I. Sandall, P. M. Smowton, I. Sellers, D. Mowbray, H. Liu, and M. Hopkinson, "The role of high growth temperature gaas spacer layers in 1.3-μm in (ga) as quantum-dot lasers," *IEEE photonics technology letters*, vol. 17, no. 10, pp. 2011–2013, 2005.

[59] A. Y. Liu, C. Zhang, A. Snyder, D. Lubyshev, J. M. Fastenau, A. W. Liu, A. C. Gossard, and J. E. Bowers, "MBE growth of P-doped 1.3 μm InAs quantum dot lasers on silicon," *Journal of Vacuum Science & Technology B*, vol. 32, no. 2, p. 02C108, 2014.

[60] A. Kosogov, P. Werner, U. Gösele, N. Ledentsov, D. Bimberg, V. Ustinov, A. Y. Egorov, A. Zhukov, P. KopeV, N. Bert, *et al.*, "Structural and optical properties of inas–gaas quantum dots subjected to high temperature annealing," *Applied physics letters*, vol. 69, no. 20, pp. 3072–3074, 1996.

[61] D. Guimard, M. Ishida, D. Bordel, L. Li, M. Nishioka, Y. Tanaka, M. Ekawa, H. Sudo, T. Yamamoto, H. Kondo, *et al.*, "Ground state lasing at 1.30 μm from InAs/GaAs quantum dot lasers grown by metal–organic chemical vapor deposition," *Nanotechnology*, vol. 21, no. 10, p. 105604, 2010.

[62] D. Lacombe, A. Ponchet, J.-M. Gerard, and O. Cabrol, "Structural study of InAs quantum boxes grown by molecular beam epitaxy on a (001) GaAs-on-Si substrate," *Applied physics letters*, vol. 70, no. 18, pp. 2398–2400, 1997.

[63] R. R. Alexander, D. T. Childs, H. Agarwal, K. M. Groom, H.-Y. Liu, M. Hopkinson, R. A. Hogg, M. Ishida, T. Yamamoto, M. Sugawara, Y. Arakawa, T. J. Badcock, R. J. Royce, and D. J. Mowbray, "Systematic study of the effects of modulation p-doping on 1.3-μm quantum-dot lasers," *Quantum Electronics, IEEE Journal of*, vol. 43, no. 12, pp. 1129–1139, 2007.

[64] H.-H. Chang, A. W. Fang, M. N. Sysak, H. Park, R. Jones, O. Cohen, O. Raday, M. J. Paniccia, and J. E. Bowers, "1310nm silicon evanescent laser," *Opt. Express*, vol. 15, pp. 11466–11471, Sep 2007.

[65] K. Tanabe, T. Rae, K. Watanabe, and Y. Arakawa, "High-temperature 1.3 μm inas/gaas quantum dot lasers on si substrates fabricated by wafer bonding," *Applied Physics Express*, vol. 6, no. 8, p. 082703, 2013.

[66] I. P. Marko, A. R. Adams, N. F. Massé, and S. J. Sweeney, "Effect of non-pinned carrier density above threshold in inas quantum dot and quantum dash lasers," *IET Optoelectronics*, vol. 8, no. 2, pp. 88–93, 2014.

[67] L. Kimerling, "Recombination enhanced defect reactions," *Solid-State Electronics*, vol. 21, no. 11, pp. 1391–1401, 1978.

[68] P. Petroff and R. Hartman, "Rapid degradation phenomenon in heterojunction gaalas–gaas lasers," *Journal of Applied Physics*, vol. 45, no. 9, pp. 3899–3903, 1974.

[69] J. Van der Ziel, R. Dupuis, R. Logan, and C. Pinzone, "Degradation of gaas lasers grown by metalorganic chemical vapor deposition on si substrates," *Applied physics letters*, vol. 51, no. 2, pp. 89–91, 1987.

[70] Z. I. Kazi, P. Thilakan, T. Egawa, M. Umeno, and T. Jimbo, "Realization of gaas/algaas lasers on si substrates using epitaxial lateral overgrowth by metalorganic chemical vapor deposition," *Japanese Journal of Applied Physics*, vol. 40, no. 8R, p. 4903, 2001.

[71] H.-Y. Liu, B. Xu, Y.-Q. Wei, D. Ding, J.-J. Qian, Q. Han, J.-B. Liang, and Z.-G. Wang, "High-power and long-lifetime inas/gaas quantum-dot laser at 1080 nm," *Applied Physics Letters*, vol. 79, no. 18, pp. 2868–2870, 2001.

[72] R. Beanland, A. Sanchez, D. Childs, K. Groom, H. Liu, D. Mowbray, and M. Hopkinson, "Structural analysis of life tested 1.3 μm quantum dot lasers," *Journal of Applied Physics*, vol. 103, no. 1, p. 014913, 2008.

[73] J.-S. Huang, "Temperature and current dependences of reliability degradation of buried heterostructure semiconductor lasers," *IEEE Transactions on Device and Materials Reliability*, vol. 5, no. 1, pp. 150–154, 2005.

[74] S. Srinivasan, N. Julian, J. Peters, D. Liang, and J. E. Bowers, "Reliability of hybrid silicon distributed feedback lasers," *IEEE Journal of Selected Topics in Quantum Electronics*, vol. 19, no. 4, pp. 1501305–1501305, 2013.

[75] P. Kightley, P. Goodhew, R. Bradley, and P. Augustus, "A mechanism of misfit dislocation reaction for gainas strained layers grown onto off-axis gaas substrates," *Journal of crystal growth*, vol. 112, no. 2-3, pp. 359–367, 1991.

[76] P. Petroff and R. Hartman, "Defect structure introduced during operation of heterojunction gaas lasers," *Applied Physics Letters*, vol. 23, no. 8, pp. 469–471, 1973.

[77] A. Sanchez, R. Beanland, N. F. Hasbullah, M. Hopkinson, and J. David, "Correlation between defect density and current leakage in inas/ gaas quantum dot-in-well structures," *Journal of Applied Physics*, vol. 106, no. 2, p. 024502, 2009.

[78] N. F. Hasbullah, J. David, and D. Mowbray, "Dark current mechanisms in quantum dot laser structures," *Journal of Applied Physics*, vol. 109, no. 11, p. 113111, 2011.

[79] H. Choi, C. Wang, and N. Karam, "Gaas-based diode lasers on si with increased lifetime obtained by using strained ingaas active layer," *Applied physics letters*, vol. 59, no. 21, pp. 2634–2635, 1991.

[80] M. E. Groenert, A. J. Pitera, R. J. Ram, and E. A. Fitzgerald, "Improved room-temperature continuous wave gaas/algaas and ingaas/gaas/algaas lasers fabricated on si substrates via relaxed graded gexsi1- x buffer layers," *Journal of Vacuum Science & Technology B*, vol. 21, no. 3, pp. 1064–1069, 2003.

[81] X. Huang, Y. Song, T. Masuda, D. Jung, and M. Lee, "Ingaas/gaas quantum well lasers grown on exact gap/si (001)," *Electronics Letters*, vol. 50, no. 17, pp. 1226–1227, 2014.

[82] K. Beernink, P. K. York, J. Coleman, R. Waters, J. Kim, and C. Wayman, "Characterization of ingaas-gaas strained-layer lasers with quantum wells near the critical thickness," *Applied physics letters*, vol. 55, no. 21, pp. 2167–2169, 1989.

[83] L. Sugiura, "Comparison of degradation caused by dislocation motion in compound semiconductor light-emitting devices," *Applied physics letters*, vol. 70, no. 10, pp. 1317–1319, 1997.

[84] U. Mishra and J. Singh, *Semiconductor device physics and design*. Springer Science & Business Media, 2007.

[85] Y. Hasegawa, T. Egawa, T. Jimbo, and M. Umeno, "Influences of dark line defects on characteristics of algaas/gaas quantum well lasers grown on si substrates," *Japanese journal of applied physics*, vol. 34, no. 6R, p. 2994, 1995.

[86] D. Lang, "Recombination-enhanced reactions in semiconductors," *Annual review of materials science*, vol. 12, no. 1, pp. 377–398, 1982.

[87] P. M. Petroff, "Physics and materials issues behind the lifetime problem in semiconductor lasers and light-emitting diodes," in *Photonics West'96*, pp. 52–58, International Society for Optics and Photonics, 1996.

[88] S. Tomiya, T. Hino, S. Goto, M. Takeya, and M. Ikeda, "Dislocation related issues in the degradation of gan-based laser diodes," *Selected Topics in Quantum Electronics, IEEE Journal of*, vol. 10, no. 6, pp. 1277–1286, 2004.

[89] J. D. Dow and R. E. Allen, "Role of dangling bonds and antisite defects in rapid and gradual iii-v laser degradation," *Applied Physics Letters*, vol. 41, no. 7, pp. 672–674, 1982.

[90] S. Sakai and N. Wada, "Monolithic iii-v light-emitting devices on si substrates," *Fiber & Integrated Optics*, vol. 13, no. 1, pp. 31–44, 1994.

[91] M. Ettenberg and C. Nuese, "Reduced degradation in inxga1- xas electroluminescent diodes," *Journal of Applied Physics*, vol. 46, no. 5, pp. 2137–2142, 1975.

[92] T. Kajimura, "Degradation mechanisms of ga1- xalxas visible diode lasers," *Journal of Applied Physics*, vol. 51, no. 2, pp. 908–913, 1980.

[93] K. Gündoğdu, K. Hall, T. F. Boggess, D. Deppe, and O. Shchekin, "Ultrafast electron capture into p-modulation-doped quantum dots," *Applied physics letters*, vol. 85, no. 20, pp. 4570–4572, 2004.

[94] S. Y. Karpov and Y. N. Makarov, "Dislocation effect on light emission efficiency in gallium nitride," *Applied physics letters*, vol. 81, no. 25, pp. 4721–4723, 2002.

[95] E. C. Madhava-Menon, P. Petroff, and R. Waters, "Degradation kinetics of gaas quantum well lasers," *Applied Physics Letters*, vol. 54, no. 26, pp. 2683–2685, 1989.

[96] A. Goodwin, P. Kirkby, I. Davies, and R. Baulcomb, "The effects of processing stresses on residual degradation in long-lived ga1- xalxas lasers," *Applied Physics Letters*, vol. 34, no. 10, pp. 647–649, 1979.

[97] R. Hartman and A. Hartman, "Strain-induced degradation of gaas injection lasers," *Applied Physics Letters*, vol. 23, no. 3, pp. 147–149, 1973.

[98] P. W. Epperlein, *Semiconductor Laser Engineering, Reliability and Diagnostics: A Practical Approach to High Power and Single Mode Devices*. John Wiley & Sons, 2013.

[99] T. Yamada, M. Tachikawa, T. Sasaki, H. Mori, and Y. Kadota, "7000 h continuous wave operation of multiple quantum well laser on si at 50 c," *Applied physics letters*, vol. 70, no. 12, pp. 1614–1615, 1997.

[100] T. Sasaki, H. Mori, M. Tachikawa, and T. Yamada, "Aging tests of inp-based laser diodes heteroepitaxially grown on si substrates," *Journal of applied physics*, vol. 84, no. 12, pp. 6725–6728, 1998.

[101] Z. I. Kazi, T. Egawa, T. Jimbo, and M. Umeno, "First room-temperature continuous-wave operation of self-formed ingaas quantum dot-like laser on si substrate grown by metalorganic chemical vapor deposition," *Japanese Journal of Applied Physics*, vol. 39, no. 7R, p. 3860, 2000.

[102] Y. Wan, Q. Li, A. Y. Liu, A. C. Gossard, J. E. Bowers, E. L. Hu, and K. M. Lau, "Optically pumped 1.3 μm room-temperature inas quantum-dot micro-disk lasers directly grown on (001) silicon," *Optics letters*, vol. 41, no. 7, pp. 1664–1667, 2016.

[103] Z. Wang, B. Tian, M. Pantouvaki, J. V. Campenhout, C. Merckling, and D. V. Thourhout, "Room temperature ingaas/inp distributed feedback laser directly grown on silicon," in *Conference on Lasers and Electro-Optics*, p. SW4M.3, Optical Society of America, 2016.

[104] R. Tkach and A. Chraplyvy, "Regimes of feedback effects in 1.5-μm distributed feedback lasers," *Journal of Lightwave technology*, vol. 4, no. 11, pp. 1655–1661, 1986.

[105] T. Komljenovic, S. Srinivasan, E. Norberg, M. Davenport, G. Fish, and J. E. Bowers, "Widely tunable narrow-linewidth monolithically integrated external-cavity semiconductor lasers," *IEEE Journal of Selected Topics in Quantum Electronics*, vol. 21, no. 6, pp. 214–222, 2015.

[106] D. Huang, P. Pintus, C. Zhang, Y. Shoji, T. Mizumoto, and J. E. Bowers, "Electrically driven and thermally tunable integrated optical isolators for silicon photonics," *IEEE Journal of Selected Topics in Quantum Electronics*, vol. 22, pp. 1–8, Nov 2016.

[107] J. Helms and K. Petermann, "A simple analytic expression for the stable operation range of laser diodes with optical feedback," *IEEE Journal of Quantum Electronics*, vol. 26, no. 5, pp. 833–836, 1990.

[108] A. Zhukov, M. Maksimov, and A. Kovsh, "Device characteristics of long-wavelength lasers based on self-organized quantum dots," *Semiconductors*, vol. 46, no. 10, pp. 1225–1250, 2012.

[109] K. Lüdge, E. Schöll, E. Viktorov, and T. Erneux, "Analytical approach to modulation properties of quantum dot lasers," *Journal of applied physics*, vol. 109, no. 10, p. 103112, 2011.

[110] S. Melnik, G. Huyet, and A. V. Uskov, "The linewidth enhancement factor α of quantum dot semiconductor lasers," *Optics Express*, vol. 14, no. 7, pp. 2950–2955, 2006.

[111] D. O'Brien, S. P. Hegarty, G. Huyet, J. G. McInerney, T. Kettler, M. Laemmlin, D. Bimberg, V. M. Ustinov, A. E. Zhukov, S. S. Mikhrin, and A. R. Kovsh, "Feedback sensitivity of 1.3 μm InAs/GaAs quantum dot lasers," *Electronics Letters*, vol. 39, pp. 1819–1820, Dec 2003.

[112] C. Otto, *Dynamics of Quantum Dot Lasers: Effects of Optical Feedback and External Optical Injection*. Springer Science & Business Media, 2014.

[113] B. Lingnau, K. Lüdge, W. W. Chow, and E. Schöll, "Failure of the α factor in describing dynamical instabilities and chaos in quantum-dot lasers," *Phys. Rev. E*, vol. 86, p. 065201, Dec 2012.

[114] J. Wang and K. Petermann, "Noise analysis of semiconductor lasers within the coherence collapse regime," *IEEE Journal of Quantum Electronics*, vol. 27, no. 1, pp. 3–9, 1991.

[115] M. L. Davenport, S. Skendzic, N. Volet, J. C. Hulme, M. J. Heck, and J. E. Bowers, "Heterogeneous Silicon/III-V Semiconductor Optical Amplifiers," *IEEE Journal of Selected Topics in Quantum Electronics*, 2016.

[116] D. Y. Cong, A. Martinez, K. Merghem, G. Moreau, A. Lemaitre, J. G. Provost, O. L. Gouezigou, M. Fischer, I. Krestnikov, A. R. Kovsh, and A. Ramdane, "Optimisation of α-factor for quantum dot inas/gaas fabry-perot lasers emitting at 1.3 μm," *Electronics Letters*, vol. 43, pp. 222–224, February 2007.

[117] T. Komljenovic and J. E. Bowers, "High temperature stability, low coherence and low relative intensity noise semiconductor sources for interferometric sensors," *Optics Express*, vol. 24, no. 20, pp. 22777–22787, 2016.

[118] M. Ishida, K. Watanabe, N. Kumagai, Y. Nakata, N. Hatori, H. Sudo, T. Yamamoto, M. Sugawara, and Y. Arakawa, "Enhanced maximum modal gain of 1.3-μm antimony mediated InAs self-assembled quantum-dot lasers," in *Indium Phosphide & Related Materials, 2007.*, pp. 555–558, IEEE, 2007.

[119] F. Tutu, J. Wu, P. Lam, M. Tang, N. Miyashita, Y. Okada, J. Wilson, R. Allison, and H. Liu, "Antimony mediated growth of high-density InAs quantum dots for photovoltaic cells," *Applied Physics Letters*, vol. 103, no. 4, pp. 043901–043901, 2013.

[120] T. A. Truong, *Terahertz Absorption in InGaAs quantum posts and exciton tuning in InAs/GaAs quantum dots by electromagnetic fields*. PhD thesis, UCSB, 2012.

[121] K. Nishi, T. Kageyama, M. Yamaguchi, Y. Maeda, K. Takemasa, T. Yamamoto, M. Sugawara, and Y. Arakawa, "Molecular beam epitaxial growths of high-optical-gain inas quantum dots on gaas for long-wavelength emission," *Journal of Crystal Growth*, vol. 378, pp. 459–462, 2013.

[122] M. Tang, S. Chen, J. Wu, Q. Jiang, V. G. Dorogan, M. Benamara, Y. I. Mazur, G. J. Salamo, A. Seeds, and H. Liu, "1.3-μm inas/gaas quantum-dot lasers monolithically grown on si substrates using inalas/gaas dislocation filter layers," *Optics express*, vol. 22, no. 10, pp. 11528–11535, 2014.

[123] S. Nakamura, "The roles of structural imperfections in ingan-based blue light-emitting diodes and laser diodes," *Science*, vol. 281, no. 5379, pp. 956–961, 1998.

[124] D. A. Miller, "Device requirements for optical interconnects to silicon chips," *Proceedings of the IEEE*, vol. 97, no. 7, pp. 1166–1185, 2009.

[125] E. Fitzgerald and N. Chand, "Epitaxial necking in gaas grown on pre-pattemed si substrates," *Journal of electronic materials*, vol. 20, no. 7, pp. 839–853, 1991.

[126] X. Zhang, P. Li, G. Zhao, D. W. Parent, F. Jain, and J. Ayers, "Removal of threading dislocations from patterned heteroepitaxial semiconductors by glide to sidewalls," *Journal of electronic materials*, vol. 27, no. 11, pp. 1248–1253, 1998.

[127] M. J. Heck and J. E. Bowers, "Energy efficient and energy proportional optical interconnects for multi-core processors: Driving the need for on-chip sources," *IEEE Journal of Selected Topics in Quantum Electronics*, vol. 20, no. 4, pp. 332–343, 2014.

[128] A. Able, W. Wegscheider, K. Engl, and J. Zweck, "Growth of crack-free gan on si (111) with graded algan buffer layers," *Journal of crystal growth*, vol. 276, no. 3, pp. 415–418, 2005.

[129] S. Zamek, L. Feng, M. Khajavikhan, D. T. Tan, M. Ayache, and Y. Fainman, "Micro-resonator with metallic mirrors coupled to a bus waveguide," *Optics express*, vol. 19, no. 3, pp. 2417–2425, 2011.

[130] D. Liang, S. Srinivasan, D. Fattal, M. Fiorentino, Z. Huang, D. Spencer, J. Bowers, and R. Beausoleil, "Teardrop reflector-assisted unidirectional hybrid silicon microring lasers," *Photonics Technology Letters, IEEE*, vol. 24, no. 22, pp. 1988–1990, 2012.

[131] E. Yablonovitch, C. Sandroff, R. Bhat, and T. Gmitter, "Nearly ideal electronic properties of sulfide coated gaas surfaces," *Applied physics letters*, vol. 51, no. 6, pp. 439–441, 1987.

[132] M. Boroditsky, I. Gontijo, M. Jackson, R. Vrijen, E. Yablonovitch, T. Krauss, C.-C. Cheng, A. Scherer, R. Bhat, and M. Krames, "Surface recombination measurements on iii–v candidate materials for nanostructure light-emitting diodes," *Journal of Applied Physics*, vol. 87, no. 7, pp. 3497–3504, 2000.

[133] V. Chobpattana, E. Mikheev, J. Y. Zhang, T. E. Mates, and S. Stemmer, "Extremely scaled high-k/in0. 53ga0. 47as gate stacks with low leakage and low interface trap densities," *Journal of Applied Physics*, vol. 116, no. 12, p. 124104, 2014.